FUNDAMENTALS THAT UNDERPIN NATIVE MASS SPECTROMETRY: A STUDY OF THERMODYNAMICS, OSMOLYTES, AND ELECTROSPRAY IONIZATION

A Dissertation

by

THOMAS E. WALKER III

Submitted to the Graduate and Professional School of
Texas A&M University
in partial fulfillment of the requirements for the degree of

DOCTOR OF PHILOSOPHY

Chair of Committee,	David H Russell
Committee Members,	Arthur D Laganowsky
	Xin Yan
	Paul D Straight
Head of Department,	Simon W North

December 2022

Major Subject: Chemistry

ABSTRACT

In recent years, native mass spectrometry (nMS) has continued to grow in popularity and recognition as an excellent structural biology tool. The implementation of orthogonal methods to nMS, such as liquid chromatography (LC) and ion mobility spectrometry (IMS), has greatly increased the reach that MS possesses for elucidating structures of biological molecules. However, many aspects that are of vital to understanding solution-phase measurements often go overlooked when conducting nMS experiments, such as solution temperature and thermodynamic trends. Even the mechanisms of electrospray ionization (ESI) are not completely understood in respect to co-solutes and osmolytes.

Herein, a newly designed, variable temperature-ESI (vT-ESI) device for modulating the solution temperature in nMS experiments is used to elucidate thermodynamic quantities for temperature-dependent protein/protein and protein/ligand interactions. The importance of osmolyte contributions toward stability of biomolecules is also underscored as these small molecules perform vitally necessary roles within the complex, dynamic cellular environment. Lastly, the mechanism of the charging of protein ions via ESI is examined in respect to how solution conditions and concentrations of analytes modulate charged ion populations.

In this dissertation, methods for the examination of thermodynamic mechanisms of proteins and protein complexes will be proposed. An explanation of observed thermodynamic trends for ligand-binding proteins systems will examined in respect to

various complimentary methods. Thermodynamic explanation for the interaction mechanism(s) of osmolytes will be given which confirms aspects of osmolyte-water network interactions. Finally, evidence for a dual mechanism of ESI for charge reduction reactions will be examined in an attempt to explain how the solution environment in a charged droplet leads to drastically different charge states for protein ions.

DEDICATION

For my parents for their unconditional love and support

For my wife Emily and her encouraging me to be the best version of myself

For my son who will be joining us soon.

ACKNOWLEDGEMENTS

I would like to thank my committee chair, Professor David H. Russell, for his guidance through my graduate career. I would also like to thank him for allowing me to have the freedom to pursue interesting projects.

I would also like to thank my committee members, Dr. Laganowsky, Dr. Yan, and Dr. Straight for their guidance and support.

I would like to thank former and current RRG students and postdocs for their support during my time at Texas A&M. Dr. Jacob McCabe for motivating me to start new projects, Dr. Chris Mallis for excellent critical feedback on presentations and papers, Dr. Michael Herbert for his guidance on the Cryo, Dr. Michael Poltash for helping me assemble my first ToF-MS, and Dr. Robert Schrader for helping fill gaps in my instrumentational knowledge.

I would also like to thank collaborators from other departments and universities for their help during my graduate career. Dr. Clowers from Washington State University, Dr. Wysocki from the Ohio State University, Gordon Anderson founder of Gordan A. Anderson Custom Electronics, and Dr. Rye from the Department of Biophysics and Biochemistry at Texas A&M; the GroEL studies would not have been possible without excellent GroEL expression and purification provided by his laboratory.

I would like to thank William Seward and Karl Yeager from the Chemistry Machine Shop for their expertise in turning my terrible CAD drawings into precision parts for MS instrumentation and for Will again teaching me how to weld.

Lastly, I would like to thank my past instructors. Dr. Allen, Dr. Davy, Dr. Raner, Dr. Brynteson, and Lauren Brynteson (Hopper) from Liberty University Department of Chemistry and Biology for encouraging me to pursue a graduate degree in chemistry. Mr. Tierney, Mrs. Walker, Mrs. Combs, Mr. Doan, Mrs. Laird, Mr. Burbach, and Mr. Matthews from South Merrimack Christian Academy for the sacrifices they made to provide a better education for many generations of students.

CONTRIBUTORS AND FUNDING SOURCES

Contributors

This work was supervised by a dissertation committee consisting of Professor David H Russell [advisor], Dr. Arthur D Laganowsky, and Dr. Xin Yan of the Department of Chemistry and Dr. Paul D Straight of the Department of Biochemistry and Biophysics.

Funding Sources

Graduate study was partially supported by a fellowship from Texas A&M University from the Hagler Institute for Advanced Study.

This work was also made possible in part by the National Institute of Health (NIH) under Grant Numbers P41GM128577 and R01GM138863. Its contents are solely the responsibility of the authors and do not necessarily represent the official views of the NIH.

NOMENCLATURE

ADP	adenosine diphosphate
AmAc	ammonium acetate
ATD	arrival time distribution
ATP	adenosine triphosphate
CCS	collision cross section
CD-MS	charge detection mass spectrometry
CEM	chain ejection model
CID	collision induced dissociation
CRM	charge residue model
Cryo-EM	cryogenic electron microscopy
Cryo-IM-MS	cryogenic ion mobility-mass spectrometry
DC	direct current
DSC	differential scanning calorimetry
e	elementary charge (1.602×10^{-19} Coulombs)
ESI	electrospray ionization
ECD	electron capture dissociation
EDDA	ethylenediamine diacetate
FAIMS	field-asymmetric ion mobility spectrometry
FT	Fourier transform
FT-ICR	Fourier transform-ion cyclotron resonance

H-bond	hydrogen bond
HT	Hadamard transform
IEM	ion evaporation model
IM	ion mobility
IMS	ion mobility spectrometry
IM-MS	ion mobility-mass spectrometry
IRMPD	infrared multiple photon dissociation
ITC	isothermal titration calorimetry
K	ion mobility parameter
K_0	reduced mobility coefficient
k_B	Maxwell-Boltzmann constant
L	drift tube length
LC	liquid chromatography
MALDI	matrix-assisted laser desorption ionization
MCP	microchannel plate
MDS	molecular dynamics simulations
MS	mass spectrometry
m/z	mass-to-charge ratio
nMS	native mass spectrometry
N	buffer gas number density
NMR	nuclear magnetic resonance
P	buffer gas pressure

PF IF	periodic focusing ion funnel
RF	radio frequency (voltage)
SEC	size exclusion chromatography
SP	substance P
T	buffer gas temperature
TEAA	triethylamine acetate
TEM	transmission electron microscopy
TMAO	trimethylamine *N*-oxide
TOF	time-of-flight (mass spectrometer)
TWIMS	traveling wave ion mobility spectrometry
UVPD	ultraviolet photodissociation
V	voltage
XRD	X-ray diffraction
z	ion charge state
ΔG	change in Gibbs' free energy
ΔH	change in enthalpy
ΔS	change in entropy
μ	reduced mass of ion-neutral pair
v_d	average drift velocity
vT	variable temperature
Ω	momentum transfer integral (collisional-cross section)

TABLE OF CONTENTS

Page

LIST OF FIGURES

Page

LIST OF TABLES

Page

1. INTRODUCTION

1.1. Overview of Native Mass Spectrometry

Structural mass spectrometry (MS) has evolved from the early artforms of interpreting bonding configurations of atoms/functional groups of small molecules ionized by electron impact ionization[1] to the method of choice for determining the amino acid sequences of proteins to studies of higher-order protein structure (2^o, 3^o, and 4^o). These evolutionary developments have expanded the experimental versatility, mass range and resolution of MS instruments, thereby opening new vistas for studies of large biomolecules,[2] membrane protein complexes[3] and even viruses.[4] Native mass spectrometry is an approach used to study biochemical structure and function of proteins and enzymes that relies on a mass analyzer to act as a detector and measure the mass-to-charge ratio (*m/z*) of gas-phase ions.[5] NMS is employed by many researchers as a compliment to more traditional structural characterization methods such as X-ray diffraction (XRD), nuclear magnetic resonance (NMR), electron microscopy (TEM and Cryo-EM).[6] NMS also offers investigators the opportunity to use mass spectrometry to monitor solution phase reactions.[7-15] **Figure 1.1** demonstrates the relation of nMS to other structural biology techniques.

From the advent of mass spectrometry by JJ Thompson in 1912 to the introduction of matrix-assisted laser desorption (MALDI) in 1985[16] mass spectrometry was largely

*Reprinted with permission from Walker, T. E.; Laganowsky, A.; Russell, D. H. Surface Activity of Amines Provides Evidence for the Combined ESI Mechanism of Charge Reduction for Protein Complexes. Anal Chem 2022. DOI: 10.1021/acs.analchem.2c01814.

employed to study atomic and polyatomic ions or to elucidate structure of organic compounds and small peptides. It was not until the discovery of electrospray ionization by Fenn in 1991 that the analysis of intact, solution-phase (native) biomolecules could be ionized reliably.[17] The incorporation of ESI enabled solution-phase structure and interaction to be gently transitioned into the gas phase meaning that solution-phase reactions could now be interrogated with the specificity and sensitivity afforded by MS. The use of ESI is thought to have a freeze-drying effect, that as solvent is removed conformations of biomolecules become kinetically trapped.[18, 19]

Many different methods for structural and functional analysis have been added to the "tool-kit" of nMS. The advent of new mass analyzer technology such as the orbitrap and the improvement of more conventional mass analyzers like ToF and quadrupoles[20,

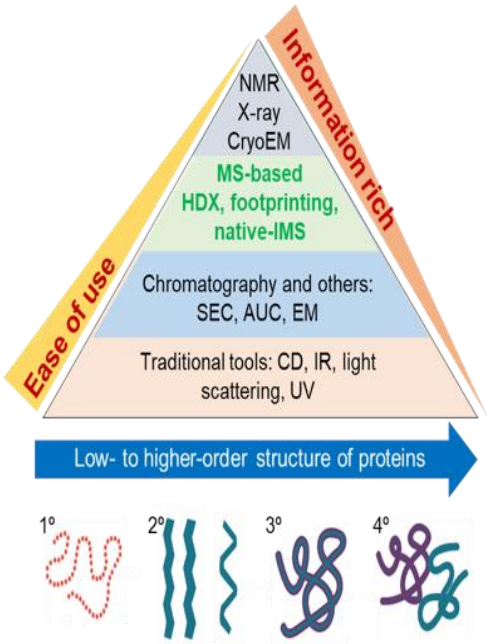

Figure 1.1 Comparison of native IM-MS to other the more conventional structural biology techniques used for protein structure studies. First presented by M. L. Gross as part of 2018 Symposium to honor his ACS Award in Analytical Chemistry.

21] have moved the frontiers of MS by increasing sensitivity, resolving power, and *m/z* range. Ion mobility spectrometry (IMS) is a popular technique to look at overall structural characteristics and monitor conformational changes by separating ions by their size and charge that has also received some technological upgrades.[22] Dissociation techniques such as SID, ECD, UVPD, CID, and IRMPD are routinely used to study primary, secondary, tertiary, and quaternary structure of proteins and protein complexes.[23-28]

1.1.1. Electrospray Ionization

ESI is a "soft" ionization method that quickly rose to prominence in the 1990's an excellent method for generating multiply charged gas-phase ions directly from a solution while limiting fragmentation.[29] The earliest ESI experiments demonstrated the ability to ionize peptides, but today ESI is nearly ubiquitous in the MS community and is used consistently to ionize intact protein complexes and even virus capsids approaching the 150 MDa range.[30] The adoption of ESI has radically transformed MS and has allowed for the coupling of orthogonal methods like capillary electrophoresis (CE) and liquid chromatography (LC).

ESI operates by imparting a voltage upon a solution in a small capillary with a tapered end (~100 μm). The voltage applied to solution (typically positive) causes positive charge to build in the solution toward the end of the emitter. This buildup of excess charge will cause the formation of a Taylor cone, which will sputter charged droplets in an effort to expel excess charges toward the receiving electrode (typically the entrance to a mass spectrometer). During the transit of these charged droplets from the emitter to the entrance

of the mass spectrometer, evaporation of the solvent will increase the relative coulombic forces felt by the droplet as the charges become more closely packed together.[17, 31, 32] When these coulombic repulsive forces become greater than the that of the surface tension of the droplet a fissioning event known as a "Rayleigh explosion" occurs which spawns many smaller highly charged droplets.[33] It is from these droplets that gas phase ions emanate and are detected in the mass spectrometer.

One problematic consequence of using ESI for generating ions from traditional solutions and buffers is the presence of residual salts and solvent molecules that greatly reduce resolving power and resolution in the mass spectrometer. Traditional buffers often have mM concentrations of Na^+, K^+, Cl^-, Tris, HEPES, or many other metal and organic ions and compounds that often adduct to biomolecular ions during the ESI process. This makes the removal of these nonspecific adducts a priority for nMS techniques.[34, 35]

Ammonium acetate (AmAc) is easily the most ubiquitous nMS solution used to analyze biomolecules because the ammonium ions are highly volatile, making ammonia an excellent leaving group; this evaporative process leaves behind protons which give the biomolecular ions their charge.[36, 37] It is common practice in nMS to "buffer exchange" samples via size exclusion chromatography (SEC) into an AmAc solution prior to MS analysis. Other buffer systems offer the ability to increase or decrease the average charge state of ions, often referred to as super-charging or charge reduction reagents. Ethylenediamine diacetate (EDDA) and triethylamine acetate (TEAA) are common charge reducing reagents and sulfolanes are typically used to induce super charging.[18,

32, 38-41] Aspects of these respective charging reactions are expounded upon in **Chapter 3**.

Other methods employed to reduce the prevalence of nonspecific adducts and residual solvent are nano (n)ESI and gas-phase declustering. NESI was coined by Wilm and Mann in 1996 when they demonstrated the ability to use ESI at low flow rates (<100 nL/min).[42-44] NESI is thought to reduce unwanted salt adductions by generating smaller initial droplets, which, as a result, contain smaller populations of aqueous salt ions. Williams et al. demonstrated that the use of very small (~100 nm i.d.) nESI emitters produced relatively "clean" ions without needing to exchange buffers to AmAc.[45] Gas-phase declustering is a general term that describes the use of gas phase collisions with background gas to remove endogenous adducts. Most methods of declustering rely on the acceleration of ions into regions of relatively higher pressure (10^{-2} to 10^{-3} torr) or trapping of ions in these pressure regions.[46] The former uses a few high energy collisions to remove adducts, whereas the latter uses many low energy collisions to accomplish the stripping of solvents and salts.

Several ionization mechanisms have been argued for and against in an attempt to elucidate correct mechanisms of gas-phase generation of ions from ESI. The main three ionization mechanisms are: the charge residue model (CRM),[37, 47] ion evaporation model (IEM),[48-52] and the chain ejection model (CEM).[53-55] The CRM posits that once nanodroplets have been expelled from the parent droplet that solvent evaporation will lead to the deposition of the residual charge that is present in the nanodroplet onto the molecule. The CRM is often cited as the accepted mechanism for the formation of larger

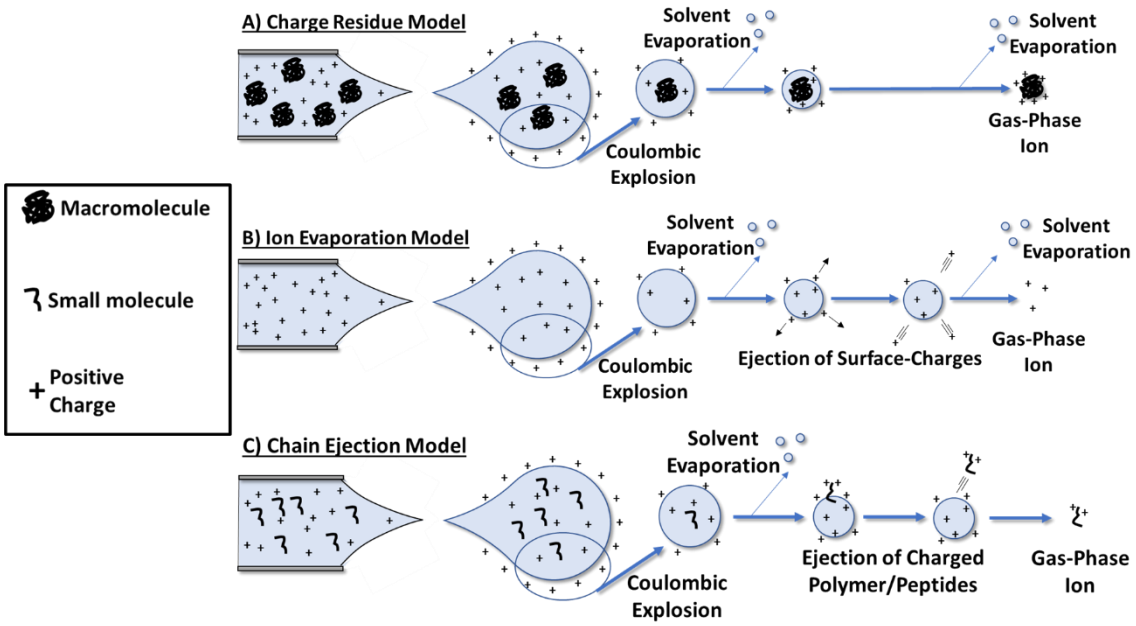

Figure 1.2 A) A depiction of the CRM where ions become charged due to the deposition of charges onto the ion as the solvent evaporates. B) IEM showing the ejection of charged ions from the droplet. C) CEM is thought to explain the charging of chain like polymers and peptides.

biomolecular ions (>2000 Da). The IEM relies on the understanding of charges on the surface of a sphere from Gauss' law. The charges arranged on the surface of sphere and as solvent evaporation occurs this will induce higher coulombic repulsive force. To relieve this stress, according to the IEM, charged species will evaporate from the surface and become gas-phase ions prior to the droplet reaching the Rayleigh instability limit. The IEM is primarily accepted as the ionization mechanism for atomic, small poly atomic, and organic ions. The CEM theorizes that charged molecular chains (such as polymers or peptide chains) may migrate to the surface of the droplet and then become expelled from the droplet should the charge repulsion be great enough to overcome the solvation forces.

The CEM is thought to apply to primarily to small peptides and charged polymers. Schematics of these mechanism are presented in **Figure 1.2**.

1.1.2. Ion Mobility Spectrometry

Ion mobility spectrometry (IMS) is a method commonly employed in nMS to elucidate overall structure or monitor conformational drifts in protein structure by separating gas-phase ions based on size and charge.[56-58] The operating principle is similar to that used in other separations techniques such as chromatography. Gas-phase ions are accelerated by an electric field in a low-pressure region (~1 torr) of an inert gas. Larger ions undergo more collisions resulting in a slower transit across the drift length

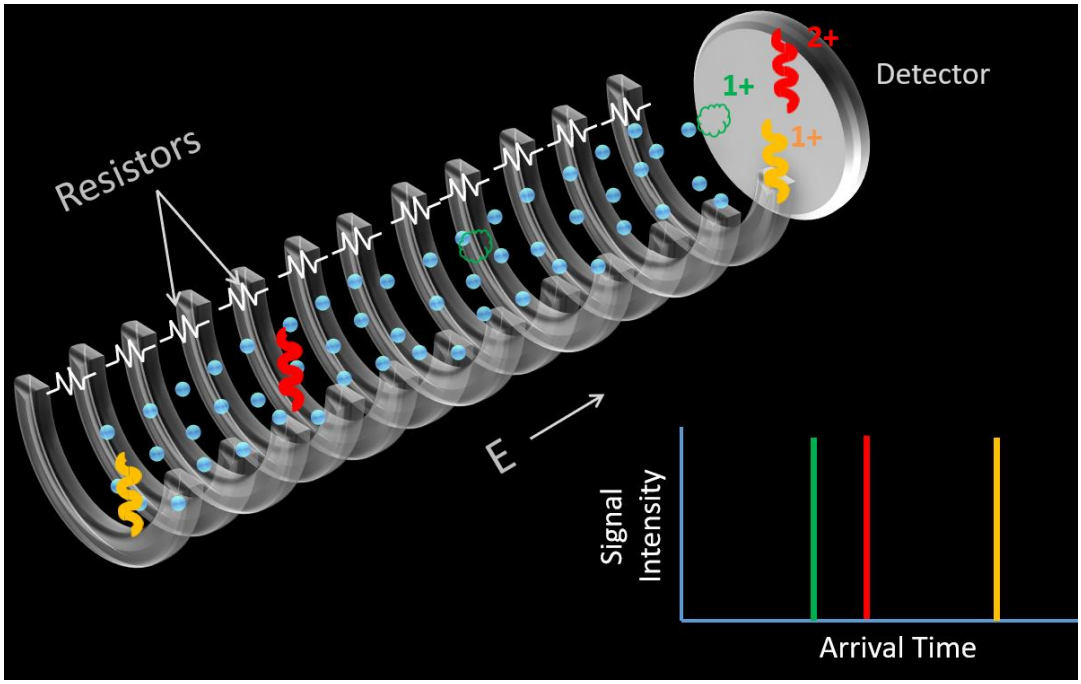

Figure 1.3 A model of a DTIMS experiment, showing separation based on molecule size (green/orange) and charge (red/orange). The green ion has the highest mobility, K, and the fastest arrival time.

(**Figure 1.3**). Charge is also important as it will define how much force is imparted by the electric field used to accelerate the ions; ions of the same shape and size but with different charges will have different mobilities. It is the two main variables of size and charge which enables measurement of an ion's ion-neutral collision-cross section (CCS).

The mobility of an ion is defined by the velocity that ion traverses the drift region and the electric field strength applied to the ion. **Equation 1-1** defines the mobility of ions where K is ion mobility, v_d is drift velocity, and E is electric field strength.

Equation 1-1

$$K = \frac{v_d}{E}$$

However, there are other important variables that must be taken into account when considering ion mobility as a measurement of ion size. Gas composition, pressure, and temperature of the drift gas greatly influence the drift time (t_d) of ions. To account for these variables, ion mobility is commonly reported as "reduced mobility" (K_0) which is defined by **Equation 1-2** where p is the pressure of the drift gas, T is the temperature of the drift gas, and p_0 and T_0 are the standard pressure and temperature (760 torr and 273 K).

Equation 1-2

$$K_0 = K\frac{p}{p_0}\frac{T_0}{T}$$

Using K_0 allows for direct comparison of results between laboratories as long as the same drift gas composition is used.

CCS is common metric used to gauge the relative size of ions. While the quantity is better defined as a momentum transfer integral, CCS has become an important tool for

nMS studies of structural biology. The Mason-Schamp equation is used to calculate the CCS for a given ion under well-defined conditions; the expanded form which uses the reduced ion mobility is given in **Equation 1-3**.

Equation 1-3

$$\Omega = \frac{\sqrt{18\pi}}{16}\frac{ze}{\sqrt{\mu k_b T}}\frac{t_d E}{L}\frac{760}{p}\frac{T}{273}\frac{1}{N_0}$$

Where Ω is the CCS, z is number of charges, e is the elementary charge, μ is the reduced mass of the ion-neutral pair, k_b is the Maxwell-Boltzmann constant, T is an approximation that only accounts for the drift gas temperature, t_d is the drift time of the ion, E is the electric field strength, L is the drift length, and N_0 is the number density of the drift gas. Today there exist many variations of IMS that offer different advantages and disadvantages: traveling wave-IMS (TWIMS),[59, 60] drift tube-IMS (DTIMS),[22, 61-63] trapped-IMS (TIMS),[64-66] and field asymmetric-IMS (FAIMS).[67, 68] For the purpose of this work only DTIMS and TWIMS instrumentation will be discussed here.

DTIMS is regarded as the primary standard for IMS measurements of CCS because DTIMS is inherently a first-principles measurement of the CCS. This is because all the variables in DTIMS instrument are held constant allowing for precise determination of CCS based on the drift time of the ion. Ions are accelerated through a low-pressure region of background gas where they are separated based on size and charge. DTIMS remains widely used today as DTIMS instruments tend to be simple to design, build, operate.

TWIMS operating principle is the use of time-dependent switching of DC electrodes to push ions along the drift path.[59] These DC pulses act as electrostatic waves where the ions ride the crests like that of surfers riding wave on a beach. Larger ions tend

to “roll over” these waves and thus will have a slower drift time than that of small ions or ions that are more highly charged. TWIMS differs from DTIMS as it relies on precise calibration curves to calculate CCS of ions.

As mentioned previously, IMS instruments are typically coupled to mass spectrometers as each instrument measures charged gas-phase ions. However, the coupling of these methods can lead to potential issues in analysis time between these methods. Time-of-flight (ToF) mass analyzers operate on a μs time scale (duty cycle) and pair well with IMS because IMS measurements are often in the ms time scale. This allows for ToF mass analyzers to detect many time segments of the mobility drift time. However, even IMS instruments coupled to ToF mass analyzers usually operate at a combined duty cycle of less than 1%. Even still the coupling of IMS to trapped mass analyzers (such as the orbitrap) proves more difficult. There exists a significant duty cycle mismatch between orbitraps (10s-100s of ms) and IMS. To alleviate these issues of duty cycle mismatching, ion multiplexing is employed[69] such as Fourier transform (FT)[70, 71] and Hadamard transform (HT).[72-74] These multiplexing methods allow for higher duty cycles at the expense of more convoluted spectra. Mathematical algorithms are then applied to deconvolute the spectra and retrieve the drift times of ions. Implementation of multiplexing methods have shown the propensity to increase IM-MS duty cycles from less than 1% to 50%.[70]

1.2. Overview of Mass Analyzers commonly used in Native mass spectrometry

Mass analyzers are used in the field of MS to separate gas-phase ions by their respective *m/z*. Some commonly used mass analyzers are quadrupoles, electric or magnetic sectors, time-of-flight (ToF), Fourier transform-ion cyclotron resonance (FT-ICR), linear and 3D traps, and orbitraps. While there exist a plethora of mass analyzers many are limited in their capabilities depending on their application. For nMS, many mass analyzers are often ruled-out due to limits of resolution and high *m/z* analysis. For example, quadrupolar, sector, and trap mass analyzers tend to have low performance at higher *m/z* values, or they are not commonly tuned for this high *m/z* ranges, and while FT-ICR offers ultrahigh resolving power, this is often not useful for larger intact biomolecules. For those reasons, this dissertation will primarily focus on ToF and orbitrap mass analyzers.

1.2.1. ToF Mass Analyzer

ToF mass analyzers operate by measuring the time it takes ions to traverse a drift region and corelating that drift time to its *m/z*. An electric field of known strength is used to impart kinetic energy on the ions. Ions with higher charge and lower mass will be accelerated faster than those with fewer charges and higher mass. **Equation 1-4** described the relationship of kinetic energy to velocity where K_E is kinetic energy, m is mass, and v is velocity.

Equation 1-4

$$K_E = \frac{1}{2}mv^2$$

Ions arriving at the detector (typically an electron multiplier such as a multi-channel plate) have their time counted and *m/z* calculated. Reflectrons can be added to the opposing side of the flight tube to correct for positional variation of ions and increase resolution as they first enter the ToF source region.[75] Ions that happened to receive more energy will penetrate deeper into the reflectron field whereas ions with less kinetic energy will not penetrate as deeply. The conceptual representation temporal refocusing in a reflectron system is demonstrated in **Figure 1.4**. These ions will have a distinct temporal focusing point is ideally identified as the detector, but the strength of the reflectron field can be adjusted change this.

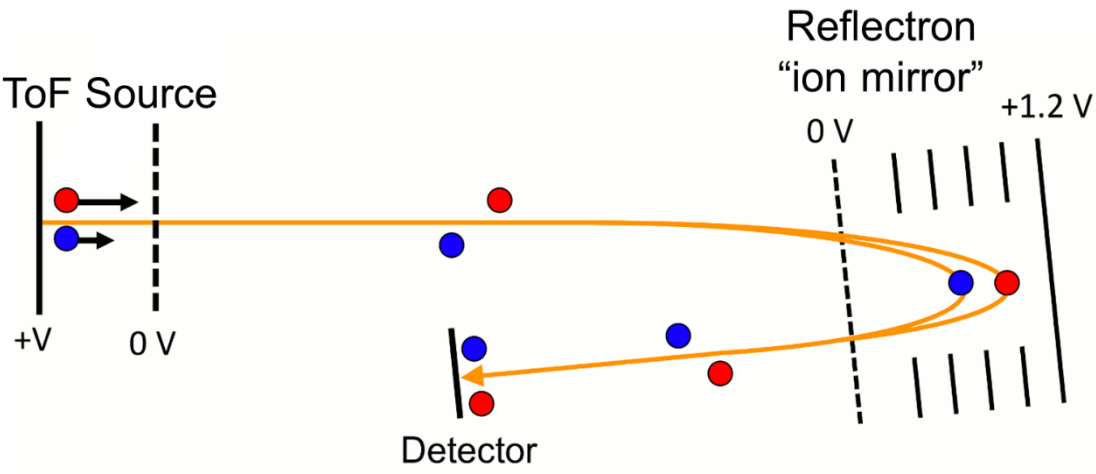

Figure 1.4 Ions of differing initial kinetic energies begin to temporally defocus. The ion with higher kinetic energy (*red*) penetrates deeper into the reflectron field and thus has a longer path length than the other ion (*blue*). Both ions strike the detector at the same time which is the refocusing point of the reflectron.

ToF mass analyzers were first used in 1946 at the University of Pennsylvania by W. E. Stephens.[76] ToF mass analyzers continued to be popular due to their simple theory of operation and construction, but they experienced a renaissance with the rise in popularity of proteomics and ESI. The fast scan rate of ToF analyzers make them

amenable for coupling with LC. With the adoption of nMS, ToF analyzers were well suited as they have no theoretical *m/z* limit and can achieve a resolution of 20,000 to 40,000. ToF mass analyzers continue to be strong candidates for MS instrumentation, and they are nearly ubiquitous in both academic and industrial labs alike.

1.2.2. Orbitrap Mass Analyzer

Orbitrap mass analyzers stem from early ion traps developed in 1923 by Kingdon[77] and then by Knight in 1981.[78] These rudimentary ion traps were instrumental to the development of the orbitrap that is available today. The orbitrap mass analyzer measures *m/z* by detecting fundamental frequencies of ions oscillating inside the trap, which orbit the central spindle. The operating principle is similar to that of FT-ICR,[79] albeit at a much smaller scale and without the need for cryogen. Orbitraps have revolutionized nMS spectrometry by providing high resolution and high *m/z* measurement capabilities without the need for large and costly instrumentation.

Orbitrap *m/z* measurements rely on measuring the fundamental frequency of ions inside the trap; the angular frequency is used for the calculation because axial motion of ions in the trap are not dependent on initial kinetic energy.[80, 81] The angular frequency is defined by **Equation 1-5** where ω is the angular frequency of the ion, k is the force constant (like the spring constant from undergraduate physics).

Equation 1-5

$$\omega = \sqrt{\frac{k}{m/z}}$$

Ions are initially injected into the orbitrap from the preceding c-trap where a short lived, time-dependent separation occurs like in a ToF mass analyzer. The initial ions to reach the orbitrap undergo a process referred to as “electrodynamic squeezing” where the DC voltage of the central spindle is decreased to draw ions that are initially entering the trap progressively closer to the spindle electrode.[80] Once the injection of ions has finished, the ramping of the spindle electrode is stopped and ions form *m/z*-dependent bands based on their angular frequency. The image current induced on the detection electrodes by the coherent oscillation of ions is recorded as a time-dependent signal, which then is Fourier

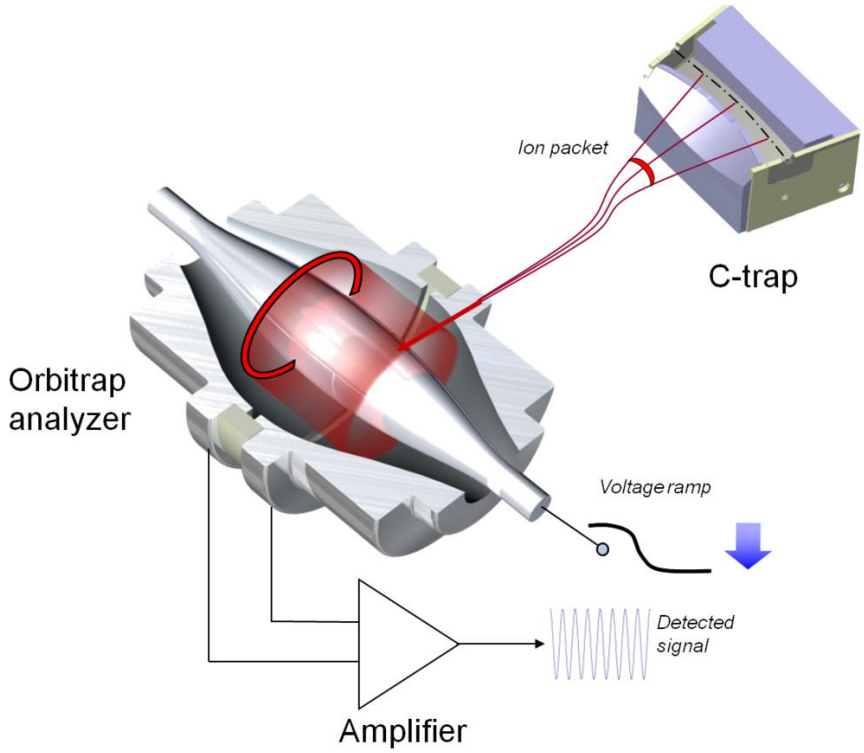

Figure 1.5 Schematic of an orbitrap mass analyzer. Ions injected into the trap begin to oscillate coherently depending on *m/z*. the signal is detected at a time dependent signal which is then converted into the frequency domain. Artwork by Thermo Fisher Scientific

transformed into the frequency domain. These frequencies are used to calculate the respective *m/z* values for all the detected ions. **Figure 1.5** shows how ions are injected from the c-trap into the orbitrap and then how the signal is recorded.

As the limits of nMS are pushed to larger and more complex systems and structures, new methods are required to gain useful information using MS.[82] Heterogeneity in glycosylated proteins and viruses causes severe drawbacks to using nMS as no useful information can be gained due to loss of resolving power.[83] Obitraps, however, have proved useful in the development of new techniques to measure these more heterogeneous systems.[83] Orbitraps, fundamentally detect the charges of ions; ions with more charges impart a larger response on the detection electrodes inside the orbitrap.[84] Orbitraps also have been shown to be capable of detecting individual ions as demonstrated by Makarov et al.[85] If single ions can be detected and the charge of those ions can be inferred from the intensity of the signal, then the mass of the ions can be determined indirectly. This discovery led to the development of charge detection-MS (CD-MS) methods on commercial instrumentation.

While CD-MS capabilities are available in other specifically designed instrumentation,[30, 86] the ability to achieve such a measurement on an already widely adopted system was truly revolutionary. Ions as large as virus capsids have been analyzed to calculate ratios of filled to unfilled capsids. CD-MS is a rapidly growing analysis technique for MDa complexes and highly complex systems, such as glycosylated antibodies.[30, 87-89] CD-MS is beginning to become more widely available with release of direct mass technology (DMT) from Thermo Fisher Scientific. The implementation of

DMT and the widespread enthusiasm from academia and industry alike for CD-MS techniques is opening up new opportunities for nMS to analyze ultra-large biological structures.

1.3. Overview of Thermodynamics in Biomolecular Systems

Thermodynamics, broadly defined, is the study of the flow of energy between a system and its surroundings. When speaking more specifically about biochemical systems, thermodynamics is often employed to understand fundamental mechanisms and driving forces that govern molecular structure and function. All biomolecules exist in a Gibbs free energy landscape (FEL) that is primarily defined by pressure, temperature, and concentrations of the solution constituents.[90, 91] By changing any of these variables the native structure of biomolecules can be perturbed into adopting a new native structure for those given conditions.[92] Thermodynamic quantities of interest in biochemistry are enthalpy, entropy, Gibbs free energy, and heat capacity. **Equation 1-6** and **Equation 1-7** show how these quantities are related.

Equation 1-6

$$\Delta G = \Delta H - T\Delta S$$

Equation 1-7

$$C_p = \frac{\Delta H}{\Delta T}$$

Where ΔG is the Gibbs free energy, ΔH is the change in enthalpy, T is temperature, ΔS is the change in entropy, and C_p is the heat capacity of the system at constant pressure. These values are important for understanding thermodynamic mechanisms of systems and are important for studying protein/ligand and protein/protein interactions.

1.3.1. Enthalpy, Entropy, and Gibbs Free Energy

Enthalpy is defined as the total internal energy of a system; in respect to biochemistry, enthalpy can be explained as the total amount of energy in a system related to the formation of bonds (H-bonds, salt-bridging, Van der Waals, ect.). When enthalpy is measured, it is reported as ΔH or the overall change in enthalpy. Positive enthalpy denotes the formation of unfavorable, higher-energy bonds while negative enthalpy denotes the formation of more favorable, lower-energy bonds. While enthalpy is fundamentally a state function—meaning that the overall change is independent of the energetic path taken to arrive at the final value—it is still an important quantity that is often used to characterize protein/ligand binding. Isothermal titration calorimetry measures the change in temperature of a solution as a solution of a ligand is titrated into it.[93, 94] The binding curve that results from the temperature changes allows for the determination of the enthalpy of the binding interaction as well as entropy and Gibbs free energy. **Equation 1-8** defines this relationship where R is the universal gas constant and K_a is the binding affinity of a given ligand.

Equation 1-8

$$\Delta G = -RTlnK_a = \Delta H - T\Delta S$$

Enthalpy is often static over small temperature ranges of a few degrees but tends to vary over larger changes in temperature. This is because temperature is an important variable for defining the conformational preferences of proteins. When proteins undergo a conformational change, enthalpy terms will differ as a result. This tendency for the enthalpic term to change as a function of temperature is defined as the heat capacity.[95-97] Differential scanning calorimetry (DSC) measures the amount of energy input to

increase the temperature of a solution as a function of measured solution temperature.[96] Thus, the energy input as a function of solution temperature can be correlated to how much energy was added to solution that did not lead to an increase in the temperature, i.e., the heat capacity of the solution constituents. DSC is an excellent tool for measuring ΔC_p of

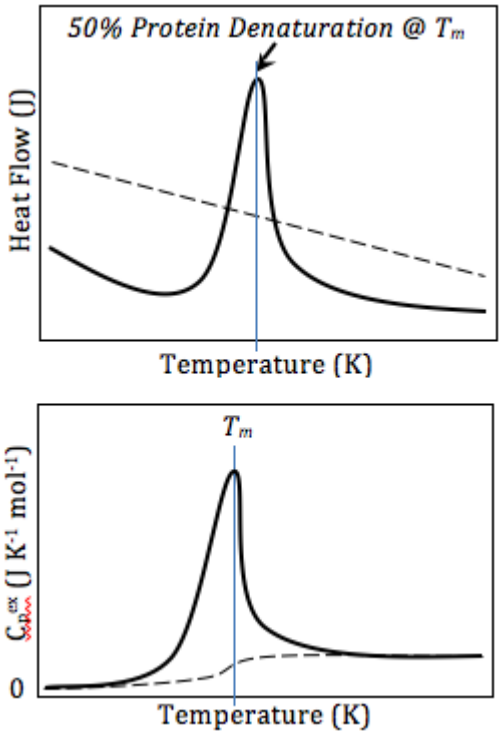

Figure 1.6 Example of DSC melting curves of proteins as they undergo thermal denaturation. *Top* is the heat flow as a function of temperature and *bottom* is the heat capacity of the solutions as a function of solution temperature. As energy is added to the solution proteins can absorb some of this energy through the destabilization of internal bonds. This signature is a direct result of a change in heat capacity of the protein.

proteins as they undergo unfolding reactions (**Figure 1.6**). Unfolding transitions produce large and obvious signals as when proteins unfold, they absorb additional heat being added to the solution which leads to the disintegration of stabilizing interactions.

Entropy can be defined simply as the level of disorder in a system. Biologically speaking, entropy controls many intracellular interactions and is responsible for the main stabilizing force of protein native structure—hydrophobic interactions. Entropy is theorized to be the main driving force of hydrophobic interactions due to unfavorable interactions between hydrating waters and hydrophobic moieties.[90, 98-100] The hydration water for these hydrophobic regions exists in a higher energy, a more ordered state. The expulsion of this hydrating water leads to more favorable hydrogen bonding in the bulk water and hydrophobic collapse of the protein. Even though the entropic state of the protein increased upon folding, the overall entropy including the expulsion of water molecules is negative for this interaction. Frank and Evans articulated this in 1964,[101] describing the highly ordered hydration water as "iceberg water."[102] Interestingly, but not surprisingly, the hydrophobic effect is temperature dependent as demonstrated by Privolov.[103] Colder temperatures lead to a weakening of the hydrophobic effect as water intercalates into the structure; such a process is referred to as "cold denaturation." This process is somewhat intuitive as the magnitude of the entropy term is tied to the temperature, so as the temperature decreases so does the magnitude of the entropy term.

Gibbs free energy is the total energy of the system from both the enthalpy and the entropy at a given temperature and constant pressure. It is often taught as being the defining thermodynamic quantity in the study of equilibrium thermodynamics. However, solely focusing on Gibbs free energy often means that entropy and enthalpy values are overlooked. Gibbs free energy values in biochemical systems often do not vary much due to a phenomenon known as enthalpy-entropy compensation (EEC).[104, 105] Many

theories have been proposed to explain this phenomenon, but for biological systems it is theorized that EEC is due to nature of water.[106-109] For example, if water molecules are located in a binding region as a ligand comes to bind to the pocket, the water will be displaced and new bonds between the protein and ligand will be formed. If the binding pocket was hydrophobic then the entropy term will be large because water has been removed from a hydrophobic interface and enthalpy will be smaller because hydrophobic interactions are relatively weak. If the binding pocket was hydrophilic then the entropy will be small or negative as the ordering of a ligand and removal of water from hydrophilic regions are entropically unfavorable, but the enthalpy will be large because hydrophilic interactions are relatively strong. Measurements of Gibbs free energy often obscure the underlying dynamic nature of EEC that may be important for a deeper understanding of the thermodynamic mechanisms of a system.

1.3.2. The Variable-Temperature ESI Device

NMS offers an excellent opportunity to use the sensitivity and specificity of mass analyzer as a detector for products of solution-phase reactions. Several iterations have been designed of a variable temperature ESI (vT-ESI) source designed to modulate the temperature of a solution as it is being analyzed by a mass spectrometer.[8, 110, 111] This enables the direct observation of temperature-dependent products and conformational transitions when coupled to an IM-MS instrument. Dispersion of products in an *m/z* dimension affords the assignment of specific products, whereas solution-phase measurement report on the ensemble average of products in solution, making specific

assignments on complex systems difficult. VT-ESI coupled to MS has already been shown to be beneficial for thermodynamic studies on protein/ligand reactions and protein melting transitions.[8, 11, 13, 14, 110, 111]

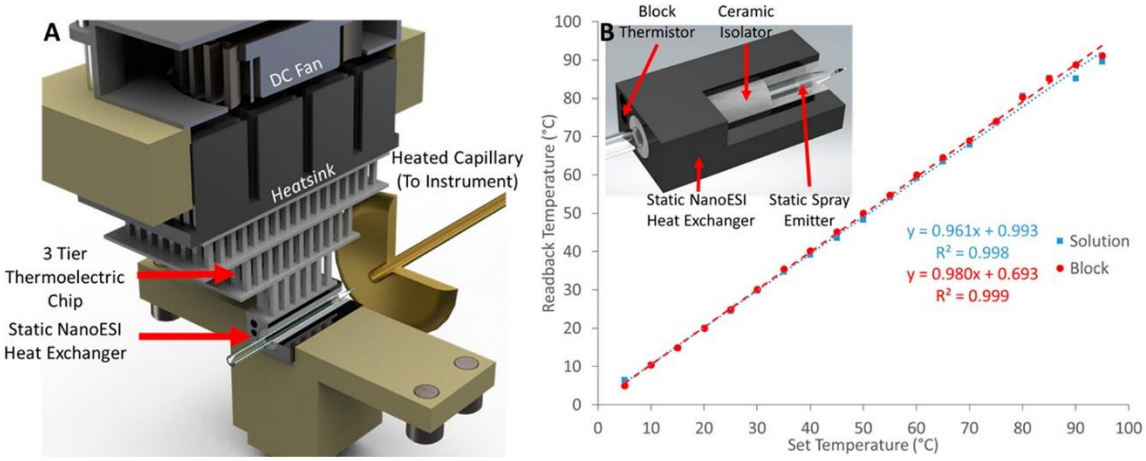

Figure 1.7 (A) Solidworks rendering of the vT-ESI assembly with labels to identify the significant components. The fan mounted to the top of the device prevents overheating and reduces atmospheric moisture condensation for experiments performed below ~15 °C. The top stage of the thermoelectric chip (TEC) makes direct contact with a heatsink; a 24 VDC fan with is used to dissipate the heat from the heatsink. The vT-ESI assembly uses custom machined PEEK components that mount directly to a commercial Thermo Nanospray Flex source. (B) Temperature calibration of the vT-ESI emitter solution is performed using thermocouples inserted into the static spray capillary and the SS heat exchanger (as shown in the inset).

McCabe et al developed a new vT device that can heat and cool nESI emitters in a rapid and controlled manner.[13] This allows for the examination of temperature dependent interactions in cold and hot conditions. **Figure 1.7A** contains a Solidworks rendering of the vT-ESI assembly using nESI emitters. The nESI emitter is positioned inside a ceramic sleeve (Kimball Physics (AL2O3-TU-C-500) and cut to length in-house) that serves as an electrical insulator from an aluminum heat exchanger. The heat exchanger makes direct contact with a three-stage TEC (Peltier chip) (Laird Thermal Systems 9360001-301 three-tier). The TEC is used to maintain the temperature of the heat

exchanger and the solution contained in the ESI emitter at the desired temperature, ranging from ~5−98 °C. The vT-ESI capillary temperature was calibrated across the range of temperatures by simultaneously monitoring the static-spray (SS) heat exchanger temperature and the solution contained in the ESI emitter (**Figure 1.7B**). The solution temperature was measured using a calibrated T-Type thermocouple (Physitemp Clifton, NJ) paired to a thermocouple (National Instruments USB-TC01) positioned inside the borosilicate pulled glass capillary filled with a 200 mM ammonium acetate solution.

1.4. Overview of Chaperonin 60 GroEL

1.4.1. GroEL as a Protein Folder

Chaperonins are a class of protein complexes found in all living systems that recognize and bind non-native proteins and assist in the folding of the protein to more stable, native state(s), thereby inhibiting misfolding and aggregation. GroEL, an *E. coli* chaperone, is an archetypal system for understanding molecular chaperones. When bound to its co-chaperonin, GroES, a heptameric complex that binds to the apical domain of GroEL, this complex promotes proper folding of the nonnative substrate protein. The structure of GroEL consists of two heptameric stacked rings, and each subunit consists of three domains—apical, intermediate, and equatorial.[112-114] The apical domain is highly dynamic and is responsible for binding protein substrates and the co-chaperonin GroES. The intermediate domain acts as a hinge between the equatorial and the apical regions of each subunit, and the equatorial domain of each subunit is the least dynamic and serves as the interfacial contact between each heptameric ring.[115-118] The

equatorial domain also harbors the ATP binding site for each subunit. The stucure of GroEL and the conformational transitions asscoiated with ATP binding are displayed in **Figure 1.8**.

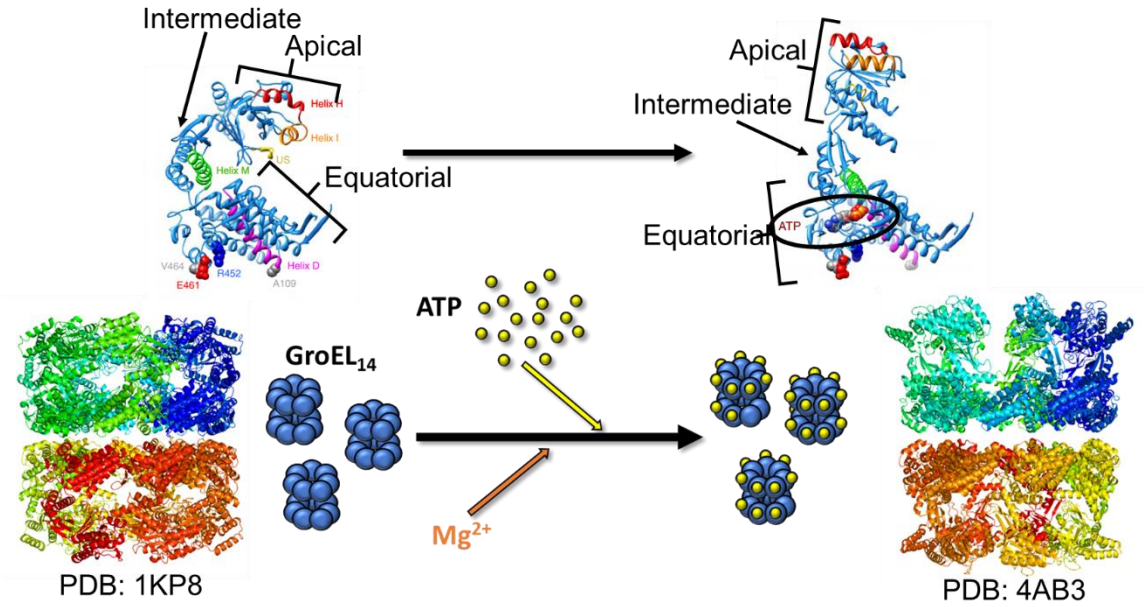

Figure 1.8 (*top*) The structural transitions of the monomers of GroEL is shown. Much of the conformational change is associated with the extensions and twisting of the apical domain when ATP is bound to the equatorial domain. (*bottom*) The change in the overall structure of the tetradecamer is shown upon the binding of ATP.

The accepted mechanistic understanding for the GroEL nano machine (**Figure 1.9**) is that upon binding of ATP the apical domain undergoes a conformational transition, extending a twisting to exposed hydrophobic patches. This conformational change allows the GroEL to recognize and bind unfolded substrates. Upon the capturing of a substrate protein, GroES then binds to the top of the cavity, completely encapsulating the protein. The GroEL-GroES-substrate complex then undergoes ATP hydrolysis with promotes the release of the substrate into the cavity and provides an "Anfinsen cage" environment, or Arthur Horwich describes "it is as if the protein is in a sea of infinite solvent."[119] Post-

hydrolysis, ATP can bind to the *trans*-ring of the complex which destabilized the *cis*-ring conformational integrity, leading to the release of the ADP, GroES, the now-folded protein. This process can continue if GroEL can access ATP, and GroES.

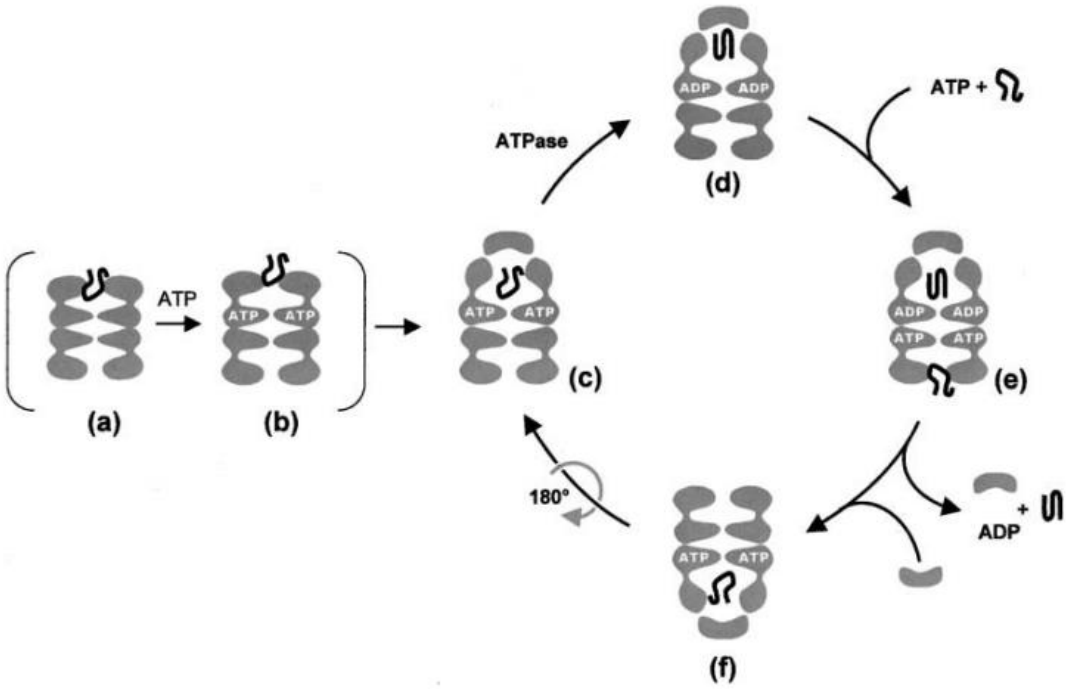

Figure 1.9 a) Substrate protein is captured by the GroEL. b) ATP is bound to the *cis* ring enabling c) the binding of GroES to capsulate the protein. d) The complex undergoes ATP hydrolysis which promotes the protein to fold. e) More substrate and ATP bind to the *trans* ring, f) destabilizing the *cis* ring and releasing ADP, folded protein, and GroES. The process then can begin again at (c).

1.4.2. Mechanisms of GroEL-ATP Interaction

Many studies have been dedicated to the understanding of the GroEL-ATP interaction. It is arguably the most important interaction for GroEL as is it an ATPase driven protein complex. Early studies focusing on the GroEL-ATP interaction were primarily pioneered by Amnon Horovitz and George Lorimer in the early and mid-

1990s.[120-124] In 1995, Horovitz et al. coined the term "nested-cooperativity" to describe the way in which ATP was observed binding to GroEL.[121] They posited that GroEL bound ATP in the initial ring (*cis*-ring) in a highly cooperative manner and that binding to the second (*trans*-ring) was disfavored via a negatively cooperative interaction. This would mean that intra-ring binding of ATP by GroEL was governed via a concerted mechanism and that inter-ring ATP binding was subject to a sequential binding mechanism.

The concerted or MWC model—proposed by Monod-Wyman-Changeux—of ligand binding postulates that the binding of one ligand to a protomer (subunit) induces changes in affinity for all the other protomers collectively into a relaxed (R) or tense (T)

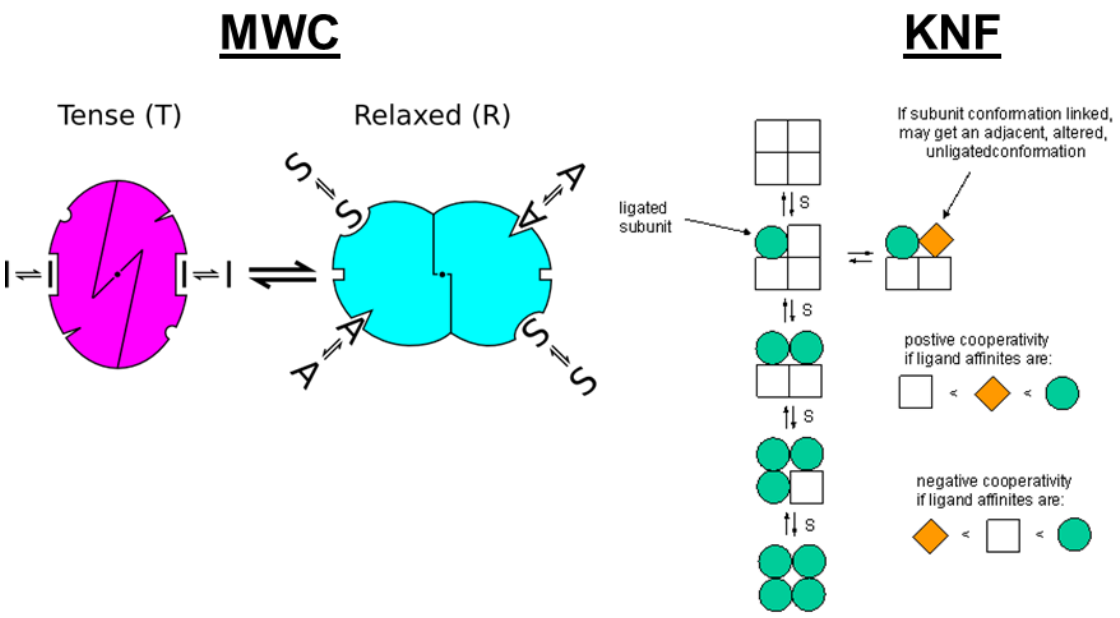

Figure 1.10 (*left*) The MWC model demonstrating a multi-ligand system that exists in an equilibrium between either tense (T) or relaxed (R) states. (*right*) The KNF model is more nuanced model allowing for allostery to promote positive or negative cooperativity in adjacent subunits rather than it being an all-or-nothing reaction like the MWC model.

state (**Figure 1.10**).[125] It was first proposed as an explanation for the sigmoidal binding pattern observed for the binding of oxygen by hemoglobin.[126] In contrast, the sequential or KNF model—proposed by Koshland-Nemethy-Filmer—argues that the binding of a ligand to a subunit will only have immediate effect (positive or negative) on its neighboring subunits (**Figure 1.10**).[127]

1.5. Overview of Osmolytes

Osmolytes are small biomolecules that are responsible for regulating many cellular functions as well as conditions in the cellular environment. Two well-studied osmolytes are trimethylamine *N*-oxide (TMAO) and urea. TMAO tends to stabilize native structures of proteins and promotes folding of proteins.[128-132] Urea tends to destabilize protein structure, especially in higher concentrations, and is actively removed from the cells of most animals.[131, 133] These two osmolytes compete against each other in a chemical sense; for this reason, marine animals, which carry higher average concentrations of urea in their bodies, produce elevated levels of TMAO to combat the damaging effects of high urea concentrations.[134, 135] Several studies have proposed that each molecule of TMAO is able to counteract the effects of 2 urea molecules.[134, 136, 137]

Despite the long-standing knowledge of TMAO and urea and their abilities to influence protein structure, there is still debate as to how these osmolytes specifically interact with proteins and peptides. The two main mechanistic propositions for these osmolytes are grouped generally as direct or indirect mechanisms. The direct mechanism theories propose that the osmolytes are interacting with the protein or peptide itself

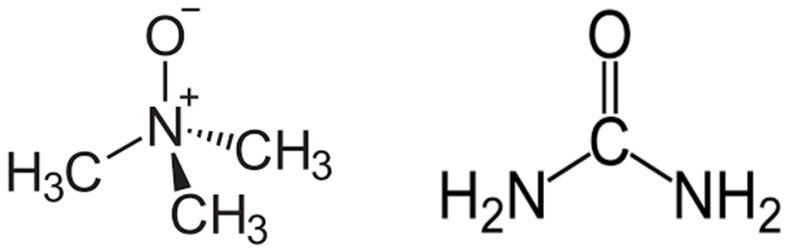

Trimethylamine *N*-Oxide (TMAO) 75 Da

Urea 60 Da

Figure 1.11 Structures and mass of TMAO (*left*) and urea (*right*). TMAO acts as a stabilizing osmolyte while urea is known to induce protein denaturation.

through manipulation of the residues and/or the peptide backbone. Studies from several sources using MD simulations and thermodynamic studies suggest that direct interaction adequately explains observed effects.[138-143] In the case of TMAO studies propose that thermodynamic stabilization through non-preferential interactions with side chains explain TMAO's stabilizing tendencies.[130, 131] The indirect mechanism proposes that osmolytes influence the larger water structure around the protein or peptide, which in turn then affects the structure of the protein/peptide. Studies have reported that TMAO could strengthen local water structure while other studies show that TMAO could act as a nanocrowding agent that drives water from and promotes folding of hydrophobic regions of proteins.[128, 144] Franks *et al.* reported that hydrocarbons are more soluble in urea/water solution than in pure water; this observation has been extrapolated to suggest that urea may denature proteins through increasing solvation of the peptide backbone in solution.[145] However, according to Canchi et al., there is likely no direct experimental evidence for an indirect mechanism of urea effect on protein/peptide structure.[146]

1.6. Overview of Cryo-IM-MS

1.6.1. Operating Fundamentals of Cryo-IM-MS

Experimental and theoretical studies underscore the importance of both long- and short-range interactions between ligands, solutes, and biological molecules.[147-151] However, a detailed understanding of the effects of water on protein structures, stabilities,

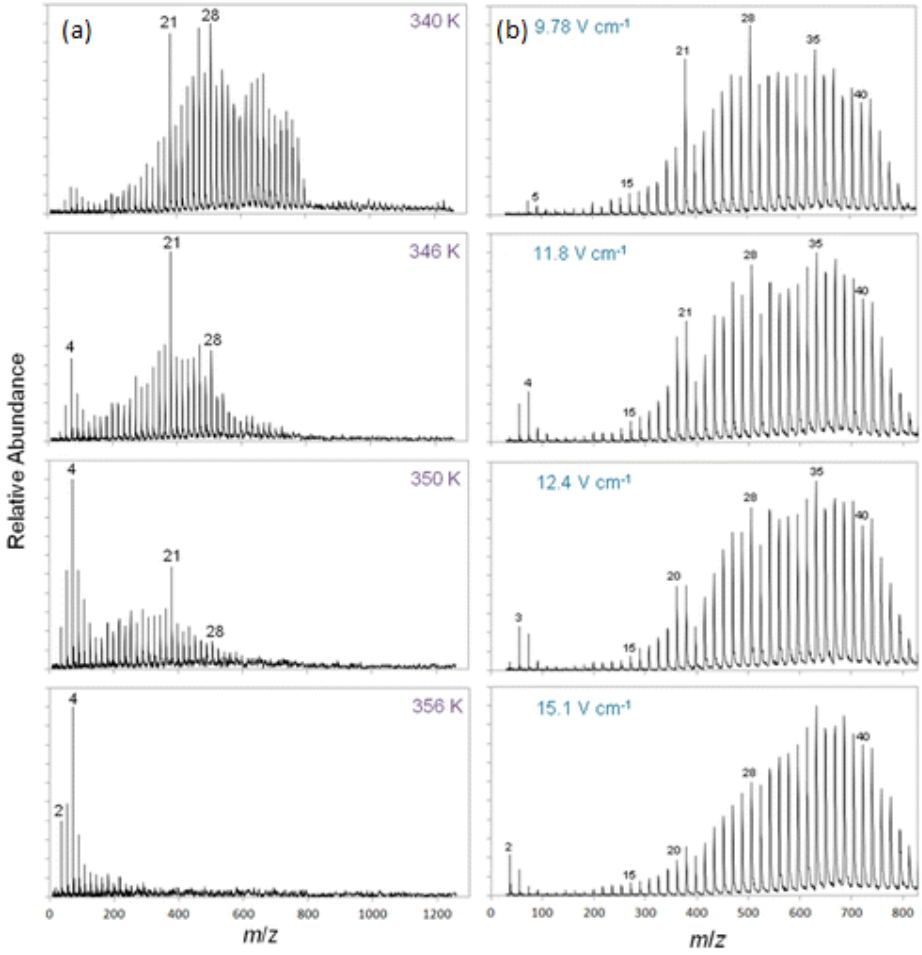

Figure 1.12 Mass spectra of protonated water clusters at (a) variable heated capillary temperatures and (b) variable IM field strengths. The field strength in (a) is 9.12 V/cm and the heated capillary temperature in (b) is 340 K. Adapted with permission from ref. 60. Copyright 2013 American Chemical Society.

dynamics, and functions is largely confined to the effects of bulk solvent and specific cases where a limited number of localized water molecules, referred to as "biological water,"[152, 153] interact with the protein backbone and/or specific amino acid side chains.[154-157] The ability to experimentally probe the effects of solvation on peptide and protein structure across the range of "bulk-like" water (where species are hydrated

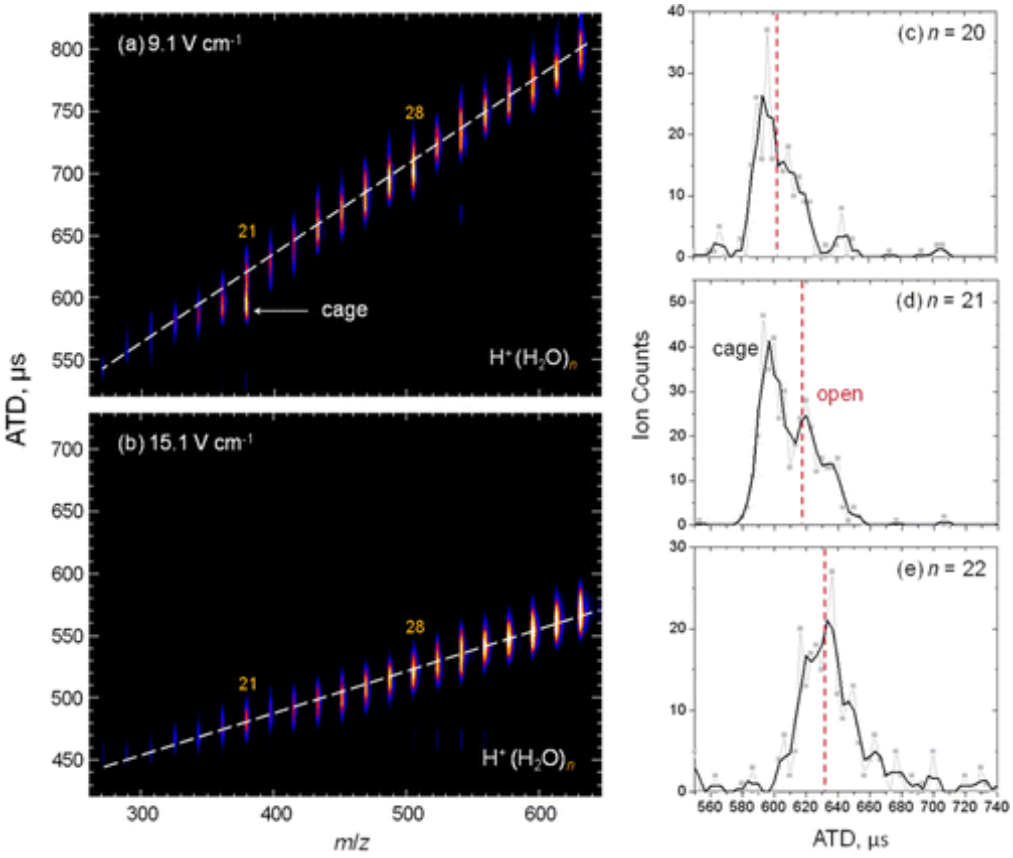

Figure 1.13 ATD vs *m/z* plot for $H^+(H_2O)_n$ (n = 15 to 35) produced at an electric field of (a) 9.1 V cm^{-1} and (b) 15.1 V cm^{-1} in the drift tube at a heated capillary temperature of 340 K. Panels c–e contain the mass-selected ATDs for (n = 20 to 22) at 9.1 V cm^{-1}. The black line is the result of boxcar averaging of the data points (gray). The vertical dashed line was inserted to guide the eye across the centroid of the IM-MS trendlines shown. Copyright 2013 American Chemical Society.

beyond the first solvent shell) to a small number of water molecules has the potential to provide new insights as to the role water plays in biological structure and functionality.

Cryo-IM-MS is a technique that employs cryogenically cooled IMS and MS to study late-stage desolvation structures of ions produced from ESI. A key component of the cryo-IM-MS experiment is the preservation of the hydration waters around the analyte of interest (**Figure 1.12**). Notably, these experiments observe the "freeze-dried" ions that form during the transition from the solution to gas phase. This observation was articulated by Beachamp et al. who observed solvated ions produced via ESI.[18, 19] The stepwise solvent evaporation is visualized as a near monotonic trendline in **Figure 1.13** and by **Equation 1-9**.

Equation 1-9

$$[M\ +\ H] + (H_2O)_x \rightarrow [M\ +\ H] + (H_2O)_x - 1\ +\ H_2O$$

The specific *m/z* shifts observed for water (m = 18 Da) allow for the identification of the charge states of hydrated ions without the need for isotopic resolution. The cryo-IM-MS utilizes cryogenically cooled helium gas (about 80 K) to preserve structured water around the ion in the gas phase. Previously, cryo-IM-MS was used to study structural transition in water networks around small peptide ions as a function of the number if retained solvation waters.

1.6.2. Instrument Design of Cryo-IM-MS and Improvements to Existing Instrumentation

The instrument schematic is displayed in **Figure 1.14**. Ions are introduced via ESI into the heated capillary which is used to control the level of solvent adduction on the ions by raising or lowering the temperature. Previously, ions traversed through and skimmer into DC ion guide, which uses a series of alternating high and low DC potentials to transport them to the drift tube. However, recent design changes mean that the DC ion guide has been replaced by an octupole which has aided overall signal transmission. Ions then enter the cryogenic-DT where they undergo separation based on size and charge. After exiting the drift tube, ions enter the ToF source where they are analyzed based on *m/z*. ToF pulses are interleaved with each successive IM pulse to ensure higher resolving power for the IM measurement.

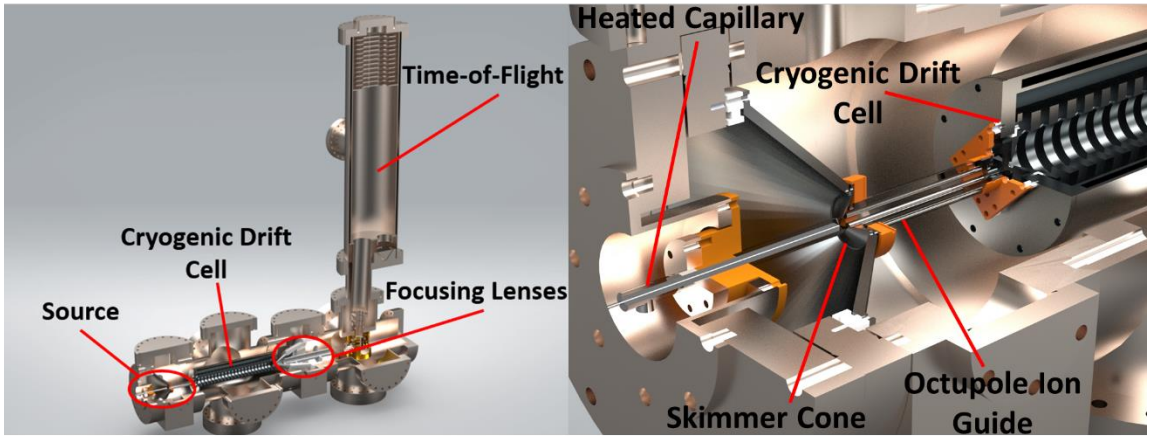

Figure 1.14 Quarter-section views of the cryo-IM-MS with the Jordan TOF and the octupole ion guide. The entire instrument is shown (*left*): notable features are the source, cryogenic drift tube, focusing lenses (Einzel lenses), and the Jordan reflectron-TOF. (*right*) A zoomed-in look at the octupole situated between the heated capillary source and the entrance to the drift tube.

The duty cycle of cryo-IM-MS is extremely low (< 1%) owing to the signal averaging (SA) measurements for the IM experiment. Combined with already low singal intensity, the overall performance of cryo-IM-MS meant that spectra required several hours to collect. This provided the impetus for implementing HT as a way to improve the duty cycle of the IM-MS experiment. HT operates by applying a "pseudo-random" pulsing sequence to the IM gate, which allows multiple ion packets to enter the IM analyzer, leading to the overrunning of multiple packets together.[72, 73] However, because the sequence is known prior, the complicated IM spectrum can be deconvoluted to yield the arrival time distributions (ATD) of the ions traversing the DT. The implementation of a HT pulsing scheme increased the duty cycle up to 33% experimentally, allowing for an IM-MS spectrum to be acquired in 20 minutes that would have taken 5 hours previously in a SA mode.

2. ENTHALPY-ENTROPY COMPENSATION AND TEMPERATURE-DEPENDENT TRIMETHYLAMINE N-OXIDE INDUCED FORMATION OF SUBSTANCE P DIMERS THROUGH INDIRECT INTERACTION

2.1. Abstract

Interactions of the peptide substance P (SP) (RPKPQQFFGLM-NH2) and TMAO were investigated using variable-temperature- electrospray ionization-ion mobility-mass spectrometry. Solutions containing SP and TMAO yield abundant hydrated SP dimer ions, but dimer formation is inhibited in solutions that also contain urea. We show that SP dimer formation at cold solution temperatures (<273 K) suffers a reduced entropic penalty when compared to warmer solution conditions (>293 K).

2.2. Background

Osmolytes are small organic molecules that influence many of the fundamental characteristics of cytoplasm within the cell.[158, 159] The osmolyte, trimethylamine N-oxide (TMAO), has been shown to protect folded protein states[128, 129, 131, 136, 160-162] and to assist refolding denatured proteins.[132] These actions are thought to influence structure by crowding out water around proteins, thereby entropically favoring folded conformations by promoting hydrophobic interactions,[128, 163, 164] and these effects have been shown to counteract denaturing effects of urea.[134, 135, 146, 161, 165-167] While much has been learned concerning the effects of osmolytes on protein structure, stabilities, and dynamics, the specific mechanisms of interactions between osmolytes and proteins/peptides remain unresolved. Generally, two broad types of osmolyte-protein interaction are entertained, *viz.*, direct and indirect interactions.[131,

146] Direct interactions are thought to disrupt local structure of proteins through interactions with the amino acid side chains or the peptide backbone, whereas an indirect mechanism invokes disruption of the water structure[168, 169] or the solvation shell of the protein.[170] Some researchers have attributed the denaturing effects of urea to direct interaction between urea and the peptide backbone and destabilization of hydrogen bonds between amino acid residues.[142, 171-175] In a recent review article Shea and co-workers provide new perspectives on the mechanism(s) of TMAO counteraction of urea-induced protein denaturation.[131] Here, we employ a combination of cryogenic-ion mobility-mass spectrometry (cryo-IM-MS)[176-179] and variable-temperature (vT)-ESI-IM-MS[13] to investigate the effects of TMAO and urea on the hydration of the peptide substance P (amino acid sequence RPKPQQFFGLM), a member of the tachykinin family of neurotransmitters.[180] The results obtained using vT-ESI reveal strong temperature-dependent reaction products, *viz.*, formation of a SP dimer at cold temperatures (< 298 K) and formation of a $[SP\text{-}TMAO]^{2+}$ complex with each exhibiting enthalpy-entropy compensation (EEC).[96, 108]

Cryo-IM-MS was previously used to investigate the effects of hydration on the conformational preferences of peptide ions during the transition from solution to the gas phase.[176, 177, 181-184] Hydrated peptide ions are generated by ESI involving a process described as “freeze-dried biomolecules”,[19] and the hydrated ions are retained in the cold (~80 K) IM drift tube. We previously showed that the hydrophilic N-terminus (RPKPQQ-) of the $[SP + 3H]^{3+}(H_2O)_n$ is hydrated (n = 0 - < 100) and the amidated C-terminus (-FFGLM-NH_2) is dry.[181] Results from molecular dynamics simulations

provided evidence that the side chains of glutamine (QQ) and *cis/trans* preferences of the two prolines afford stabilization of specific conformer and hydration of the ions.[177-179, 185, 186] On the basis of these prior studies we asked the following question—does the presence and/or absence of osmolytes, *e.g.*, TMAO and urea, alter the structure, stability, and hydration of the SP ions? Here, we extend these earlier studies to include the effects of osmolytes on the hydration of SP ions.

2.3. Results and Discussion

Arrival time distribution (ATD) vs. *m/z* plots for a 50 μM SP aqueous solution (pH ~ 7) obtained using cryo-IM-MS are shown in **Figure 2.1A**; these data are very similar to those reported previously for SP.[177] Note that both $[SP + 2H]^{2+}$ and $[SP + 3H]^{3+}$ ions are hydrated and retain 85-100 water molecules. **Figure 2.1B** contains similar data obtained from a solution (50 μM SP and pH ~7) containing urea (50 μM), hereto all ions are assigned as hydrated $[SP + 2H]^{2+}$ and $[SP + 3H]^{3+}$. **Figure 2.1C** contains data for a solution of SP and 1 μM TMAO; note the presence of both hydrated ions for $[SP + 2H]^{2+}$ and $[SP + 3H]^{3+}$ ions as well as signals for a hydrated SP dimer, $[2SP + 4H]^{4+}$. The assignment of these ions as a dimer is possible because the clusters are spaced by 4.5 *m/z* units (see **Figure 2.5**). Note the reduction in abundances of $[SP + 3H]^{3+}(H_2O)_n$ for *m/z* < 700. **Figure 2.1D** contains data for a 50 μM SP solution containing 1 μM urea and 1 μM TMAO. The $[2SP + 4H]^{4+}$ dimer ions are observed but their abundance is diminished upon addition of urea indicating that the TMAO-induced dimer formation is inhibited by the presence of urea, further evidence regarding the counteracting effects of TMAO and urea.

Results from cryo-IM-MS experiment provides information regarding extent of hydration of the SP peptide; however, the signal-to-noise ratios (S/N) for the hydrated ions are low owing to signals being dispersed over many signal channels. To better understand the effects of TMAO on SP, experiments were conducted using an ambient IM-MS (Waters Synapt-G2 TWIMS (traveling wave-IMS)-ToF instrument). While this

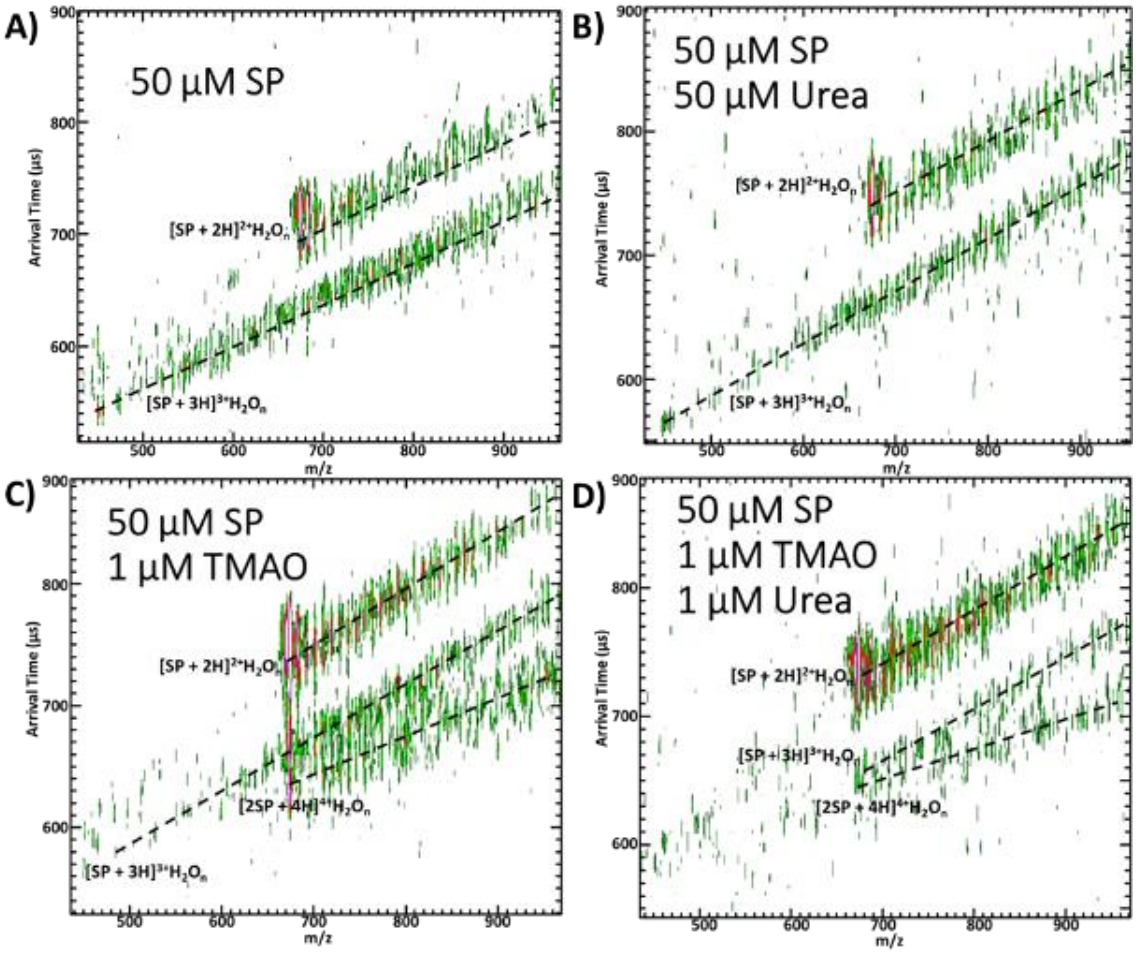

Figure 2.1 Plots showing arrival-time distributions (ATD µs) vs. m/z for SP water clusters obtained from solutions of A) 50 µM SP, B) 50 µM SP with 50 µM urea, C) 50 µM SP with 1 µM TMAO, and D) 50 µM SP, 1 µM TMAO, and 1 µM urea. Note: the appearance and disappearance of the SP dimer when comparing the various experiments with and without TMAO. Collectively, these data illustrate effects of TMAO-induced SP dimer formation and the counteraction disruption by urea.

instrument does not allow for detection of the hydrated ions, it does afford greater sensitivity and dynamic range as well as higher mass resolution. Moreover, ambient IM-MS is capable of dispersing overlapping signals[22, 187] for monomer and dimer of SP ions, and when combined with vT-ESI it is possible, using Van't Hoff analysis of the data, to determine changes in Gibbs energy ($\Delta G = \Delta H - T\Delta S$) arising from the presence or absence of TMAO. Effects of urea can be inferred by changes in the products formed by interactions involving SP/TMAO, but these are more difficult to quantitate because product ions containing urea are not detected. **Figure 2.2A** contains ATD vs. *m/z* plot illustrating separation of the monomer and dimer ions of SP, and **Figure 2.2B** contains extracted mass spectra for $[SP + H]^{1+}$ and $[2SP + 2H]^{2+}$ ions obtained from solutions

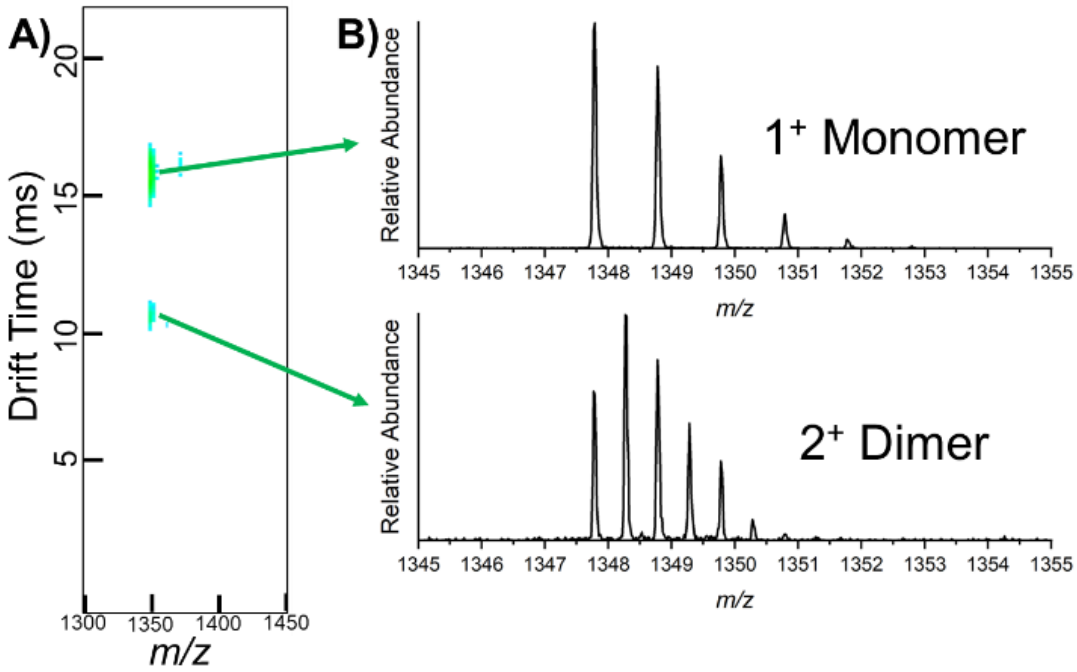

Figure 2.2. A) Two-dimension plot showing ATD (µs) vs. *m/z* for 5 µM SP with 0.1 µM TMAO in water collected on the Synapt-G2. There are 2 distinct peaks that have matching *m/z* values but have varying ATDs. B) Extracted mass spectrum of the 2 mobility peaks shown in A. The isotope distributions demonstrate the formation of the dimer.

containing SP and TMAO, 5 µM and 0.1 µM, respectively. $[SP + H]^{1+}$ ions are observed when using the Synapt-G2 due to higher sensitivity compared to cryo-IM-MS and the capacity for TMAO to be an effective charge reducing reagent.[188] Increasing the concentration of TMAO in the solution led concomitantly to an increase in the relative abundance of the $[SP + H]^{1+}$ and $[2SP + 2H]^{2+}$ ions. Even at the lowest concentrations of added TMAO (0.1 µM TMAO (50:1 ratio of SP:TMAO), TMAO induced formation of SP dimers is observed. In neither cryo-IM-MS or ambient IM-MS spectra do we find products indicative of TMAO bound to the dimer state of SP.

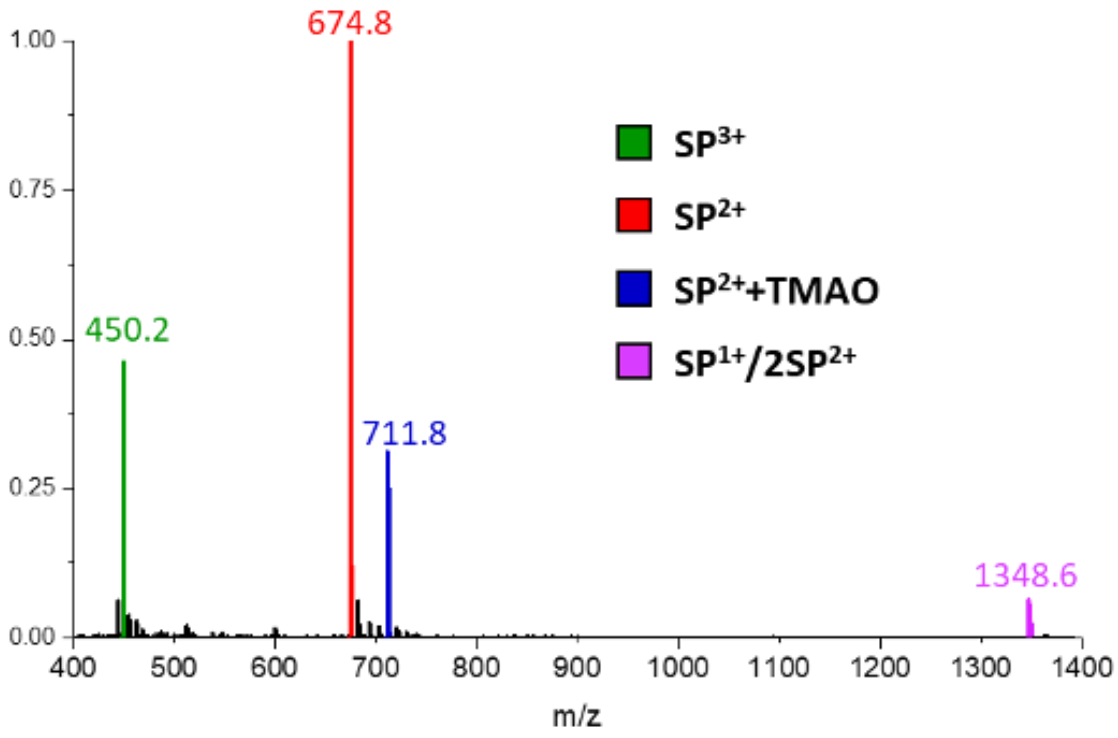

Figure 2.3 Mass spectrum obtained for an aqueous solution containing 5 µM SP and 500 µM TMAO at 293 K. The signals used for the calculation of the thermodynamic constants are highlighted in various colors. The *m/z* values for the respective peaks are given above each respective peak.

Temperature dependence for SP dimer formation was investigated further using the vT-ESI device, as described previously.[12, 13] The thermodynamic effects of solution temperature for a solution of 5 µM SP and 500 µM TMAO were analyzed using a Synapt-G2 instrument at solution temperatures between 278 K to 358 K. The 278 K solution temperature coincided with the highest relative abundance of SP dimer ions, and further increases in the solution temperature decreased the relative abundance of $[2SP + 2H]^{2+}$ ions. The lowest relative abundance of dimer ions was measured at 358 K. A spectrum obtained at T = 293 K is shown in **Figure 2.3**. The temperature-dependent data suggest that lower solution temperatures favors SP self-assembly in the presence of TMAO.

Van't Hoff plots (**Figure 2.4A**) are evidence that formation of the SP dimer in the presence of TMAO at both low and high temperatures is subjected to an entropic penalty, but favorable enthalpy overcomes the entropic barrier resulting overall negative ΔG (Table S1); ΔH = -71.1 kJ/mol, $-T\Delta S$ = 53.6 kJ/mol (293 K), and ΔG = -17.5 kJ/mol (293 K) (low temperture trend). It is interesting to note, however, that the Van't Hoff plots are bimodal, showing a distinct change for solution temperatures below 293 K. The deviations at higher temperature are plotted separately, signifying that the cold temperature formation of the dimer is preceded by a different mechanism than that at higher solution temperatures; ΔH, $-\Delta TS$, and ΔG at 293 K are -26.4 kJ/mol, 8.8 kJ/mol, and -17.6 kJ/mol, respectively (high temperature trend). These data are an example of EEC where even though the entropy and enthalpy contributions change (warm vs cold trends) the overall Gibbs free energy is unchanged.

At high concentrations of TMAO (500 µM) ions corresponding to $[SP\text{-}TMAO]^{2+}$ are detected, and the Van't Hoff plots are shown in **Figure 2.4B**. At low temperatures, the relative abundance of the $[SP\text{-}TMAO]^{2+}$ complex exhibits small changes, followed by much larger changes T > 298 K. The Van't Hoff plot for the $[SP\text{-}TMAO]^{2+}$ complex shows a similar pattern to that observed for the $[2SP + 2H]^{2+}$ complex (Figure 4A), *i.e.*, non-linear Van't Hoff plots. Note that the shallower slope of K_a for cold solution temperatures is observed and plotted between 278 - 298 K. The second slope for K_a is defined for temperatures 298 K to 353 K. From the fitted data we obtain thermodynamic values (ΔH

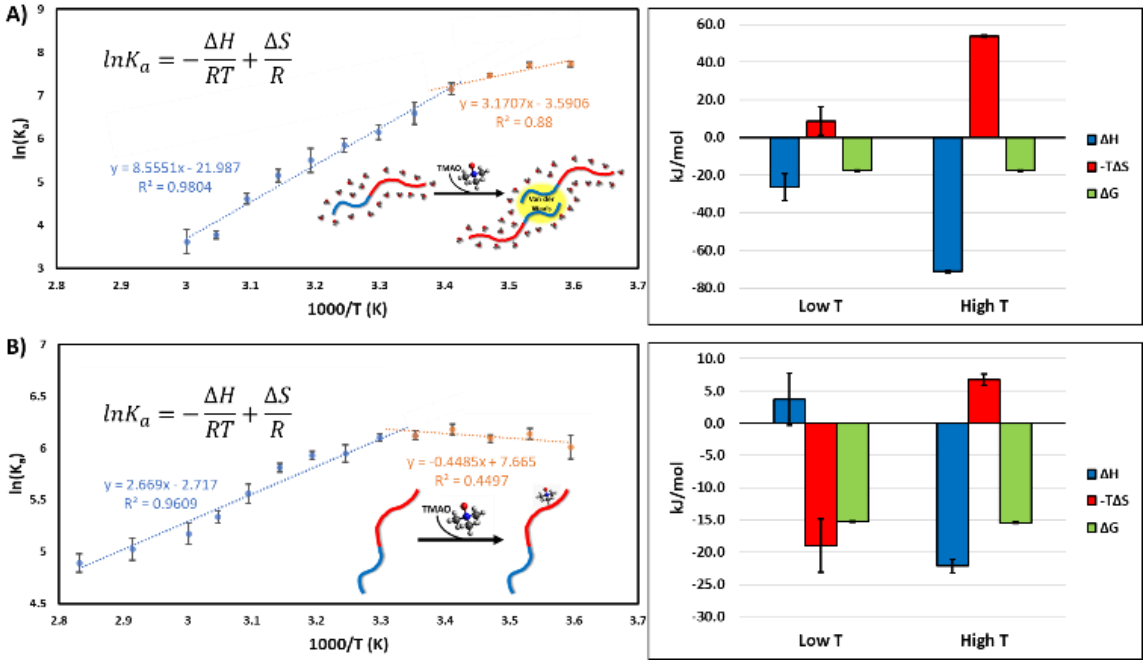

Figure 2.4 (A) Van't Hoff plots for the self-assembly reaction of SP (5 µM) and 500 µM TMAO (500 µM) in water, and SP-TMAO adduct of TMAO (B). These data were collected on a Synapt-G2 TWIMS instrument. In both (A) and (B) the low temperature data are shown in orange and higher temperature data are shown in blue. The thermodynamic contributions of ΔH, -TΔS, and ΔG are shown for each (A) and (B). Values were calculated at T = 293 K for (A) and T = 298 K for (B). Note that y-axes are not matched to scale.

and -TΔS) of 3.7 kJ/mol and -19.0 kJ/mol (298 K) for the low temperature and -22.2 kJ/mol and 6.5 kJ/mol (298 K) at higher temperature (**Table 2.1**).

Table 2.1 Thermodynamic values for SP dimer formation and TMAO Adduct formation

		ΔH	-TΔS	ΔG	Notes
Dimer Formation	Low T	-26.4	8.8	-17.6	T = 293 K
	High T	-71.1	53.6	-17.5	T = 293 K
TMAO Adduct Formation	Low T	3.7	-19.0	-15.3	T = 298 K
	High T	-22.2	6.7	-15.5	T = 298 K

Van't Hoff plots for SP dimer formation are similar, albeit less pronounced than that of $[SP\text{-}TMAO]^{2+}$. The inflection temperature for formation of SP dimers occurs at ~293 K, and the relative abundances of dimers exhibit minor changes at solution temperatures between 278 K and 293 K. At T > 293 K the slope change in the Van't Hoff plot is quite steep. The behavior at cold temperatures is consistent with a smaller entropic barrier for self-assembly than that at high temperature, consistent with the small entropic penalty associated with decreased ordering of the hydrating water molecules. At higher temperatures, the interactions between SP and TMAO are less favorable, as evidenced by the rapid decrease in the abundances of the $[SP\text{-}TMAO]^{2+}$ complex, expected behavior for a reaction that is driven by the favorable enthalpy. The enthalpic contribution becomes dominant due to the decrease in the prevalence of hydration water in the vicinity of the hydrophobic residues, thus the SP dimer involves Van der Waals interactions without the intercalation of water interrupting the binding region.

Formation of $[SP\text{-}TMAO]^{2+}$ ions at low temperatures is consistent with limited interaction between the SP hydrophobic C-terminus and the hydrophobic methyl groups of TMAO that promotes displacement of hydrating water molecules, consistent with favorable entropy originating from reorganization of the hydration shell and excluded volume effects.[179] However, at solution temperatures greater than 298 K the formation of the $[SP\text{-}TMAO]^{2+}$ complex becomes enthalpically favored. Both mechanisms are consistent with the changes observed for $-T\Delta S$ at low and high temperature (Figure 4B). It is also interesting to note that the abrupt change in thermodynamic signature for the formation of $[SP\text{-}TMAO]^{2+}$ may indicate a change in binding preference for the TMAO molecule, *i.e.*, switching from limited hydrophobic binding at cold temperature to predominantly H-binding at warmer temperatures. TMAO is readily excluded from protein surfaces, as it tends to form more favorable H-bonds with the solvent.[131, 189, 190] While the location of the TMAO adduction site(s) cannot be deduced directly from the MS data, previous MD simulations for SP confined in nanodroplets containing H_3O^+ and Cl^- anions showed clear evidence for interactions of Cl^- and H_3O^+ with the charge carrying N-terminus, *e.g.*, amino acid side chains (H_3N^+-RPKPQQ-);[185] however, the experimental data suggests that Cl^- and H_3O^+ ions are also evidence suggest weak interactions of TMAO with hydrophilic side chains of peptides/proteins are also weak.

These studies provide insight into the mechanisms for TMAO stabilization of protein structure. Our initial observation of the $[2SP + 4H]^{4+}$ dimer using cryo-IM-MS provided the impetus for follow-up experiments targeted at procuring thermodynamic data for the TMAO/SP interaction and the formation of the SP^{2+} dimer. Thermodynamic data

for the TMAO/SP interaction show that TMAO utilizes entropic favorability to interact with the SP molecule at cold temperatures—a process involving reorganization of hydrating water from the peptide backbone to the bulk solution, thereby inducing a solvent excluded volume effect that preferentially favors hydrophobic interactions (*i.e.*, an indirect mechanism). The entropic favorability of the TMAO/SP interaction coincides with a lowering of the entropic barrier for self-assembly.

Lower solution temperatures decreases the prevalence of the hydrophobic effect.[90, 91, 103] However in the presence of TMAO the self-assembly of SP—involving hydrophobic-hydrophobic interactions[191]—is favored at low temperatures. Hydration of hydrophobic molecules is generally disfavored under ambient conditions owing to entropic penalty as the hydrating water becomes more ordered. Reorganizing the water molecules around the hydrophobic regions of the molecule is entropically favored at lower solution temperatures.[90, 91, 103, 192, 193] A study by Shea and co-workers has demonstrated that small increases in solution temperature (20 K) are sufficient to remove waters from hydrophobic regions of biomolecules.[194] This result provides an explanation as to why there is a mechanistic change in the thermodynamics data for the dimer formation of SP. As the solution temperature increases the solvated state of the hydrophobic region of the SP molecule transitions from a "wet" to a "dry" state.[195] At cold solution temperatures TMAO can make dimer formation of SP more entropically favorable via removal of hydration waters, however at higher solution temperatures hydrophobic side chains would become more "dry." This effect would lead to TMAO being less effective at retaining $[2SP + 2H]^{2+}$ ions through removal of waters. This

interpretation agrees with the vT-IM-MS data in which loss in the abundance of $[2SP + 2H]^{2+}$ ions as a function of solution temperature is markedly increased for temperatures above 293 K.

2.4. Experimental Information

All vT-ESI experiments were conducted on a Waters Synapt-G2 TWIMS-ToF. The concentration of SP was maintained at 5 μM while the TMAO concentration was varied; typical SP to TMAO ratios of 50:1, 5:1, 1:1, 1:10, 1:100. The vT-ESI source has been described in more detail previously.

Thermodynamic measurements for the formation of the $[2SP + 2H]^{2+}$ dimer and $[SP + TMAO]^{2+}$ complex were calculated using the relative abundance the precursors and product ions as determined from the IM-MS spectra.[12, 13, 196] of the SP dimer over the total abundance of SP monomer in the ion mobility spectrum. The equilibrium constants for the TMAO/SP interaction were calculated in a similar manner. Plots of the $ln(K_a)$ of the equilibrium constants vs the inverse of the solution temperature yields the Van't Hoff relationship, from which the ΔG, ΔH and -TΔS values were calculated. The thermodynamic study was conducted in triplicate and all error bars are representative of the standard deviation of the measurements.

Substance P was obtained from Sigma Aldrich at a purity of 95%. The TMAO used in this study was obtained from Cayman Chemical at a purity of 95%. The urea used in this study was purchased from EM Science at a purity of 99%. Unless otherwise noted

all solutions used in this work were prepared in 18.2 MΩ water at pH ~7. Move this type of info to SI...label an exp section.

We previously described methodologies for using vT-ESI-MS experiments to measure the thermodynamics of the using vT-ESI-MS.[8, 197]

2.4.1. Explanation of methods employed for thermodynamics quantitation.

Van't Hoff plots yield thermodynamic information by plotting the natural log of the equilibrium constant (association constant) of the reaction against the inverse of the temperature in Kelvin. When the points are fitted linearly the equation of the line is in the form of **Equation 2-1**.

Equation 2-1

$$K_{eq} = -\frac{\Delta H}{RT} + \frac{\Delta S}{R}$$

The equilibrium constants used in to form the Van't Hoff plots were the association constants (K_a). The calculation of the K_a values for the dimer formation utilized **Equation 2-2**.

Equation 2-2

$$K_a = \frac{I_{dimer}}{[I_{monomer}]^2}$$

Where I_{dimer} is the intensity of the dimer in the mobility spectrum and $I_{monomer}$ is the intensity of SP monomer in the mobility spectrum. The monomer value is squared because the "free ligand" concentration that would typically be a variable in the equation is the SP monomer itself.

Equation 2-3 was used to calculate the K_a values for the SP and TMAO interaction:

Equation 2-3

$$K_a = \frac{I_{SP+TMAO}}{I_{SP} \cdot [TMAO]}$$

Where $I_{SP+TMAO}$ is the mass spectral intensity of $[SP + TMAO]^{2+}$, I_{SP} is the mass spectral intensity of the SP monomer ions, and $[TMAO]$ is the concentration of TMAO in the sample.

2.5. Conclusions

The low concentrations of analytes used in this study also draw attention to the unique solution environment of ESI droplets.[198, 199] Typically, in solution-phase studies, the osmolyte concentration used is in the molar range,[139, 161, 162, 164, 190, 200-202] yet in the MS experiments, micromolar range of osmolytes were used to induce observable products of osmolyte interaction. Circular dichroism (CD) studies performed by Rueger et al. show that SP can spontaneously form oligomers in solution via hydrophobic interactions in the low mM range of concentration,[191] but the results from cryo-IM-MS and ambient TWIMS-MS experiments show that TMAO enhances oligomer formation in the μM range through an indirect mechanism rather than a direct interaction. Evidence for an indirect mechanism is the exclusion/absence of TMAO molecules adducted to the dimer complex in the cryo-IM-MS experiment. Experimental data and MD simulations have predicted that protein surfaces exclude TMAO,[128, 136, 164, 203] which may explain why TMAO is not adducted to the $[2SP + 4H]^{4+}$ ions in **Figure 2.1C**

and is only weekly adducted to $[SP + 2H]^{2+}$ (Figure S2). The formation of solvent excluded volumes favors hydrophobic contacts between hydrophobic regions of SP ions in solution leading to the formation of a dimer species.[204, 205] The formation of a dimer species would be more entropically favorable exclusion of water in the presence of TMAO that accompany decreased numbers of hydrating water molecules necessary to form solvation shells for the SP ions.[128, 206]

Further studies should be directed at understanding roles the nanodroplet environment enacts in osmolyte-biomolecule interactions. Moreover, the inclusion of experimental data as a compliment to MD simulations is important to elucidate the true mechanisms of osmolyte interactions.[131] The vT-ESI-MS studies reported here provide a new level of specificity which is difficult to achieve in conventional solution-phase experiments.

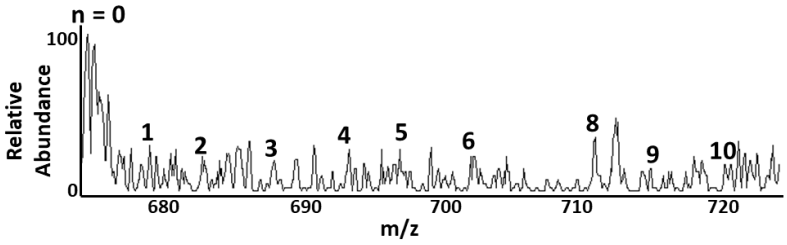

Figure 2.5 Mass spectrum displaying the n<10 water clusters of the $[2SP + 4H]^{4+}$ dimer; each water cluster is spaced by 4.5 *m/z*.

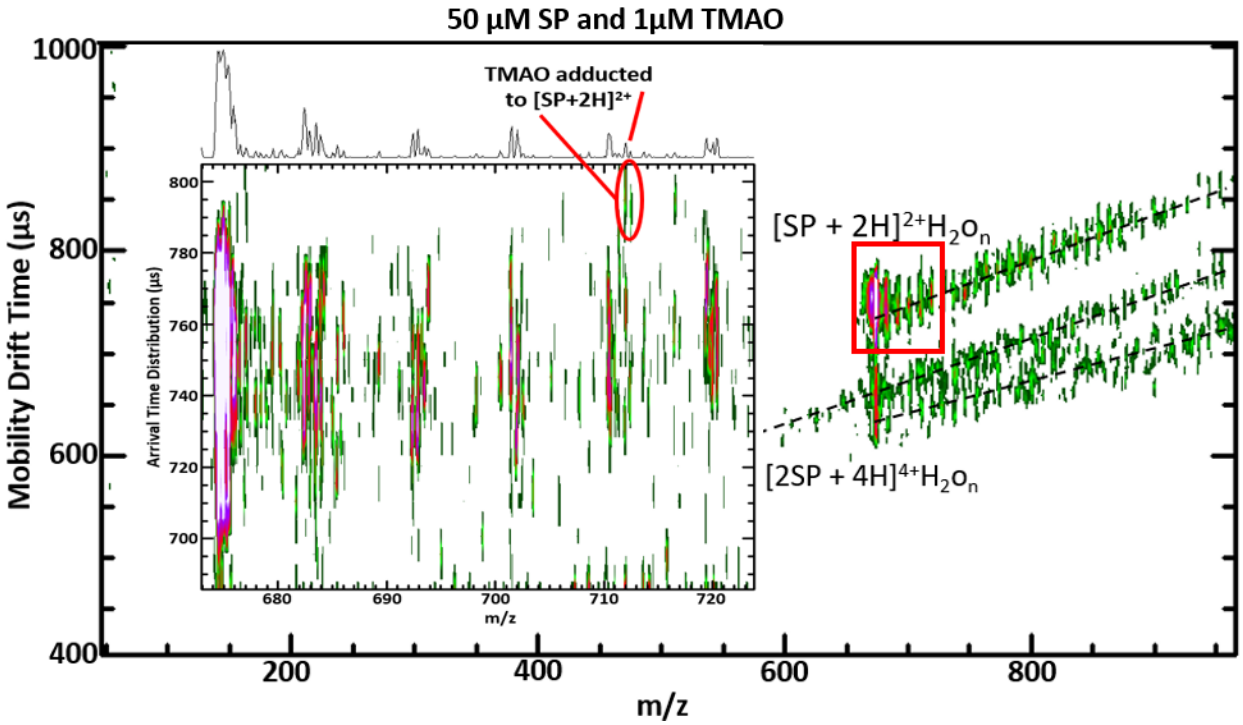

Figure 2.6 50 µM SP and 1 µM TMAO in water. The inlay shows a zoomed in version of Figure 1B. the TMAO molecule is shown to be bound to the $[SP + 2H]^{2+}$ ion. This species does not show any further hydration unlike the unbound $[SP + 2H]^{2+}$ which shows extensive hydration. This effect may be due to the TMAO making water adduction unstable during the ESI process.

3. SURFACE ACTIVITY OF AMINES PROVIDES EVIDENCE FOR COMBINED ESI MECHANISM OF CHARGE REDUCTION FOR PROTEIN COMPLEXES*

3.1. Abstract

Charge reduction reactions are important for native mass spectrometry (nMS) because lower charge states help retain native-like conformations and preserve non-covalent interactions of protein complexes. While mechanisms of charge reduction reactions are not well understood, they are generally achieved through addition of small molecules, such as polyamines, to traditional nMS buffers. Here, we present new evidence that surface active, charge reducing reagents carry away excess charge from the droplet after being emitted due to coulombic repulsion, thereby reducing the overall charge of the droplet. Furthermore, these processes are directly linked to two mechanisms for electrospray ionization, specifically the charge residue and ion evaporation models (CRM and IEM). Selected protein complexes were analyzed in solutions containing ammonium acetate and selected trialkylamines or diaminoalkanes of increasing alkyl chain lengths. Results show that amines with higher surface activity have increased propensities for promoting charge reduction of the protein ions. The electrospray ionization (ESI) emitter potential was also found to be a major contributing parameter for the prevalence of charge reduction; higher emitter potentials consistently coincided with lower average charge states among all protein complexes analyzed. These results offer experimental evidence

*Reprinted with permission from Walker, T. E.; Laganowsky, A.; Russell, D. H. Surface Activity of Amines Provides Evidence for the Combined ESI Mechanism of Charge Reduction for Protein Complexes. Anal Chem 2022. DOI: 10.1021/acs.analchem.2c01814.

for the mechanism of charge reduction in ESI, and also provide insight into the final stages of the ESI and their impact on biological ions.

3.2. Background

Electrospray ionization of biomolecules has gone through many stages of development since it was first described by Fenn and coworkers some 35 years ago.[29, 207, 208] But Fenn's vision of the long term impact, expressed in the 1990 review of electrospray ionization "*...that other "cooks"(practitioners) will have even more success than we have had with the recipes to be presented*..." (Fenn et al., page 38)[17] rings true even today! Researchers continue to develop new approaches that improve the informational content of the ESI mass spectral data. Notable examples include super-charging reagents that have played key roles in the development of top-down protein sequencing[39, 209, 210] and more recently, the introduction of native mass spectrometry (nMS) buffers that are volatile and reduce salt adduction[34, 211, 212] and the use of sub-micron emitters that provide cleaner, more defined mass spectral peaks and better signal-to-noise ratios (S/N).[45, 47, 213-216] While ammonium acetate is an excellent buffer for native MS, other buffer systems are often used to either increase or reduce the charge state distribution of proteins.

Charge reducing reagents are MS-friendly buffers that lower the average charge state (Z_{avg}) of protein ions.[31, 217] Lower charge states appear at higher *m/z* therefore increasing the charge state spacing (resolving power) for ions of proteins and protein complexes. The increased *m/z* separation has proved particularly advantageous for studies

of lipid binding to membrane protein complexes[188] and more generally for preserving intact protein complex structures.[218, 219] Lower Z_{avg} is also correlated with more native-like protein states due to less coulombic repulsion throughout the protein structure.[220-222] The most commonly used nMS buffers are ammonium acetate (AmAc), triethylammonium acetate (TEAA), and ethylenediamine diacetate (EDDA) with the latter two being most frequently used as charge reducing buffers.[2, 217] The mechanism of charge reduction and the physicochemical properties that are responsible for observed charge reduction are not well understood. We recently reported results for charge reduction for a series of amino-containing compounds that showed similar charge reduction as TEAA and EDDA, but trimethylamine *N*-oxide (TMAO), showed very different behavior.[188]

The formation of gaseous ions of large molecules from nanodroplets formed by ESI is generally described using the charge residue model (CRM) and ion evaporation model (IEM).[52, 223-227] The CRM purports that macromolecules acquire excess charges from the evaporating nanodroplet during the late stages of desolvation in the transition from solution to gas-phase ions, whereas IEM is often used to explain ionization of small molecules where the ions are ejected from the droplet due to coulombic repulsion near the surface of the droplet;[48, 55, 224, 226, 228, 229] however, neither model accounts for the mechanism of charge reduction in its entirety.

Hybrid models that incorporate both the CRM and IEM processes have been used to explain charge reduction effects observed in ESI formation of ions, most notably, the charge carrier field emission model (CC-FEM).[32, 40, 51, 205, 230, 231] Briefly,

evaporation of the solvent from the initially formed nanodroplets is adequately described by CRM, but as the solvent evaporates the ion density increases and exceeds the Rayleigh limit resulting in droplet fission and ejection of even smaller nanodroplets. As the solvent loss from the nanodroplet leads to increased coulombic repulsion, an IEM step occurs and surface-active ions are preferentially ejected, thus lowering the total charge of the nanodroplet. These processes proceed stepwise until the transition of solvated ions to solvent-free gas phase ions. Thus, the CC-FEM invokes CRM formation of macromolecular ions to be preceded by an IEM step where surface-active ions (less preferentially solvated) are ejected from the droplet. This model provides increased explanatory power for the formation of charge-reduced macromolecular ions. Clearer understanding of electrospray processes allows for tuning of solution conditions to provide for optimal experimental conditions. Many of the factors outlined above for charge reduction are important for elucidating details concerning structure, stability, and dynamics of protein complexes.

Here, we present recent experimental results for large protein complexes that are consistent with the CC-FEM. Monomeric proteins have been extensively studied via ESI-MS, therefore we have chosen to conduct these experiments on protein complexes which offer to provide a more complex and less well-studied response to charge reduction conditions. A recent example reported by Walker *et al.* revealed remarkable effects of native MS buffers, AmAc and EDDA, on the conformation and stabilities of the GroEL tetradecamer.[11] The protein complexes of C-reactive protein (CRP ~115 kDa), pyruvate kinase (PK ~237 kDa) and glutamate dehydrogenase (GDH ~334 kDa (experimental))

were studied using mixed buffers containing various concentrations of AmAc and TEAA, and the effects of nESI (nano-ESI) emitter potentials were also examined. Higher concentrations of TEAA and higher emitter potentials at each TEAA concentration decreased the Z_{avg} for all proteins. We also examined a series of amino-containing compounds (trimethylamine (TMA), triethylamine, tripropylamine (TPA), 1,5-diaminopentane (1,5-DAP), 1,6-diaminohexane (1,6-DAH), 1,7-diaminoheptane (1,7-DAH)). These reagents were used to examine the effects of surface activity of charge carriers on charge reduction. Increasing the hydrophobicity of the amine compound in the mixed buffer solution corresponded to a decrease in the observed Z_{avg} of all the protein complexes.

3.3. Methods

Protein samples of GDH and PK were prepared from lyophilized powders obtained from Sigma. CRP samples were prepared from a 1 mg/mL stock solution obtained from Sigma. All protein solutions were buffer exchanged using BioRad P-6 size exclusion columns with a mass cutoff of 6000 Da to remove unwanted contaminants from the solution. Protein concentrations varied from 750 nM to 2 μM, depending on the protein used. All amine solutions were used in the presence of 160 mM ammonium acetate (AmAc). All amines were obtained from Sigma. The pH of the AmAc, TMA, TEAA, TPA solutions were pH 6.5 to pH 7. TMA and TPA solutions were acidified slightly using acetic acid to reach pH 6.5. Solutions of the diaminoalkanes 1,5-DAP, 1,6-DAH, and 1,7-

DAH were acidified to pH 8 (from pH 9.5 initially) using acetic acid. All pH measurements used 3-color litmus paper purchased from J.T. Baker.

All solutions were sprayed using pulled borosilicate capillaries with an emitter diameter of 1-2 μm. The same tip-pulling program was used across all experiments to mitigate tip diameter effects as much as reasonably possible. Mass spectra were deconvoluted using UniDec processing software.[232] Relative abundances of the charge states were used to calculate a weighted average charge. All experiments were conducted on the Thermo Q Exactive UHMR (ultra-high mass range) instrument. Mass resolution was set to either 6250 or 12500 for all experiments shown here. Instrument tuning conditions used to promote desolvation of ions were maintained at identical levels for each protein complex to provide an accurate comparison of charge reduction that are solely dependent on solution conditions. Spray voltage was also tuned to achieve highest signal except in the experiments where spray voltage was used as the variable in the experiment. Spray voltage is defined as the absolute voltage measured on the emitter referenced to ground. Heated capillary temperatures were maintained at 200 °C.

Triplicate collisional-cross section (CCS) measurements for CRP were made using mixed buffer solutions with varying ratios of AmAc and TEAA; 200 mM AmAc or 160 mM AmAc with 0, 5, 10, or 15 mM TEAA. The emitter potentials were tuned to get optimal signal and then biased by ~+200 V and ~+400 V relative to initial voltage to explore the CSD sampled at higher emitter voltages. Ion mobility experiments were conducted using the Fourier transform periodic-focusing ion-mobility drift tub (FT-PF-IM-DT) UHMR Orbitrap instrument. All experiments were performed using helium

collision gas at 1.725 torr, at 23.7 °C. A more detailed description of the fundamental theory and workings of the instrument has been described thoroughly in previous papers.[62, 70, 233, 234]

3.4. Results

To explore the effects of charge reduction on protein complexes, various mixtures of TEAA and AmAc were screened against 3 protein complexes (CRP, PK, and GDH). The observations from this study led to the conclusion that as the concentration of TEAA was increased, the Z_{avg} of the observed charge state distribution was lowered. This trend reached asymptotal behavior beginning at 20 mM TEAA. **Figure 3.1A** summarizes the average charge state of 3 protein complexes (CRP, PK, and GDH) in response to different concentrations of TEAA.

Emitter voltages can vary based on various solution factors and can be used to control the ionization efficiency. For certain buffer conditions, increased nESI emitter voltage caused a shift to a lower charge state for proteins in mixed buffer conditions. The mass spectra clearly show a large change in charge state distribution (CSD) in response to an increase in the emitter potential of about +400 V from the initial nESI potential (see **Figure 3.6**). **Figure 3.1A** reveals two different trends for the Z_{avg} for each protein complex studied: 1) an increase in emitter potential lowers the Z_{avg} of the ions for a given set of buffer conditions; 2) as TEAA concentration is increased the emitter potential needed to lower the Z_{avg} of the ions decreases. The plots in **Figures 3.1B** and **3.1C** show both trends; **Figure 3.1B** shows the observed change in relative abundance for the low and high CSDs

as a function of emitter voltage while **3.1C** shows the change in CSD as a function of TEAA concentration. The AmAc concentration was maintained at 160 mM regardless of

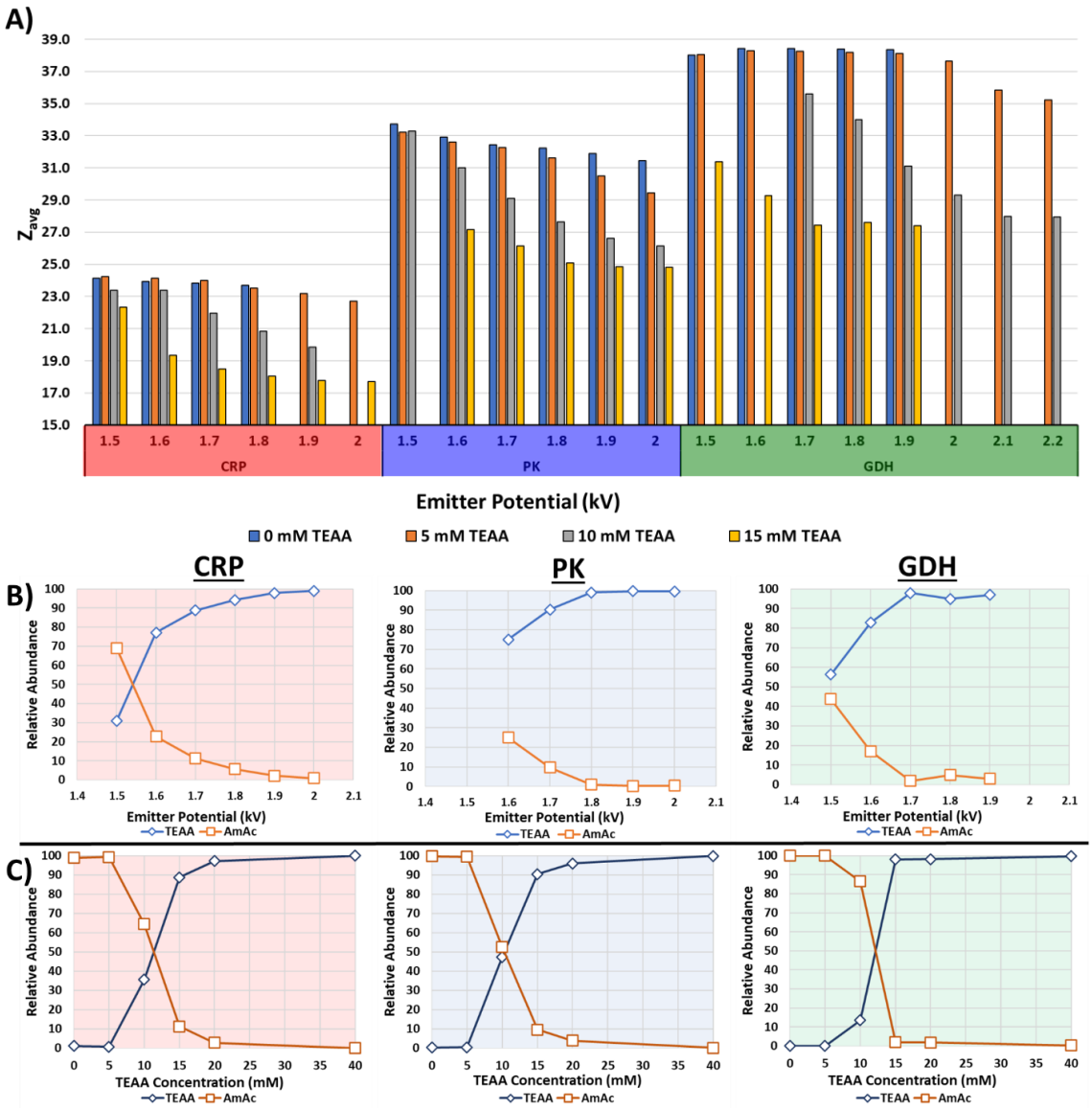

Figure 3.1 A) Bar charts displaying the average charge state of CRP, PK, and GDH protein complexes as a function of TEAA concentration and emitter voltage. The Z_{avg} shifts by up as much as 25% simply by increasing spray voltage. AmAc concentrations are held constant at 160 mM for all data in this figure. B) Plots showing the relative abundances of the low (TEAA-like) and high (AmAc-like) CSDs for 15 mM TEAA and 160 mM AmAc buffer conditions as a function of emitter potential. C) These plots show the same information as (B) but as a function of TEAA concentration at 1.7 kV emitter potential.

the TEAA concentration. This was intended to keep a fixed concentration of AmAc in the solution even though that as the concentration of TEAA was varied the ionic strength of the solution would be altered as well. The concentration of AmAc did not have a

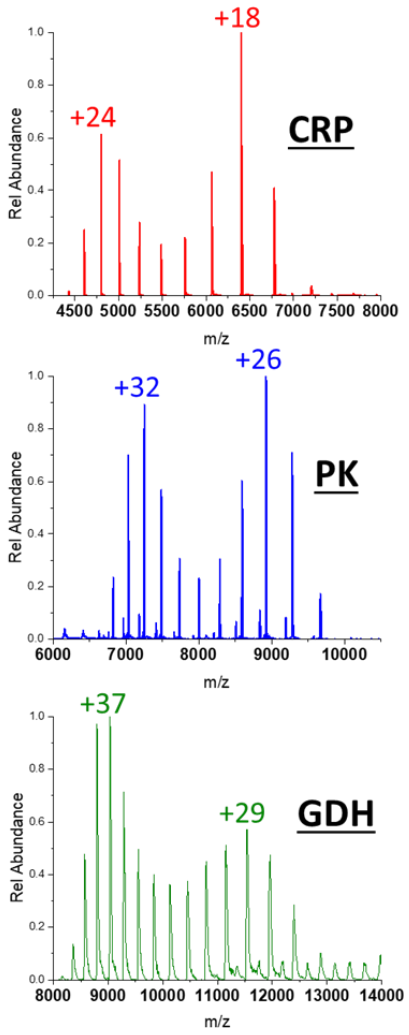

Figure 3.2 Mass spectra of CRP, PK, and GDH demonstrating the bimodal charge state distribution that accompanies a combined ionization model. The higher charge state distributions are typical for AmAc buffers, whereas the lower charge state distributions are typical for TEAA charge reduction. The buffer concentrations are 10 mM TEAA and 160 mM AmAc.

significant effect in subsequent trials (data not shown) and reaffirmed the observation that TEAA concentration was responsible for charge reduction.

The mass spectra of CRP, PK, and GDH in 10 mM TEAA and 160 mM AmAc (**Figure 3.2**) show bimodal CSDs; these bimodal distributions are due to the presence of two different ion populations and suggest that there are two ionization mechanisms operating to generate each ion population. The higher Z_{avg} distribution is similar to that seen when sprayed from an AmAc solution whereas the lower Z_{avg} distribution is similar to results seen in a mixed buffer solution containing higher concentrations of TEAA (*e.g.*, > 20 mM TEA, see **Figure 3.1** and **Figure 3.7**). This bimodal CSD behavior dissipates at higher concentrations of TEAA in the solution and at higher nESI emitter potentials. The distributions are sensitive to emitter potentials and can be shifted reversibly to higher or lower charge states by changing the bias placed on the nESI emitter (**Figure 3.8**). At 20 mM TEAA, the ion populations of these protein complexes are nearly entirely charge-reduced. This observation implies that a critical concentration of TEAA in the droplet is necessary to effectively charge reduce the ions, and that there exists a small concentration window to observe the shift in Z_{avg} from non-charge-reduced to charge-reduced distributions. The emitter potential effects suggest that higher spray voltages increase the partitioning of surface-active charge carries between the bulk and the surface of the nanodroplet. This would explain why lower Z_{avg} are observed at higher emitter potentials without increasing the bulk concentration of charge reducing reagents in the solution.

Trialkylamines and diaminoalkanes were added to AmAc solutions to explore the effect of surface activity on the efficacy of charge reduction. The final concentrations for

these solutions consisted of 40 mM of selected amine and 160 mM of ammonium acetate. **Figure 3.3A** contains the high *m/z* range of mass spectra obtained using solution with and without added charge reducing buffers. TMA, TEAA, and TPA show increased ability to reduce the Z_{avg} for both GDH and CRP concomitantly with the increasing lengths of the alkane chains. Similar data (**Figure 3.3B**) were obtained using 1,7-DAH solution, which is even more effective for lowering the Z_{avg} of the CRP ions than the 1,6-DAH and 1,5-

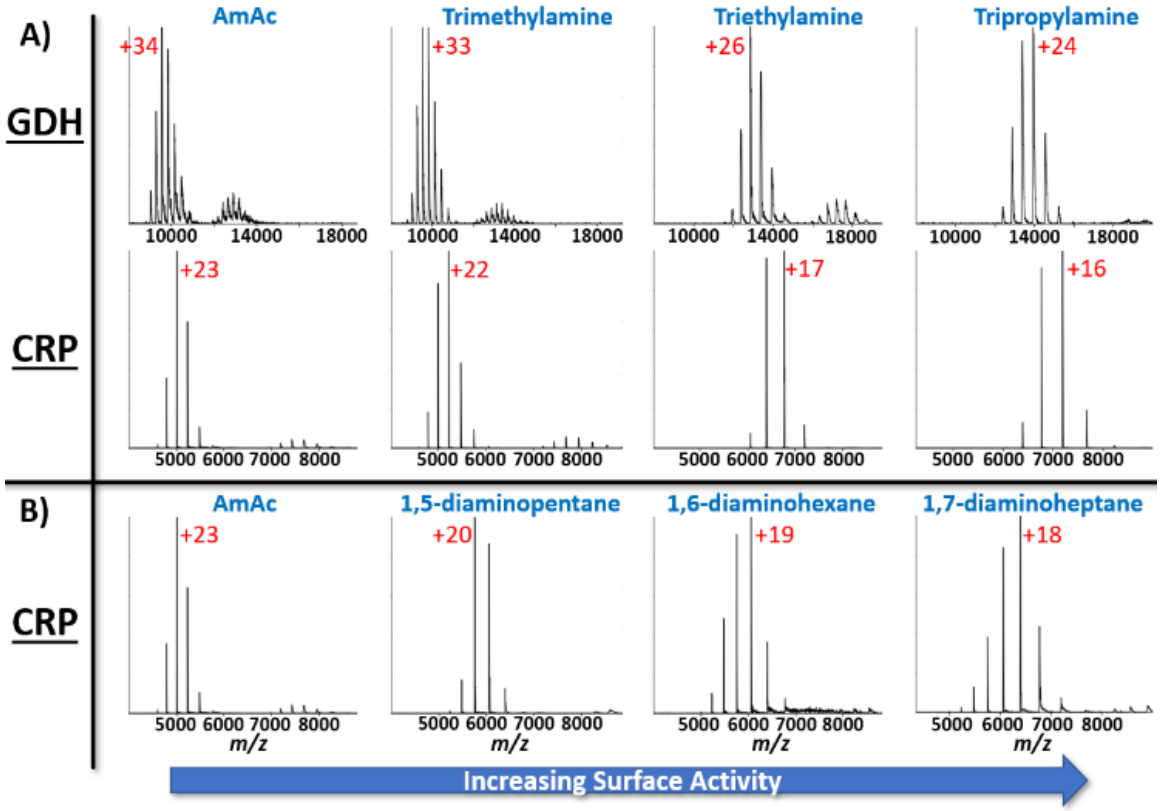

Figure 3.3 Mass spectra demonstrating the efficacy of amines and dialkylamines to reduce the Z_{avg} of given proteins. A) GDH and CRP protein solutions had 40 mM of a given amine added to the solution. For both protein complexes a trend of lower Z_{avg} exists as the surface activity of the amine increases. B) CRP mass spectra in a similar experiment using dialkylamines to show a trend of increasing charge reduction as the surface activity of the dialkylamine increases. Once again, the most surface-active charge carrier is the most effective charge reduction agent. Labeled charge state are the charge state of the peak with the highest relative abundance.

DAP solutions. Increasing the length of the alkane chains increases the hydrophobicity and in turn the surface activity of these charge carriers thus decreasing the favorability of being solvated in the "bulk" solution of the droplet. This is also demonstrated when comparing the exhibited charge reduction of the alkyl diammonium series and the trialkylammonium series for CRP. The trialkylammonium ions are more effective at reducing the Z_{avg} of CRP because they are more hydrophobic than the alklyl diammonium ions. The emission of these molecules from the droplet is responsible for the lower Z_{avg} of the resulting macromolecular ions exhibited in **Figure 3.3**.

3.5. Discussion

Surface-activity is a term used here to describe how likely hydrophobic charge carriers, *e.g.,* alkylamines, are to be partitioned to the surface of the nanodroplet. The initial understanding of how charge is distributed in charged nanodroplets is attributed to Gauss' law which predicts that charges are located at the surface of the droplet due to coulombic repulsion. Simulations conducted by Konermann *et al.* demonstrated that small charge carriers (Na^+, K^+, NH_4^+) are preferentially solvated and that their existence at the surface of the droplet would bear an enthalpic penalty.[50, 224, 235] On the other hand, larger hydrophobic charge carriers that are less preferentially solvated would be partitioned to the surface of the droplet more than smaller ions. Hogan *et al.* describe a process by which surface active ions are ejected from the droplet before CRM formation of the macromolecular ion.[51] These surface active ions are preferentially ejected from the droplet leading to lower charge states for the respective macromolecules. With more

surface-active charge carriers being emitted from the droplet, fewer charges are then available to reside on the macromolecule. The CC-FEM, in essence, is the mechanism underlying the charge reduction of protein ions generated from nESI. **Figure 3.4** presents the CC-FEM mechanism (**3.4A**) along with the CRM (**3.4B**) for comparison. Bush *et al.* concluded that a CC-FEM model is also applicable to negative mode electrosprays inclusively.[236] They showed that negative charge carriers can more easily be emitted from the droplet than positive charge carriers, resulting in lower overall charge for negative ions. A possible aside to the CC-FEM is the effect that droplet surface tension may have on the final charge state of gas-phase ions. Donald *et al.* observed trends in supercharging effects on proteins (i.e., increased Z_{avg}) while using cyclic alkyl carbonates

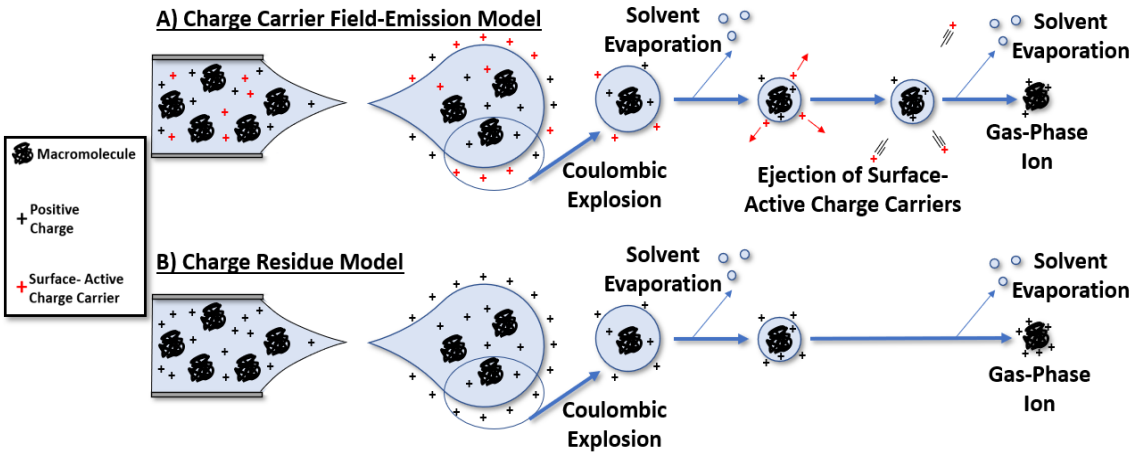

Figure 3.4 A) A representative sketch of the basic mechanism for combined CRM and IEM. Surface active charge carriers disproportionally populate the surface of the parent droplet. Progeny droplets then are given large relative concentrations of surface-active charge carriers. These charge carriers leave the droplet and syphon excess charges from the droplet. The proteins left in the nanodroplet are then ionized via a CRM pathway. B) The CRM is generally accepted as the mechanism for the formation of macromolecular ions from ESI droplets. The charge carriers in this model are more likely to stay solvated in solution and thus their charge will become deposited upon loss of the solvent.

and cyclic alkyl sulphites, with various alkyl chain lengths, as supercharging reagents.[237]

The data presented in **Figure 3.3** demonstrate the surface activity effect described by the CC-FEM. Protein ions generated from these mixed buffer conditions are more charge-reduced in the presence of buffer components that are more surface active. As an example, TMA is much more easily solvated than TPA; thus, TPA is more surface active and much easier to eject from the nanodroplet. Therefore, the Z_{avg} for proteins in TPA solutions is much lower than that for TMA. This same effect applies to the alkyl diammonium series. The increased length of the alkyl chain increases the surface activity of the molecule and is responsible for the observed charge reduction effects. It is interesting to note the slight differences in the charge reduction effects between the classes of diammonium alkanes. The CSD for CRP in a 40 mM TPA, 160 mM AmAc solution is centered around the 16^+ and 17^+ charge states, whereas the CSD for CRP in a 40 mM 1,7-DAH, 160 mM AmAc solution produces a CSD centered around the 18^+ charge state. 1,7-DAH ions are less surface active than the TPA ions and therefore are not as effective at charge reducing ions. The addition of these amino-containing compounds to the solution did not produce observable signs of protein instability (*i.e.*, dissociation of protein complexes) for the specific conditions used in these experiments (**Figure 3.9**).

Gas-phase basicities of amines are well studied and characterized,[238] and it has been proposed that gas-phase basicities are determinants of protein charge reduction in ESI.[41, 188, 217, 238, 239] While gas-phase basicity may play a role in the mechanism of charge reduction, the observations pertaining to the bimodality of protein ion CSDs do

not support this argument.[51] Gas-phase proton transfer reactions from the protein to an amine would be expected to yield a uniform distribution of charge states that would decrease as the concentration of the gas-phase base increased. While gas-phase proton transfers have been demonstrated to charge reduce ions,[240, 241] it is unlikely that gas-phase proton transfers are responsible for charge reduction via a single ESI emitter owing to the short time scales available in transit to the mass spectrometer and the low densities of ions with which these transfers would be required to occur. Hogan et al. predicted and observed that a bimodal distribution of protein charge state distributions would occur in a mixed buffer environment if charge emission from the droplet was responsible for the observed charge reduction.[51] The initial progeny droplets produced from the mother droplet would be enriched in surface active charge carriers. However, if the overall concentration of charge reduction reagents becomes diminished due to repeated fissioning of the droplet, later progeny droplets produced from that same mother droplet would receive fewer surface-active ions to remove charges from the nanodroplet. This, in turn, would give rise to protein ion populations with bimodal charge state distributions, charge reduced populations from earlier fission events and non-charge reduced populations from late fission events.

Bimodal charge state distributions were also observed for GDH, CRP, and PK in multiple concentrations of TEAA-containing buffers in **Figure 3.2**. The formation of nonspecific dimers for these protein complexes was observed and was initially considered to be the source of these charge reduced ions. However, the breakup of dimer ions does not account for the solution- and voltage-dependance that are observed is these

experiments. The conditions needed to bring about the charge reduction were controlled by varying the nESI emitter potential and the TEAA concentration present in the buffer. As seen in **Figure 3.1**, the Z_{avg} of the protein complexes was sensitive to the concentration of TEAA present in the solution. The emitter potential was also used to increase the relative concentration of TEAA in the droplet. Support for this may be drawn from the observation that higher emitter potentials are linked to larger initial droplet sizes.[242] This may provide increased enrichment of surface active charge carriers in progeny droplets.[34, 243] The need to increase the emitter voltage to effectively lower the charge state distributions of the ions demonstrates that a critical concentration of TEAA is necessary in the droplet to bring about charge reduction of the protein ions.

It is clear from **Figure 3.2** that these conditions show the transitory steps from a non-charge-reduced ion population to a charge-reduced population. These data also exhibit the predicted effects outlined by a field emission mechanism as being responsible for charge reduction rather than it being entirely dependent on gas-phase basicity. Lastly, as the TEAA concentration was increased beyond the limit necessary to begin generating charge-reduced macromolecular ions, the field emission mechanism takes over as the concentration of surface-active ions is sufficient to remove excess charges from the subsequent nanodroplets.

Figure 3.5 shows the change in CCS across the different sets of solution conditions and emitter potentials for each charge state measured. Two observations were made: 1) when compared among conditions for the same charge state, the CCS does not change significantly; 2) the emitter potential, while decreasing the charge state, did not decrease

the CCS when compared to other conditions for that charge state. This would indicate that the observed charge reduction is not a consequence of conformational change induced by the charge reduction reagents.

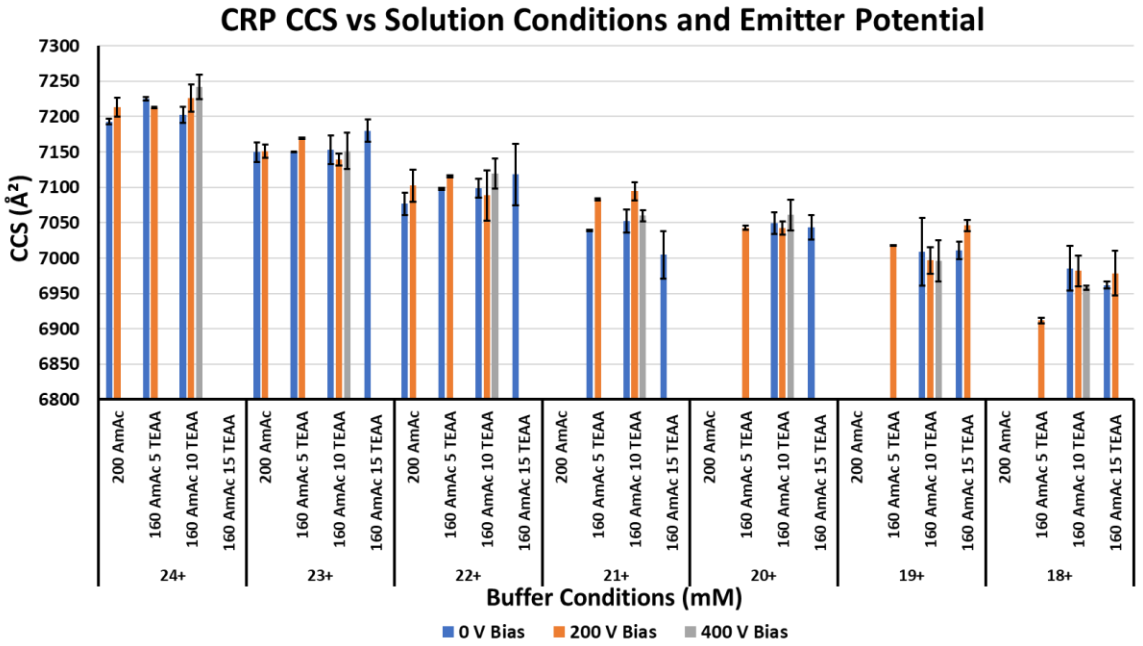

Figure 3.5 Bar chart for the measured CCS of CRP from different charge reducing solutions and nESI emitter potentials. Black error bars delineate the standard deviation of triplicate measurements. Variations in the buffer do not change the CCS significantly when compared among other conditions for the same charge state. Despite lowering the average charge state, higher emitter voltages did not change the CCS values significantly when compared to other values for the same charge state. These results are evidence that the TEAA concentration is not influencing the conformational preference of the protein complex when compared to the same charge state under other buffer conditions.

Charge states of proteins and protein complexes in nMS are closely linked to the solvent-accessible surface area (SASA) of the proteins.[244, 245] It is often appropriate to correlate the charge state of the protein to the conformational state of the protein, i.e., whether the protein has adopted a more native-like or more extended/unfolded state; higher charge states of proteins are indicative of more extended structures.[222] The

question arises, are charge reduction reagents reducing charge states of proteins by altering conformation(s) or are they only perturbing the ESI process? Ion mobility measurements would be able to offer insight into this question. The CCS values shown in **Figure 3.5** clearly show that TEAA concentration does not promote statistically significant changes in CCS for the protein CRP (CCS values and IMS conditions can be found in **Table 3.1**). Even higher emitter voltages, while decreasing the average charge state, do not reduce the CCS when compared to other solution conditions for the same charge state. The lower charge states have lower CCS, which would be explained by a reduction in the coulombic repulsion in the ion. These results support the idea that TEAA reduces average charge states via an ESI mechanism without influencing the conformational preference of the protein ions.

3.6. Conclusion

The results presented here provide additional experimental evidence for the dual ionization model, CC-FEM, for formation of protein complex ions via nESI. This model provides a rationalization for the observed phenomena of charge state reduction in mixed buffer solutions, *viz.* surface activity of the charge-carrying molecules in the nanodroplet definitively predicts the efficacy of the molecule to induce charge reduction of macromolecular ions. Higher emitter potentials are responsible for producing lower charge states of proteins by increasing the partition of surface-active ions in the nanodroplet, forcing surface active ions to the droplet surface. Bimodal charge state distributions for proteins indicate that charge emission of surface-active ions, rather than

a gas-phase proton transfer, is responsible for charge reduction. The observed effects of solution composition and ESI conditions apply also to monomeric proteins. We chose to focus this study on protein complexes due to higher innate charge which illustrates the effect of charge reduction more distinctly.

Protein charge states in native MS are linked to the SASA of the protein. Lower protein charge states favor more native-like conformations in the gas phase due to a reduction in coulombic repulsion.[220-222] It is important to understand how the components in the solution interact with the protein to provide a more accurate framework in which to interpret experimental observations. In these studies, the diaminoalkane molecules were observed to increase the width of the charge state distribution for CRP, which is a potential indicator of conformational drift; however, the CCS for CRP suggest otherwise. These questions illustrate the needs for additional studies on these processes, specifically surface-induced dissociation (SID).[246, 247] Here we do not address potential effects of co-solutes that may also alter the charge states of protein complexes, specifically osmolytes and chaperones. As noted previously for TMAO,[188] these co-solutes are more likely to induce significant compositional and conformational changes. Studies addressing these issues are currently underway.

3.7. Description of the CC-FEM

The Rayleigh limit of charges in a droplet is described as the point at which the repulsion amongst charged species contained within a droplet exceeds the surface tension of the droplet, causing the droplet to undergo a fission event. While droplet fissioning is

an important driving force for ESI, researchers have sought a more specifically defined mechanism for the generation of ions from electrospray droplets. Consta et al. have proposed that charged droplets do not necessarily have to be spherical and that they may actually deform as a way to reduce the repulsive forces that closely packed like-charged ions generate.[248, 249] However, the droplet charge can be considered dynamic, and it is entirely possible that charged droplets will emit hydrated ions,[185] for the purpose of preserving the integrity of the droplet, by pathways other than coulombic explosion. Thompson proposed a theory for generation of ions through what is now referred to as the IEM.[225-227] **Equation 3-1** provides a framework for understanding the generative process of small ions from nanodroplets; n is the charge of the droplet, ε_0 is the permitivity of free space, E^* is critical charge of the droplet surface , e is elemental charge, and D is the diameter of the droplet.

Equation 3-1

$$n = \frac{\pi \varepsilon_0 E^*}{e} D^2$$

E^* essentially governs the rate of IEM-generated ions from nanodroplets and is an innate factor for charge-carrying species in ESI droplets. Hogan et al. proposed that charge carriers with lower E^* thresholds will be emitted from the surface of the droplet more preferentially than ions that have higher E^* thresholds.[51, 231] As the droplet shrinks via solvent evaporation, the density of the charges in the nanodroplet increases; this increase in repulsive forces causes ions on the surface to be emitted from the droplet to reduce the energy needed to keep the droplet shape, as illustrated by Kim et al.[185] Once the necessary critical surface charge is reached, ions on the surface of the droplet are ejected

and the evaporation of the solvent continues until this step is repeated again. This process is considered separate from that of fissioning or coulombic explosion as the IEM process is concerned with the emission of charged species that may or may not be solvated.[224]

Table 3.1 Relevant experimental conditions and values for CCS measurements of CRP; ammonium acetate (AmAc), triethylammonium acetate (TEAA).

Buffer Conditions	Emitter Bias (V)	Mass (kDa)	He Pressure (Torr)	Z (+)	α	PF-DT CCS (nm^2)	Field Strength (V/cm·torr)
200 mM AmAc	0	115.2	1.725	24	0.90	**71.9**	5.71
				23	0.90	**71.5**	5.71
				22	0.90	**70.8**	5.71
				21	0.90		
				20	0.90		
				19	0.90		
				18	0.90		
200 mM AmAc	200	115.2	1.725	24	0.90	**72.1**	5.71
				23	0.90	**71.5**	5.71
				22	0.90	**71.0**	5.71
				21	0.90	**68.8**	5.71
				20	0.90		
				19	0.90		
				18	0.90		
160 mM AmAc **5 mM TEAA**	0	115.2	1.725	24	0.90	**72.2**	5.71
				23	0.90	**71.5**	5.71
				22	0.90	**71.0**	5.71
				21	0.90	**70.4**	5.71
				20	0.90		

				19	0.90		
				18	0.90		
160 mM AmAc 5 mM TEAA	200	115.2	1.725	24	0.90	**72.1**	5.71
				23	0.90	**71.7**	5.71
				22	0.90	**71.2**	5.71
				21	0.90	**70.8**	5.71
				20	0.90	**70.4**	5.71
				19	0.90	**70.2**	5.71
				18	0.90	**69.1**	5.71
160 mM AmAc 10 mM TEAA	0	115.2	1.725	24	0.90	**72.0**	5.71
				23	0.90	**71.5**	5.71
				22	0.90	**71.0**	5.71
				21	0.90	**70.5**	5.71
				20	0.90	**70.5**	5.71
				19	0.90	**70.1**	5.71
				18	0.90	**69.9**	5.71
160 mM AmAc 10 mM TEAA	200	115.2	1.725	24	0.90	**72.3**	5.71
				23	0.90	**71.4**	5.71
				22	0.90	**70.9**	5.71
				21	0.90	**70.9**	5.71
				20	0.90	**70.4**	5.71
				19	0.90	**70.0**	5.71
				18	0.90	**69.8**	5.71
160 mM AmAc 10 mM TEAA	400	115.2	1.725	24	0.90	**72.4**	5.71
				23	0.90	**71.5**	5.71

				22	0.90	**71.2**	5.71
				21	0.90	**70.6**	5.71
				20	0.90	**70.6**	5.71
				19	0.90	**70.0**	5.71
				18	0.90	**69.6**	5.71
160 mM AmAc **15 mM TEAA**	0	115.2	1.725	24	0.90		
				23	0.90	**71.8**	5.71
				22	0.90	**71.2**	5.71
				21	0.90	**70.0**	5.71
				20	0.90	**70.4**	5.71
				19	0.90	**70.1**	5.71
				18	0.90	**69.6**	5.71
160 mM AmAc **15 mM TEAA**	200	115.2	1.725	24	0.90		
				23	0.90		
				22	0.90		
				21	0.90		
				20	0.90		
				19	0.90	**70.5**	5.71
				18	0.90	**69.8**	5.71

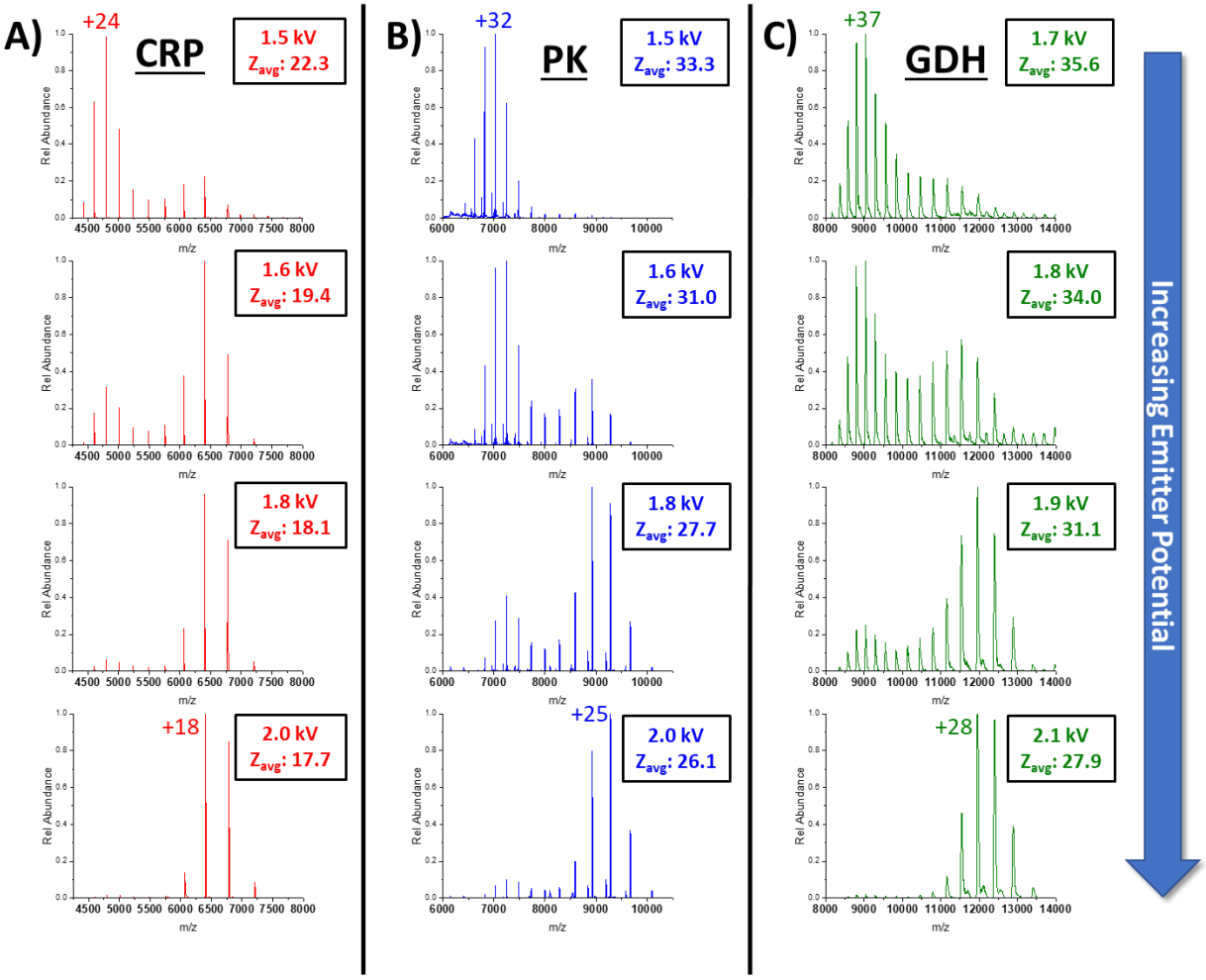

Figure 3.6 Spectra of CRP, PK, and GDH displaying the effect of emitter potential on the observed charge state distributions of these protein complexes. The applied emitter potential (relative to ground) along with the weighted average charge state is displayed with each spectrum. The solution conditions are 750 nM, 2 µM, and 2µM of protein complex (CRP, PK, and GDH, respectively) in 160 mM AmAc and 10 mM TEAA. As the emitter potential is increased, the relative concentration of surface-active charge carriers on the surface of the droplet is increased. Increased concentrations of surface-active charge carriers allow for more charges to be relinquished by the droplet, resulting in lower average charge states.

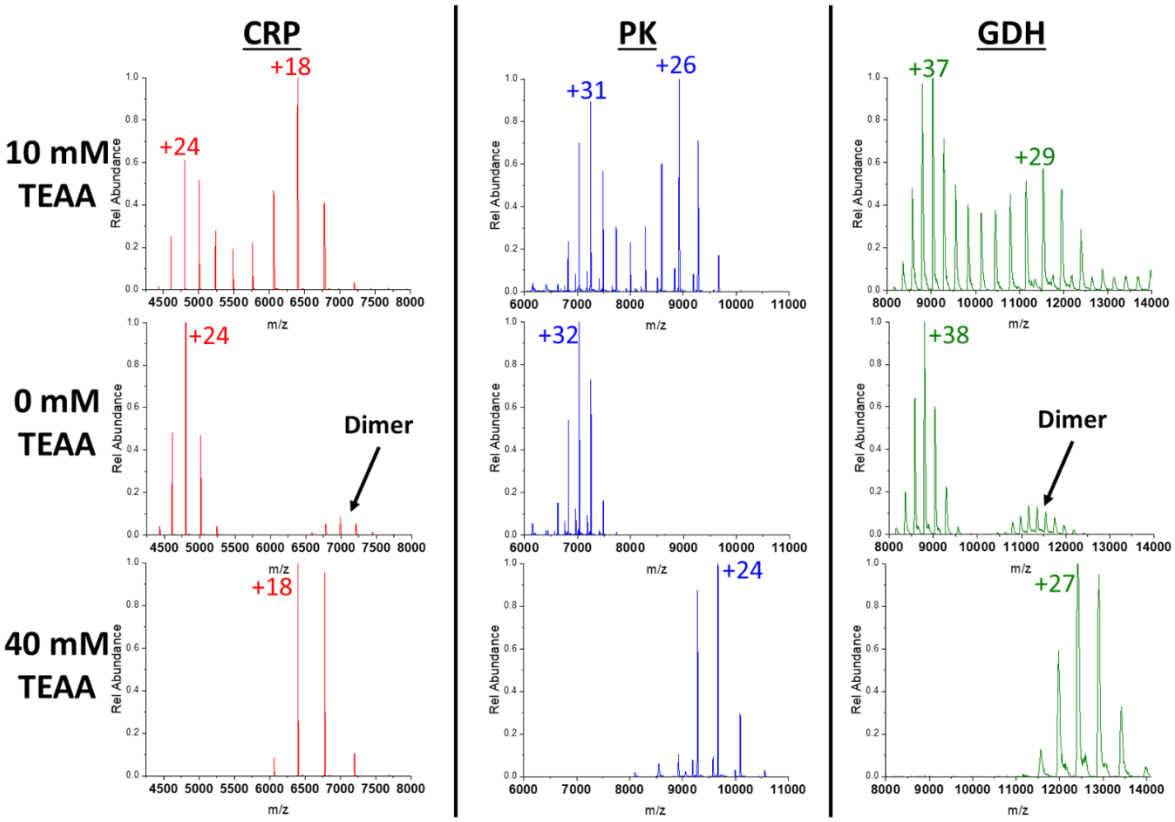

Figure 3.7 Spectra of CRP, PK, and GDH displaying the effect of TEAA concentration on the observed charge state distributions of these protein complexes. In the 10 mM TEAA solution conditions the bimodal distribution of charge states resembles a combination of and AmAc distribution and a 40 mM TEAA distribution (each of which are shown for the requisite protein complex). Dimers of the protein complexes are observed in some of the spectra and are labeled as not to confuse the dimer signals with those of the charge reduced protein complex.

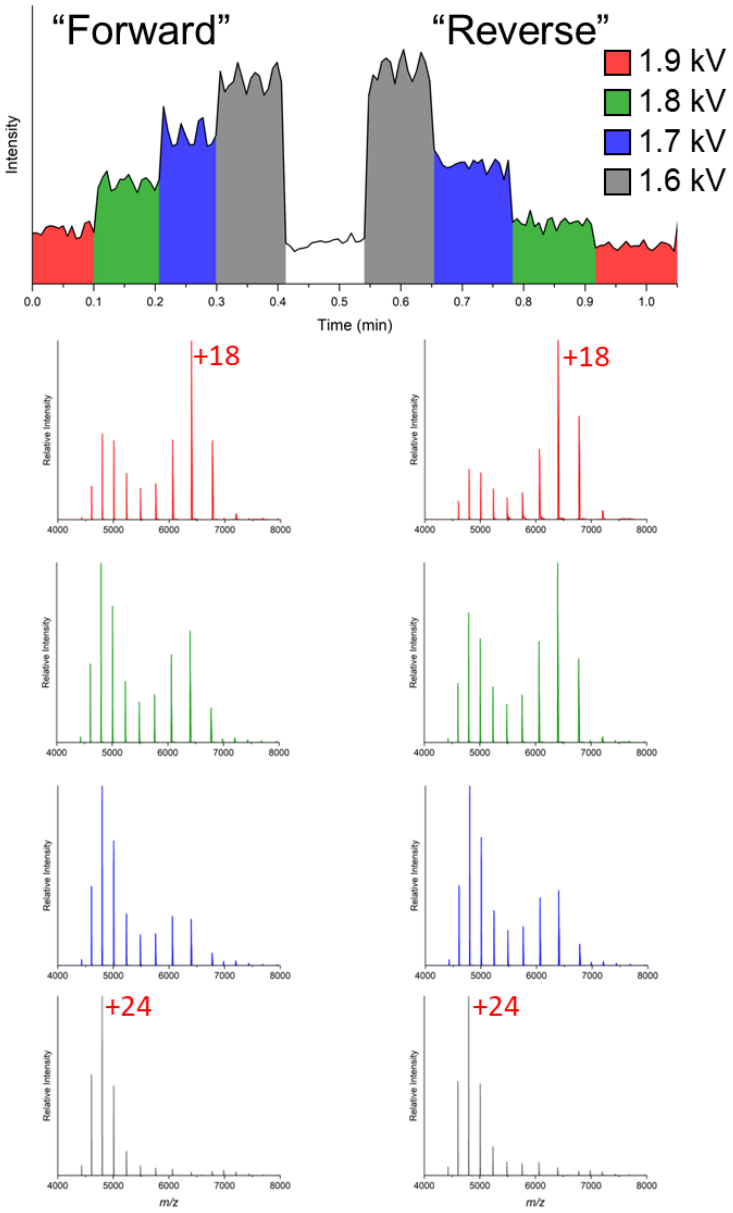

Figure 3.8 Demonstrates the reversibility of the charge reduction phenomenon. The top plot is the total signal intensity as a function of time. The stepwise pattern of the plot corresponds to changes in the emitter voltage applied to the sample. The various time regions are colored and correlate to the spectra represented below. As the voltage is decreased the charge reduction effect becomes less dominant but can be reversed by applying more voltage again. The solution conditions are 750 nM CRP, 10 mM TEAA, and 160 mM AmAc.

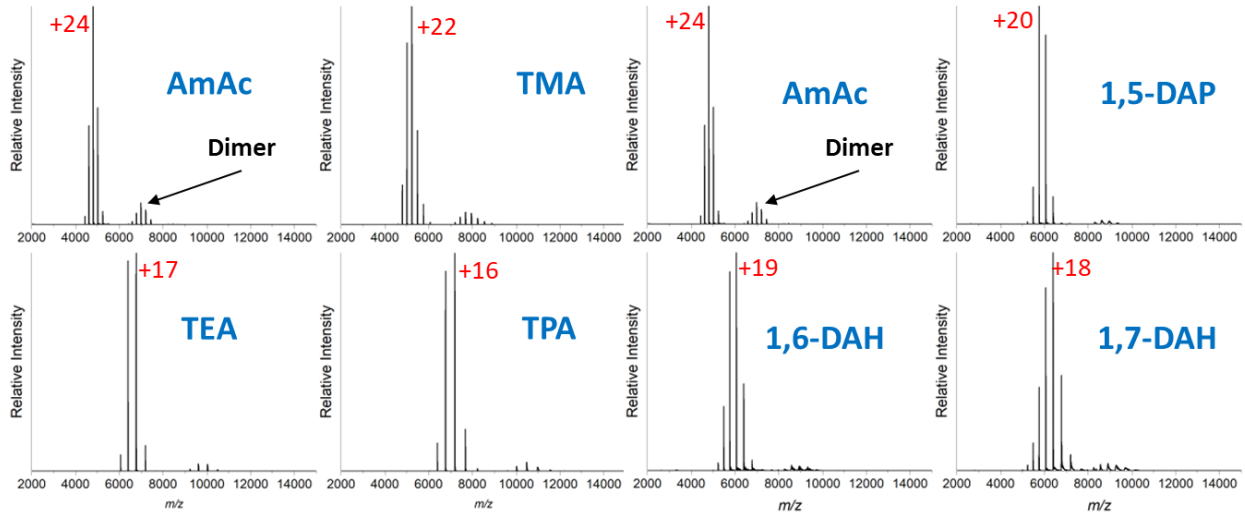

Figure 3.9 Full mass spectral data of CRP for all solution conditions. The lack of observed dissociated monomer (subunits of the native pentamer complex) confirms that CRP remains stable even in the presence of various amines.

4. TEMPERATURE REGULATES STABILITY, LIGAND BINDING (MG^{2+} AND ATP) AND STOICHIOMETRY OF GROEL/GROES COMPLEXES*

4.1. Background

Chaperonins are a class of protein complexes found in all living systems that recognize and bind non-native proteins and assist in the folding of the protein to more stable, native state(s), thereby inhibiting misfolding and aggregation. GroEL, an *E. coli* chaperone, is a model system for understanding molecular chaperones. The GroEL tetradecameric complex ($GroEL_{14}$) is comprised of two heptameric rings stacked back to back.[250] When bound to its co-chaperonin, GroES, a heptameric complex that binds to the apical domain of GroEL, this complex promotes proper folding of the non-native substrate protein. While detailed mechanisms for the assembly of GroEL-GroES complex have been described,[251] largely based on the structural analysis of final products of the processes,[252, 253] many details about the dynamics, stabilities,[254, 255] and assembly of the individual units that comprise the GroEL tetradecamer and the GroEL-GroES complex, are still not fully understood. Most notably, GroEL stability, structure and function(s) are ATP-dependent, the conformational dynamics of GroEL are directly linked to ATP binding and hydrolysis, and specific domains of GroEL subunits, denoted as apical, intermediate and equatorial,[256] are known to exist as three distinct conformations that are linked to specific orientations of the apical domain.[257] The N-

*Reprinted with permission from Walker, T. E.; Shirzadeh, M.; Sun, H. M.; McCabe, J. W.; Roth, A.; Moghadamchargari, Z.; Clemmer, D. E.; Laganowsky, A.; Rye, H.; Russell, D. H. Temperature Regulates Stability, Ligand Binding (Mg(2+) and ATP), and Stoichiometry of GroEL-GroES Complexes. J Am Chem Soc 2022, 144 (6), 2667-2678. DOI: 10.1021/jacs.1c11341.

terminal apical domain of each GroEL subunit is directly involved in binding substrate protein and the GroES co-chaperone. The C-terminal equatorial domains are involved in subunit-subunit interactions both within and between the heptameric GroEL rings as well as binding of nucleotide (ATP), Mg^{2+}, and K^{+} ions.[258] Communication between the apical and equatorial domains is largely achieved by changes in the conformation through a hinge-like motion of the intermediate domain. Collectively, the dynamics of the individual domains within these complexes act as a two-stroke folding machine, wherein, encapsulation of substrate by the one ring, denoted *cis* ring, followed by GroES binding, forming the bullet-shaped (BS) structure, initiates the folding reaction.[253, 259-261] ATP binding drives a structural change and formation of the hydrophilic chamber that triggers protein folding, while ATP hydrolysis acts as a timer, controlling the lifetime of the GroEL-GroES folding chamber.[262] Rye *et al*. proposed that binding of ATP to the *trans* ring, following hydrolysis of ATP in the *cis* ring, triggers disassembly of the GroEL-GroES *cis* ring complex and subsequent release of GroES and the substrate protein into free solution.[262] Yang et al. proposed an alternative model whereby a second GroES binds to the *trans* ring of the $GroEL_{14}$-$GroES_7$ complex to form the symmetric football-shaped (FS) complex, in which ATP hydrolysis and asymmetric nucleotide distributions are essential, but can happen in either ring in an stochastic manner.[263] Potential roles of bullet- and football-shaped GroEL-GroES complexes (BS- and FB-conformations, respectively) remain somewhat controversial.[264, 265] Bigman suggests that BS and FB structures may co-exist and that their relative activities may be linked to ATP concentrations, which have been shown to be widely variable.[266] A more complete

summary of bullet vs. football shaped GroEL-GroES complexes can be found in a recent review by Horovitz et al.[267]

Early mass spectrometry (MS) studies of GroEL/GroES demonstrated the utility of MS for the analysis of large protein complexes[268, 269] and that these measurements are complementary to other structural biology techniques, *e.g.*, electron microscopy, X-ray crystallography, and NMR spectroscopy. MS analyses provide unparalleled sensitivity and dynamic range for studies of conformationally heterogeneous systems, including direct analysis of reaction products formed by interactions with ligands, cofactors, and intermediates formed on pathway from initial reactants to final products.[270, 271] Specific examples that are directly related to GroEL include work by Dyachenko *et al.* where native MS was used to investigate the allostery associated with Mg^{2+}/ATP binding

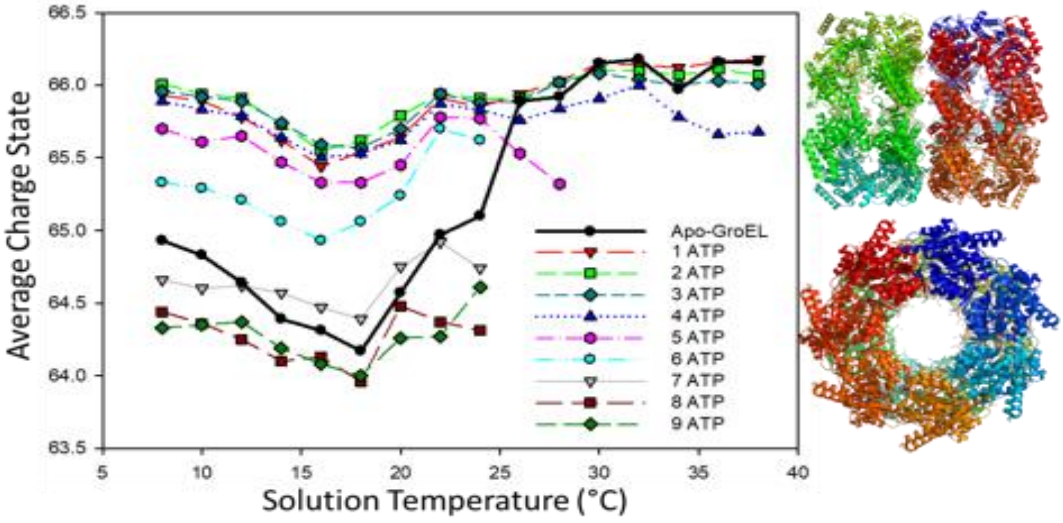

Figure 4.1 Plot showing temperature-dependent changes in average charge (Z_{avg}) of $GroEL_{14}$ and $GroEL_{14}$-ATP_n (n = 1-9). Solution conditions are 1 µM GroEL, 200 mM ammonium acetate, and 125 µM ATP. Note that Z_{avg} for n = 1-4 are similar, but larger changes in Z_{avg} are observed for n = 5 – 9. At T > 24 °C the ion abundances for n = 6 - 9 are below the detection threshold. Also, the abundance of n = 5 is begins to decline at T > 24 °C. This behavior is very different from that obtained using ethylenediammonium diacetate buffer (vide infra).

to GroEL[272] and van Duijin *et al.* who used native MS to study folding and assembly of gp23, the major capsid protein of bacteriophage T4, by the GroEL-gp31 complex (a 912 kDa complex).[273] These studies were performed at different temperatures, 25 and 20 °C and different native MS buffers, ethylenediamonium diacetate (EDDA) and ammonium acetate (AmA), respectively. Dyachenko specifically noted differences for ATP binding and charge state distributions for GroEL using AmA buffers compared to solutions of EDDA.[272] Here, we report data obtained using variable-temperature ESI (vT-ESI) native mass spectrometry that provides additional evidences on the stability and dynamics of the GroEL and GroEL-GroES complex. An earlier report of results from vT-ESI native mass spectrometry were interpreted as evidence for conformational drift associated with ATP binding to GroEL.[274] The vT-ESI-MS experiments report on changes in the protein/protein complex that occur in the solution contained within the ESI emitter vis-à-vis processes that occur prior to the transition from solution to the gas phase. **Figure 4.1** contains a plot of the average charge (Z_{avg}) for $GroEL_{14}$ (solid black trace) and $GroEL_{14}$-ATP_n (n = 1 -9) bound states of the GroEL tetradecamer complex versus temperature of the ESI solution; using these solution conditions complexes with n > 9 are not observed. For the apo-GroEL tetradecamer (solid black trace), Z_{avg} shifts from 64.8 to 64.3 as temperature is increased from 8 to 18 °C, followed by an increase in Z_{avg} to 65.8 between 18 to 26 °C. At temperatures greater than 26 °C, Z_{avg} for $GroEL_{14}$ are centered around 66. Note that Z_{avg} for the $GroEL_{14}$-ATP_n (n = 1-9) products are also temperature-dependent. For n = 1-4, Z_{avg} decreases slightly in the 8 to 18 °C range, but changes for n = 5 and 6 are larger as are the changes for n = 7-9. Note also that Z_{avg} for n = 5 and 6 are

lower relative to those for n = 1-4. At temperatures greater than 18 ^{o}C changes in Z_{avg} are relatively small. The observed changes in Z_{avg} and apparent binding affinities for ATP were attributed to changes in the solvent accessible surface area (SASA) for the apo-GroEL and GroEL-ATP_n complexes owing to temperature- and ATP-dependent conformation changes.[274] The temperature-dependent Z_{avg} for the $GroEL_{14}$ and $GroEL_{14}$-ATP_n, are consistent with changes in SASA of the complexes that have been noted for other systems[244, 245, 275] and with well-known cold- and heat-induced folding/refolding reactions of proteins and protein complexes.[276]

In the work presented below, the effects of temperature and ATP binding on the stability and conformation of GroEL, GroES, and GroEL/GroES complexes are investigated using vT-ESI native mass spectrometry.[110, 274, 277] Conformational changes induced by ATP binding as well as cold- and heat-induced changes in stabilities are directly linked to changes in Gibbs energy.[8, 244, 275, 278] The vT-ESI source is used to control the temperature of the protein-containing solution in the ESI emitter; consequently, the observed changes in stability/conformation are occurring in the solution prior to ESI ionization. While we cannot completely rule out that some reactions may occur in the confined environment of the nano-droplets formed by ESI, evaporative cooling of the nanodroplets has been shown to be an effective mechanism for kinetically trapping (freeze drying)[279] ions during the transition from solution to the gas-phase.[177, 279] The relationships between ESI freeze drying and cryo-EM have been noted previously[271] and is supported by detection of intermediates and final products that are similar to those previously reported by Ranson *et al.* using cryo-EM.[252] The

similarities between results obtained using native MS and cryo-EM,[252, 280] underscore the potential utility of native MS for investigations of molecular machines as well as identification of key intermediates that may be involved in the chaperone-assisted protein folding cycle.

4.2. Results

4.2.1. Thermal stability of GroEL and GroES as determined by vT-ESI native MS

Cooling and heating EDDA buffered solutions of GroEL contained within the ESI emitter over a temperature range from 8 – 50 °C did not result in significant changes in the average charge state (Z_{avg}), the charge state distribution (CSD) or the measured *m/z* values of $GroEL_{14}$ ions (**Figure 4.2A**); however, evidence for T-dependent stabilities for $GroEL_{14}$ are observed at T > 52 °C. The region of the mass spectrum shown in the inset of **Figure 4.2B** contains ions that have *m/z* values that correspond to $GroEL_7$ and $GroEL_{14}$-$GroEL_1$. Ions having similar *m/z* values are detected at 54 °C (**Figure 4.2C**); note the abundance of $GroEL_7$ ions (**Figure 4.2C**) is increased relative to that for $GroEL_{14}$-$GroEL_1$. This spectrum also contains low abundance ions that are assigned as $GroEL_1$ and $GroEL_2$. It appears that these ions are formed by solution-phase thermal decomposition of $GroEL_{14}$ The increased relative abundances for $GroEL_7$ and $GroEL_{14}$-$GroEL_1$ at 54 °C compared to 52 °C are consistent with a large shift in stability of the $GroEL_{14}$ (**Figure 4.6**). While we cannot rule out the possibility that some fractions of these ions are formed by gas phase collision-induced dissociation (CID), the increased in abundances of $GroEL_1$, $GroEL_2$ and $GroEL_7$ at 54 ° C

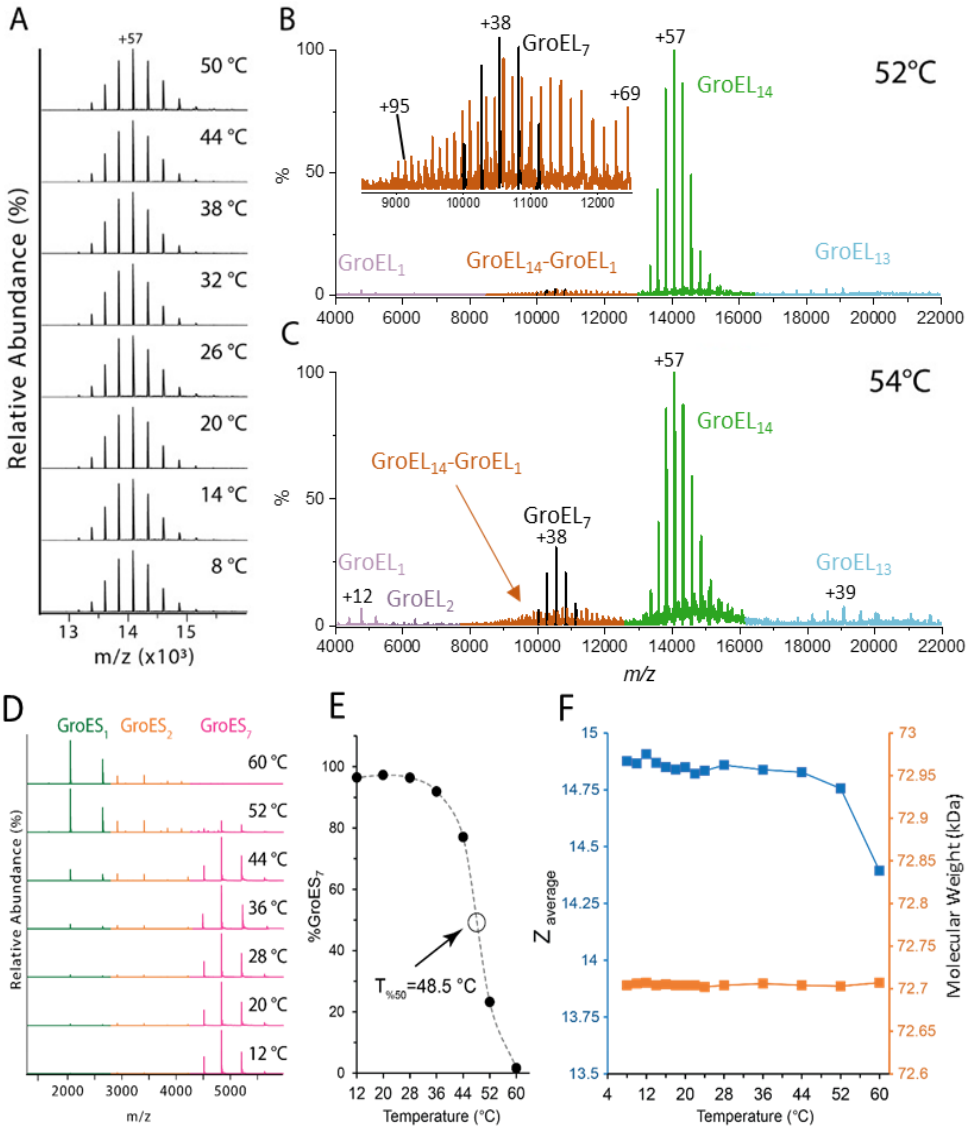

Figure 4.2 Effects of temperature on stability of $GroEL_{14}$ and $GroES_7$. (A) Charge state distribution (CSD) for intact GroEL tetradecamer (1.2 µM in 200 mM EDDA) at T = 8 – 50 °C, and the high m/z range (4,000-22,200) of mass spectrum of $GroEL_{14}$ acquired at (B) T = 52 °C and (C) at T = 54 °C; signals for $GroEL_7$, $GroEL_{14}$-$GroES_1$ and $GroEL_{14}$ are color coded in black, orange, and green, respectively. See supplemental material (Figure S2) for deconvoluted spectra. (D) Mass spectra of $GroES_7$ (7 µM, heptamer) in 200 mM EDDA at T = 12 - 60 °C. (E) A plot showing temperature dependent changes in the relative abundance of GroES7; signal intensity for GroES as a percentage of the total ion signal in spectra shown in (D). (F) Plot of average charge state (Zavg) (blue) and measured molecular weight (orange) of $GroES_7$ as a function of temperature.

The effects of heating and cooling the ESI solutions on the stability of $GroES_7$ were also investigated (**Figure 4.2D**). The $GroES_7$ complex is the most abundant species observed in the range of 12 < T < 28 °C, but at T > 44 °C there are notable increases in the abundances of $GroES_1$ and $GroES_2$ ions. Duckworth and co-workers assigned the fragment ions to gas phase collisional activation reactions;[281] however, based on a series of studies, we are confident that under these experimental conditions these product ions result from reactions that occur in the solution.[110, 282] The midpoint in the curve shown in **Figure 4.2E** denotes the temperature at which the relative abundance of the $GroES_7$ ion has been reduced by 50%, i.e., $T_{50\%}$ = 48.5 °C (see experimental section), which is significantly lower than the T_m of ~74 °C reported by Boudker et al.[283] It is important to note, however, that their ΔC_p vs. T curve revealed evidence for a low temperature endotherm at ~40 °C, which agrees well with our $T_{50\%}$ for $GroES_7$. Geels et al.[284] and Dyachenko et al.[285] have reported T_m data for GroES using mass spectrometry, and they report similar T_m values (~70 °C), but both of these studies were performed using ammonium acetate buffer. Moreover, the differential scanning calorimetry (DSC) and vT-ESI results reveal strong evidence for T-dependent instability,[283] and the vT-ESI results suggest that this transition may serve as the early steps leading to disassembly of $GroES_7$ complex. In both experiments it appears that these are reversible even for solutions that have been heated to 60 °C. These results and the lower charge states (Z_{avg} = 4.66 and 6.19, respectively) suggest that the $GroES_1$ and $GroES_2$ do not undergo irreversible unfolding upon heating in EDDA buffered solutions; consequently, T_m values determined by CD (circular dichroism) spectroscopy, report on

the 2° structure, whereas T-dependent measurements using native MS of protein complexes report changes in architecture, stoichiometry and quaternary structure, i.e., changes in SASA that accompany changes in tertiary and quaternary structure.

4.2.2. Temperature-dependent ATP binding to the GroEL$_{14}$ Complex

Dyachenko et al. previously reported thermochemical data (Ka) for ATP binding to GroEL$_{14}$.[272] While their measurements were performed on samples incubated at 25 °C, the actual temperature of the solution in the ESI emitter was not specified. Owing to the observed temperature-dependent stabilities for GroEL$_{14}$ in EDDA buffered solutions, we investigated the effects of temperature on ATP binding to GroEL for vT-ESI solutions with different Mg^{2+} and ATP concentrations. Galan et al. observed a low temperature endotherm of GroEL by DSC that they proposed as evidence for conformation changes for the GroEL$_{14}$ complex, specifically modifications of tertiary and quaternary structure and minor changes in secondary structure.[286] Similar conformational changes were also observed using fluorescence.[287] VT-ESI native MS can potentially provide additional evidence for conformational changes as well as how such changes affect ATP binding.

For GroEL$_{14}$ solutions containing 10 μM ATP (solution "A", see **Table 4.1**) the products observed in the spectra were GroEL$_{14}$-ATP$_{1-11}$ (**Figure 4.3A**) at low temperatures, but at higher solution temperatures, binding of ATP becomes less favorable (see **Figure 4.3A**). An increased concentration of ATP to 25 μM (**Figure 4.3B**) (solution "B", **Table 4.1**) yields GroEL$_{14}$-ATP$_{1-14}$ at 10 °C, but as T is increased, the abundances of all these products decrease, esp. for n > 7. Under these conditions ATP binding to the second GroEL ring is

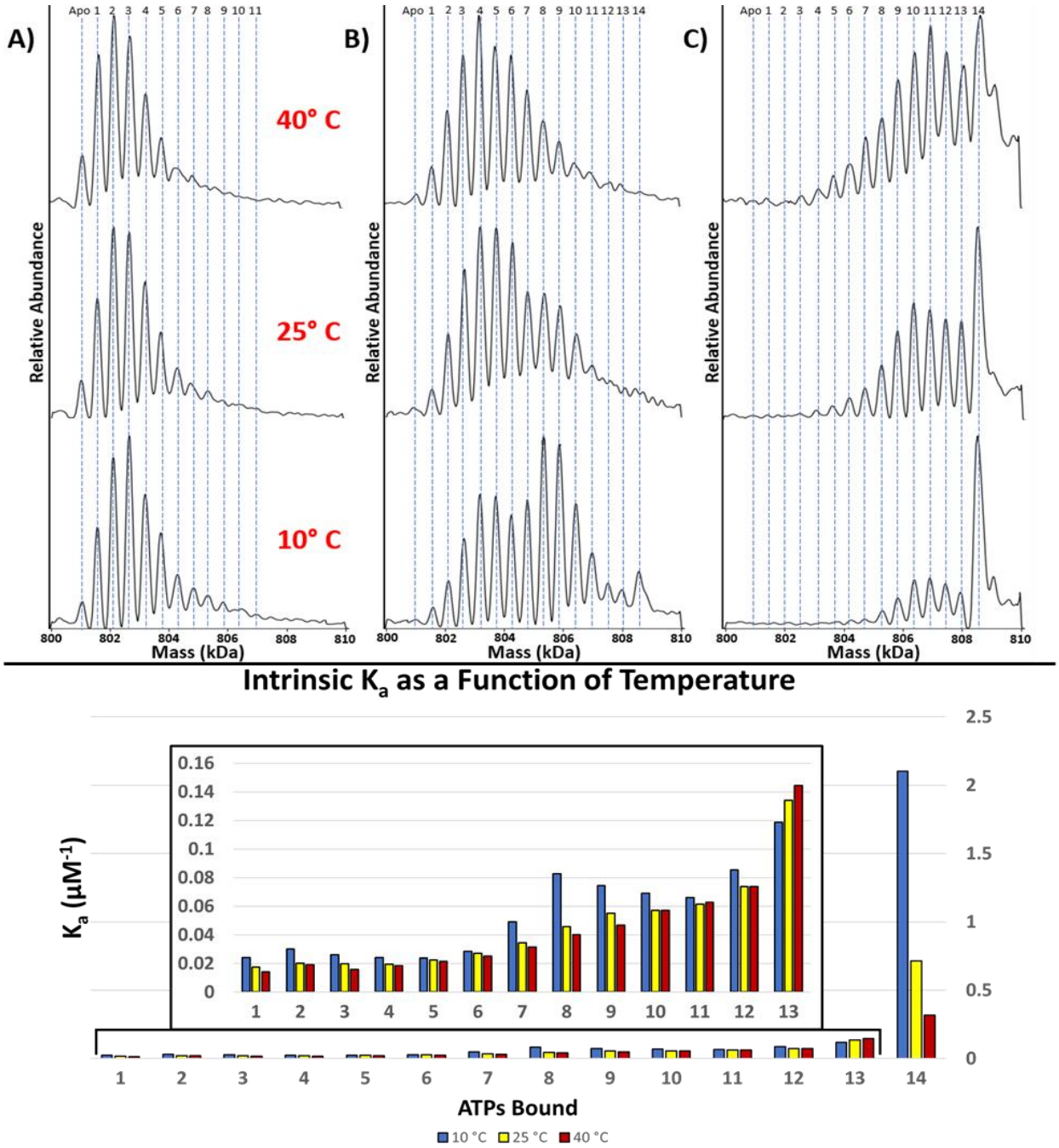

Figure 4.3 ATP binding is favored at low temperatures. Mass spectra of deconvoluted charge state of GroEL (0.5 µM, tetradecamer) in 200 mM EDDA and 1 mM Mg^{2+} incubated with ATP (A) 10 µM, (B) 25 µM and (C) 50 µM at different temperatures. (D) Calculated intrinsic association constants (K_a) for binding of ATP to GroEL 10 °C (blue), 25 °C (yellow), and 40 °C (red). Binding is more favorable at lower temperatures and affinity decreases with increase in solution temperature. Macroscopic K_a data and the methods used to calculate intrinsic K_a values are provided as supplemental information (Figure S2).

GroEL-$ATP_{3\text{-}6}$ (**Figure 4.3B**). Clearly lower solution temperatures are more favorable for ATP binding, and under these conditions the complexes also carry lower Z_{avg}, which is consistent with an ATP-induced conformational change of $GroEL_{14}$.[286] Z_{avg} trends as a function of temperature for GroEL-ATP_n in EDDA appear to be similar to those observed in **Figure 4.1**; stepwise addition of ATP induces a small decrease in Z_{avg} with each ATP bound. A similar temperature dependence is observed for solutions containing 50 μM ATP ("solution C", **Table 4.1**). Most notably the binding of 14 ATPs to $GroEL_{14}$ is highly favored compared to the previous binding events, but this effect diminishes at higher solution temperatures. While ATP and ADP are not distinguishable at the mass resolution used in this study, the affinity of GroEL for the binding of ATP is an order of magnitude greater than for the binding of ADP.[288] The ATPase activity of GroEL will also be negligible without the presence of K^+.[124, 289]

The higher relative abundance for $ATP_{3\text{-}5}$ and $ATP_{8\text{-}10}$ (**Figure 4.3B** 10 °C) raises an interesting question - is the binding of up to three ATP molecules at each ring more favorable than the remaining ATPs? Interestingly, Chapman *et al.* previously suggested that binding of three ATP molecules is required for successful substrate binding and release.[290] The intrinsic association constants (K_a) for temperature-dependent ATP-GroEL binding (10, 25, and 40 °C) are shown in **Figure 4.3D**. These K_a values show that ATP is bound with a higher affinity at lower temperatures and the affinities diminishes at elevated solution temperature. The intermediate (e.g., ATPs 7-10) and last (ATP 14) binding affinities are most affected by temperature (**Figure 4.3D**). The binding of the 14^{th} ATP draws particular interest due to the relative binding affinity compared to the other

affinities preceding it. These K_a values are consistent with positive cooperativity reported by Yifrach and Horovitz[121] and Dyachenko[272] for intra-ring-ATP binding – as reflected by the increase in the K_a values for the $GroEL_{14}$-ATP_{1-3} and $GroEL_{14}$-ATP_{7-8}.

4.2.3. Ligand- and Temperature-dependent stabilities of GroEL-GroES complexes

Results for temperature-dependent GroEL-ATP binding prompted further investigations on how solution temperature influences the binding of GroES to $GroEL_{14}$. As noted previously,[272] mass spectra acquired from EDDA-buffered solutions give well resolved peaks and are less congested, thereby greatly simplifying assignment of mass spectral signals. The mass spectra obtained from EDDA-buffered solutions containing a range of concentrations of $GroEL_{14}$, $GroES_7$, Mg^{2+} and ATP (**Table 4.1**) were examined. The mass spectrum obtained from solution "D" contain ions corresponding to $GroEL_{14}$-$GroES_{14}$-ATP_n, where n = 12 – 14, presumably the FS structure.[291, 292] Lorimer suggested that K^+ facilitates ATP turnover and promotes formation of the BS structure, $GroEL_{14}$-$GroES_7$-ADP, and serves as the acceptor state in the substrate refolding cycle.[293] Here, we avoided the effects of K^+ because this also further complicates assignment of the products observed in the mass spectrum. On the basis of preliminary data acquired from an EDDA solution containing K^+ (800 μM) we can report that the presence of K^+ significantly increases ATP binding but the stoichiometry of the resulting GroEL-GroES complexes does not change.

Table 4.1 The effects Mg^{2+} and ATP concentrations on ATP binding and stoichiometry of GroEL-ES complex at 24 ºC in 200 mM EDDA.

Solution "X"	**GroEL (nM)**	**Mg^{2+} (μM)**	**ATP (μM)**	**GroES (μM)**	**ATP/GroEL**	**Mg^{2+}/GroEL**	**$GroEL_x$-$GroES_y$-ATP_n**
A	500	1000	10	-	20	2000	$GroEL_{14}$- ATP_{1-4}
B	500	1000	25	-	50	2000	$GroEL_{14}$- ATP_{1-14}
C	500	1000	50	-	100	2000	$GroEL_{14}$- ATP_{3-14}
D	260	225	110	12	420	850	$GroEL_{14}$-$GroES_{14}$-ATP_{14}
E	120	25	50	12	420	200	$GroEL_{14}$-$GroES_{7-8}$-ATP_8
F	600	500	50	12	80	850	$GroEL_{14}$-$GroES_{7-8}$-ATP_8
G	600	25	50	12	80	40	$GroEL_{14}$-$GroES_{0-2}$-ATP_{0-2}
H	500	-	-	12	-	-	Not Detected

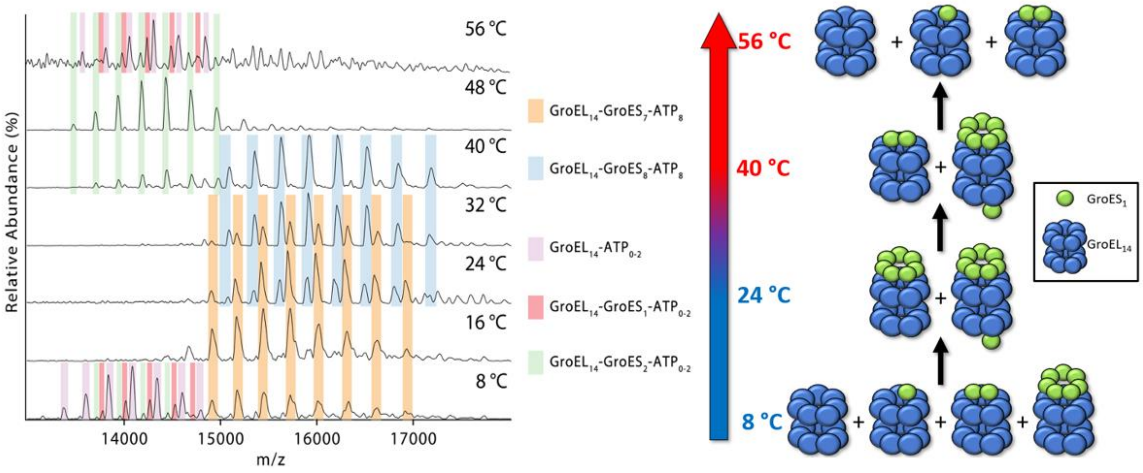

Figure 4.4. Mass spectra showing the region corresponding to the GroEL-GroES complexes formed in solution E (Table 1 solution "E" 120 nM GroEL, 12 μM GroES, 25 μM Mg^{2+}, 50 μM ATP in 200 mM EDDA). The accompanying illustration summarizes the observed products formed upon heating solution "E" at temperatures of 8 °C to 56 °C. Lower temperatures (8 °C) $GroEL_{14}$-$GroES_y$ (y = 0 - 2) products are formed, whereas $GroEL_{14}$-$GroES_7$ and $GroEL_{14}$-$GroES_8$ products are formed at higher temperatures. At T > 40 °C the observed species revert back to the lower mass complexes, which become the most abundant products at 48-56 °C.

The mass spectra shown in **Figure 4.4** were acquired from solution "E" (25 μM Mg^{2+} and 50 μM ATP) at temperatures between 8 °C and 56 °C. At the lowest temperature (8 °C) the spectra contain abundant ions corresponding to $GroEL_{14}$-ATP_{0-2} (violet), $GroEL_{14}$-$GroES_1$-ATP_{0-2} (magenta), $GroEL_{14}$-$GroES_2$-ATP_{0-2} (green), $GroEL_{14}$-$GroES_7$-ATP_8 (orange). Increasing the temperature to 16 °C results in formation of $GroEL_{14}$-$GroES_7$-ATP_8, and at 24 and 32 °C the major products correspond to $GroEL_{14}$-$GroES_7$-ATP_8 and $GroEL_{14}$-$GroES_8$-ATP_8 (blue); however, the ratios of these two products change in the range of 24 to 32 °C. At T > 40 °C the signal for these complexes is diminished, possibly a result of disassembly, first to form $GroEL_{14}$-$GroES_2$-ATP_{0-2} followed by formation of the initial products observed at 8 °C. The assignment of ATP_8 is consistent with measured mass differences for $GroEL_{14}$-$GroES_7$ and $GroEL_{14}$-$GroES_8$ masses and the measured mass of the $GroEL_{14}$-$GroES_7$ complex.

The mass spectrum obtained for solution "F" (**Figure 4.5A**), which has a higher concentration of ATP and Mg^{2+} than solution "D", is most similar to the mass spectrum obtained (at 24 °C) using solution "E"; however, the ratios of $GroEL_{14}$-$GroES_7$-ATP_8 and $GroEL_{14}$-$GroES_8$-ATP_8 are different. These results underscore the importance of both Mg^{2+} and ATP in determining the stoichiometry of GroEL-GroES complexes. The presence of $GroEL_{14}$-$GroES_1$ and $GroEL_{14}$-$GroES_2$ product ions (magenta and green, respectively) are very different from vT-ESI of solutions containing low Mg^{2+}/$GroEL_{14}$ and ATP/$GroEL_{14}$ ratios (solutions "E" and "F", respectively). Decreasing the ratio of Mg^{2+}/$GroEL_{14}$ and Mg^{2+}/ATP (solution "G" relative to solution "F" (**Table 4.1**)) results in a mass spectrum (**Figure 4.5B**) containing signals for $GroEL_{14}$-ATP_{0-2}, $GroEL_{14}$-

$GroES_{1\text{-}3}$-$ATP_{0\text{-}2}$, and low abundances of $GroEL_{14}$-$GroES_{7\text{-}8}$-ATP_8. The ions at higher *m/z* values are identical to ions observed from solution "F", whereas the ions at lower *m/z* correspond to $GroEL_{14}$-$GroES_{1\text{-}2}$. These results suggest that binding of $GroES_7$ to the GroEL-ATP complex is directly linked to the concentrations of both ATP and Mg^{2+} ions. The concentration of Mg^{2+} will also affect the effective concentration of ATP as Mg^{2+} is necessary for ATP to bind.[294] The binding of individual GroES subunits to GroEL has not been previously reported and seems counterintuitive. The binding of individual GroES subunits could explain the formation of $GroEL_{14}$-$GroES_8$ ions in solution "E". Presumably, the $GroEL_{14}$-$GroES_8$ complex has a single GroES subunit bound to the *trans* ring and an intact $GroES_7$ bound to the *cis* ring. VT-ESI analysis of solution "F" is similar to solution "E" in terms of increased abundances of GroEL-$ATP_{1\text{-}2}$ and $GroEL_{14}$-$GroES_2$-

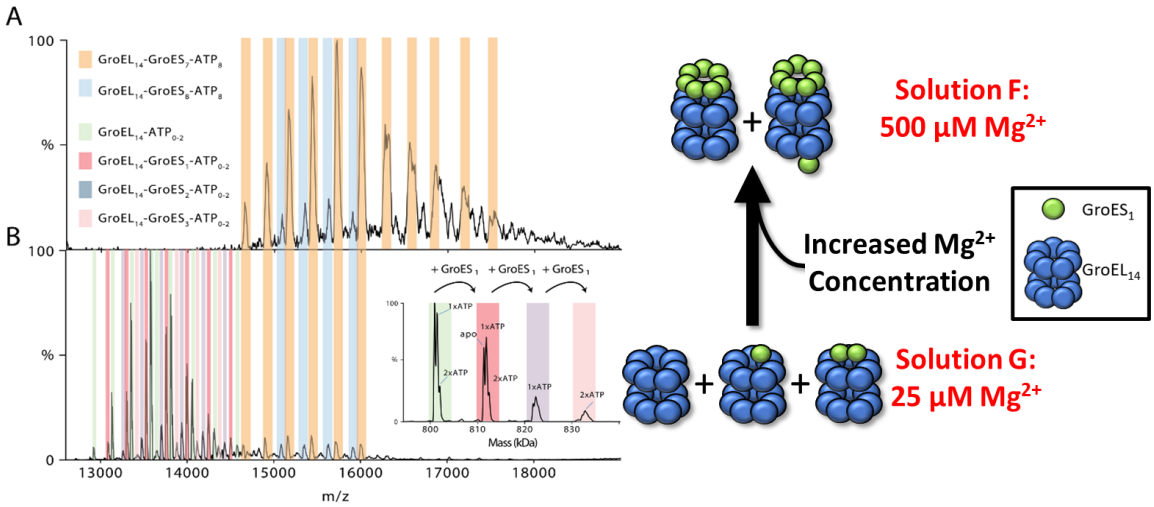

Figure 4.5. Mg^{2+} regulates the stoichiometry of GroEL-ES complex. (A) The mass spectra shown in (A) and (B) illustrate the effects of Mg^{2+} concentration on the formation of $GroEL_{14}$-$GroES_7$ and $GroEL_{14}$-$GroES_8$ complexes. The solution conditions used (solution F and solution G) only differ in concentrations of Mg^{2+}, (A) 500 µM and (B) 25 µM collected at 12 k resolution (HCD = 200 V) at 24 °C. The insert in (B) illustrates the resolving power available to assign the GroES bound state of the GroEL as well as the ATP bound state of each $GroEL_{14}$-$GroES_7$ state.

ATP_2 at 8 °C and ~50 °C, respectively. Collectively, the results suggest that these experimental conditions alter the stability/dynamics of the $GroES_7$ and/or the positioning of GroES with the apical domain of the GroEL complex.

The role of Mg^{2+} and ATP concentration on the stoichiometry of GroEL-GroES complex, specifically formation of sub-stoichiometric GroES complexes is illustrated by the data shown in **Figure 4.5.** The spectrum shown in **Figure 4.5A** was obtained from solution "F" (500 μM Mg^{2+}, 50 μM ATP, and 12 μM $GroES_7$), and the spectrum shown in **Figure 4.5B** was obtained from solution "G" (25 μM Mg^{2+}, 50 μM ATP and 12 μM $GroES_7$). The solution containing higher Mg^{2+} concentration produces higher abundances of $GroEL_{14}$-$GroES_7$-ATP_8 and $GroEL_{14}$-$GroES_8$-ATP_8. Low abundance signals for the same complexes are formed at low Mg^{2+} concentrations (25 uM), but the dominate species correspond to $GroEL_{14}$-$ATP_{0\text{-}2}$, $GroEL_{14}$-$GroES_n$-$ATP_{0\text{-}2}$, where n = 1-3. Moreover, GroEL-GroES complexes are not detected from solutions that do not contain ATP and Mg^{2+} (solution "H"). Collectively, these results corroborate the role of Mg^{2+} in driving the reaction. Boudker *et al.* previously reported Mg^{2+}-dependent stability for $GroES_7$ (K_d ~ 0.5 mM),[283] and Sakane *et al.* reported reduced stabilities for $GroES_7$ at low concentrations.[295] Studies are currently underway, including vT-ESI, in an effort to better understand the underlying mechanisms that favor formation of sub-stoichiometric GroEL-GroES complexes.

4.3. Discussion

The vT-ESI GroEL studies were limited to a single native MS buffer EDDA owing to greater stability and structural integrity when compared to that for the more commonly used native MS buffer ammonium acetate.[21,[274]] The charge states produced from ammonium acetate solutions differ from those in EDDA, and the data shown in **Figure 4.1** and **Figure 4.2** reveal differences in thermal stability of GroEL in the different buffers. The upregulation of heat shock proteins and chaperonins raises questions of how the GroEL-GroES system responds to both cold and hot conditions. Temperature has strong effects on the dielectric constant of water[296] as well as the Gibbs free energy of the system, both of which have direct effects on protein structure. In general, cold denaturation favors more compact conformers, owing to solvent penetration of the protein, and heat denaturation favors elongated conformers.[297] Both cold- and heat-induced conformational changes are evidenced by changes in the SASA (see **Figure 4.1**).[297] Our results show that both GroEL and GroES are stable up to ~50 ^{o}C and 44 °C in EDDA, respectively, but this is limited to a relatively narrow range of concentrations, as evidenced by temperature-dependent ATP binding for $GroEL_{14}$ and changes in SASA for both $GroEL_{14}$ and $GroES_{7}$. The discrepancies between the previously reported thermal stabilities of GroEL (T_m ~67 °C)[254] and GroES, (T_m ~76.4 °C)[283] and our results may be due to differences in solution conditions. Moreover, the previously reported T_m values were determined using biased techniques, *viz.* CD spectroscopy, which measures changes in 2° structure; native MS reports changes in Z_{avg}, related to changes in SASA, as well as T-dependent changes in ligand binding. As shown in **Figure 4.2E and 4.2F**, there are no

significant changes in Z_{avg} for $GroES_7$ at T < 44 ^oC, but at T > 44 ^oC signals for $GroES_1$ and $GroES_2$ ions appear. Note, however, that at T > 44 ^oC the mass and charge state distribution (CSD) of GroES heptamer are unchanged, which suggest that these ions are native-like. GroEL, GroES, and GroEL/GroES complexes are highly dynamic, and even small changes in the solution conditions, *viz*. chemical potential (Gibbs free energy) of the local environment (T, P, pH, osmolytes, chemical chaperones, concentration of GroEL/GroES), strongly affect conformation, stability, and possibly the behavior of these nanomachines. This explanation is consistent with the previously reported low temperature endotherm in the DSC profiles detected at ATP concentrations of 0.25 and 0.50 mM;[286] these authors note "existence of a conformational state of GroEL with modified 3°/4° structures having increased exposure of hydrophobic surfaces, but minor rearrangements of its 2° structure."

We show that in EDDA solutions, $GroEL_{14}$ becomes unstable above 50 °C and unfolding of the monomer resembles previously reported self-chaperonin activity of GroEL[254] even though the size of GroEL monomer ($GroEL_1$: ~57 kDa) is near the limit of substrate size reported previously, ~70 kDa.[254] This self-protection mechanism in response to heat shock stress is evidenced by our observation of a highly stable octamer in ammonium acetate that most likely consisted of a single ring GroEL and a trapped unfolded subunit that cannot be dissociated in the gas phase (data not shown). We conjecture that such high stability plays a role in the capability of this chaperonin to regain its functionality after removal of heat stress. The self-assembly and monomer unfolding

can be connected to a reversible, low-temperature endotherm reported from thermodynamics measurements of GroEL.[286]

Disassembly of $GroES_7$ at elevated temperatures (T > 44 °C) can be attributed to the increased coulombic repulsion of negatively charged residues, Glu50 and Glu53, localized on the roof of the $GroES_7$ complex and near the subunit-subunit interface.[298, 299] The CSD and Z_{avg} of unfolded subunits are not detected by native MS experiments upon heating up to 60 °C, suggesting that dissociation of subunits precedes the backbone unfolding. Supporting evidence for this statement is the observed reassembly of $GroES_7$ upon cooling the solution. The native MS studies performed at sub-ambient temperature (T < 24 °C) do not reveal changes in quaternary structures of $GroEL_{14}$ and $GroES_7$ which might be expected for assembly mechanisms involving purely hydrophobic interactions; however, for GroEL, hydrogen bonds and salt bridges are known to provide stabilization of the complex.[122, 254, 300-302]

4.3.1. Impact of ions and small molecules on GroEL-GroES function:

Physiological function of molecular chaperones such as GroEL are ATP-, Mg^{2+}-, and K^+-dependent,[261, 303] and nucleotide hydrolysis serves as the energy source to power specific conformational changes.[262, 304] Solution temperature can significantly influence the thermodynamics and kinetics of small molecule binding. High resolution native MS and vT-ESI afford means to study these binding events with unprecedented detail at concentration levels that mimic physiological conditions, including experimental conditions that allow final products to be analyzed. On the other hand, native MS affords

the ability to investigate chaperones over a range of experimental conditions that may reveal previously hidden details, e.g., the presence and roles of intermediates that are either off- or on-pathway to final products. As a single example, the fact that ATP binding is diminished at elevated temperatures provides a clue regarding the contribution of ionic interactions, with a major role of the phosphate group compared to the hydrophobic moiety (adenosine).[304] The formation of ADP, which is expected to increase the heterogeneity of the system, is inevitable in our experiments; however, because ADP is similar to ATP in thermochemistry, it does not interfere with the vT-ESI of GroEL-GroES complex. In fact, we have previously shown that ADP binding to GlnK is enthalpically driven and disfavored at elevated temperatures.[8] Moreover, we cannot rule out the contribution of conformational dynamics of GroEL, mainly local destabilization of nucleotide binding and the observed changes in ATP binding at elevated temperatures. Nevertheless, our data not only provide insight into effect of temperature on ATP binding but also on ATP-induced conformational change on GroEL. The observed decrease in the Z_{avg} of $GroEL_{14}$-ATP complex compared to apo-$GroEL_{14}$ is consistent with structural rearrangement or conformational drift that has been previously reported.[305]

4.3.2. T-dependent GroEL-GroES interactions

Cold-induced disassembly of protein complexes is associated with a decreased entropic penalty for ordering water near hydrophobic residues.[276] The disassembly of $GroEL_{14}$-$GroES_7$, the BS structure, at T < 8 °C points to a major contribution of hydrophobic interactions, mainly engagement of GroES “mobile loop” with apical domain

of GroEL.[306] Previously, Todd *et al.*[123] reported fast release of $GroES_7$ from $GroEL_{14}$-ADP complex at 4 °C, corroborating the role of hydrophobic interactions in this binding process.

The higher stability of the FS structure ($GroEL_{14}$-$GroES_{14}$) compared to the BS complex at low and high temperatures suggests that the apo ring might compromise the stability of GroEL ring capped with $GroES_7$. In other words, the structural changes in the free ring upon heating or cooling the solution destabilizes the subunit-subunit interactions in the GroES-bound ring to disrupt GroES binding. Additional evidence for compromised inter-ring stability of the BS complex is the observation of single ring GroEL ($GroEL_7$) in the vT-ESI of $GroEL_{14}$ (**Figure 4.2**). Our data suggest that heat-induced unfolding of GroEL subunits destabilizes the subunit-subunit interactions between two rings. In fact, our results show that subunit unfolding precedes the appearance of single ring and suggests that unfolding of GroEL subunits in one ring disfavors intra-ring interactions. Such ring splitting of $GroEL_{14}$ has been previously reported under heat shock conditions,[307] and the importance of such effects serves as the basis for planned future studies – the target being how $GroES_7$ binding to both rings seems to inhibit such conformational changes and increases the stability of complex over a broader range of temperatures. The fact that the FS structure is fully loaded with ATP molecules might also enhance the stability of $GroEL_{14}$-$GroES_{14}$ complex. Furthermore, the resistance of the FS structure against cold and hot treatment points out to the limited dynamics of this structure and in contrast to GroEL biological function. On the other hand, previous studies have

shown that ADP-bound BS structure is the acceptor state of GroEL-GroES system and is more physiologically relevant.[308]

The observation of intermediates, such as $GroEL_{14}$-$GroES_{1\text{-}2}$, upon both cooling and heating of the BS structure is an unexpected result as is the observation of $GroEL_{14}$-$GroES_8$ at temperatures between 24 - 40 °C. The increased abundances of these complexes at elevated temperatures can be justified based on temperature- and concentration-dependent stabilities of $GroES_7$.[283, 295] The formation of $GroEL_{14}$-$GroES_{1\text{-}2}$ at both low (8 °C) and high temperatures (up to 56 °C) can be explained by temperature-dependent disassembly of the $GroES_7$ complex, and this is supported by the 0.5 mM K_d reported by Sakane et al.[295] and Boudker et al.,[283] which raises yet another possible explanation. Specifically, that a destabilized $GroES_7$ binds to the apical domain of GroEL through a limited number of GroES subunits and the exposed subunits then reorganize and disassemble. Evidences for this hypothesis are the reported instabilities previously reported[283, 295]which are further supported by the effects of Mg^{2+} concentration shown in **Figure 4.5**. Lastly, these intermediates are only observed in Mg^{2+}- or ATP-deprived solution, which corroborates their transient nature.

The number of bound ATPs required for GroEL and GroES interaction as well as substrate refolding has been previously investigated by Chapman *et al.*[290] In their study, ATP binding to a GroEL mutant (I493C) was inhibited in the presence of the cyclopentane-carboxamide derivative molecule, EC3016. It was shown that only 50% of W2M5 complex (W: wild type and M: mutant) is capable of binding GroES in the presence of an inhibitor, and at least three ATP molecules are required for GroES binding. Here,

we observed binding of 1-3 individual GroES subunits to GroEL in solutions where Mg^{2+} and ATP concentrations are below physiological concentration, which are highly variable.[16] We discount the possibility that these products are formed by dissociation of a $GroES_7$ that is bound to the GroEL apical domain; however, we also detected a correlation in the number of ATP molecules bound to GroEL and the stoichiometry of $GroEL_{14}$-$GroES_x$-ATP_n complex. For n = 1-3, up to two GroES subunits are able to interact with GroEL and increasing Mg^{2+}/ATP concentrations increases ATP binding, $6 < n < 9$ as well as binding of intact GroES ($GroES_7$). We propose that binding of ATP_{1-4} can allow for rotation of the apical domain of GroEL to recruit individual GroES subunits but not enough to allow for binding intact GroES.[43] Specifically, binding of intact co-chaperone requires specific amounts of Mg^{2+} and in its absence binding of ATP_n molecules ($n > 5$) is not sufficient to capture the native GroES complex. Previously, Azem *et al.* showed that Mg^{2+} not only increases ATP binding and hydrolysis but also increase the dynamics of GroEL.[303]

The X-ray structure of $GroES_7$ provides more insight into observations of individual subunits of GroES binding to GroEL. Hunt *et al.* discovered an unexpected asymmetry in terms of subunit-subunit interactions in $GroES_7$ structure as well as interfacial residues.[298] In fact, R47 and K55 residues form salt bridges with neighboring residues in only two subunits and these stabilizing interactions are missing in the other five subunits. This structural heterogeneity[285] might also explain the observation of monomer and dimer ions in native mass spectrum of $GroES_7$ (**Figure 2.3**) and previous studies.[281, 285] The $GroEL_{14}$-$GroES_{1-3}$ complexes may be formed by reactions with

$GroES_1$ and $GroES_2$ binding to the hydrophobic (apical) domain similar to that for unfolded substrates. Alternatively, we cannot rule out the possibility that the energy requirement for disassembly of the GroES complex can be compensated by the binding energy to $GroEL_{14}$. Previous studies have shown that both ATP and GroES binding are necessary for apical domain movement and for transition from substrate-binding mode (hydrophobic surface exposed) to the folding-active state (hydrophilic chamber).[309, 310] The role of GroES binding in this transition suggests an alternative mechanism under extreme conditions wherein sequential binding of GroES subunits to GroEL may indeed become favorable. These factors may also have implications in refolding of multi-domain proteins where $GroES_y$ binding ($y < 7$) could allow for partial or full release of a single GroES subunit, providing the gap necessary for a piece of polypeptide to extrude to the exterior of the GroEL-GroES complex.[311, 312]

The vT-ESI data offer insight into thermal stability of $GroEL_{14}$-$GroES_{1-3}$ complexes. The higher abundance of $GroES_1$ and $GroES_8$ at 32 °C < T < 40 °C (**Figure 4.4**) indicates that binding of a single GroES subunit to a GroEL ring is thermodynamically stable, whereas increasing temperature favors binding of two subunits (~44 °C). Above this temperature both GroEL and GroES become unstable and GroEL-GroES interactions are lost. At low temperatures, also due to the hydrophobic nature of the GroEL-GroES interaction, these intermediates are no longer formed. Overall, these results showcase the power of native high-resolution MS and vT-ESI to investigate the role of nucleotide and small molecules in chaperonins and their interaction with co-chaperonins. Future studies with substrate can shed light on the thermal dependency of

protein chaperonins and substrate interactions and cofactors roles in driving the refolding reaction.

4.4. Experimental Data and Materials

4.4.1. Materials:

All reagents including magnesium acetate and EDDA were purchased from Sigma Aldrich (St. Louis, MO). GroEL and GroES were over-expressed in *E. coli* as described previously.[313] Adenosine triphosphate sodium (ATP) was purchased from Jena Bioscience and dissolved in deionized water (Barnstead Easy Pure II, Thermo Scientific). Sample aliquots were stored at -20 °C and freshly diluted with water then added to protein prior to analysis. Protein concentration was measured using Bradford assay and are for tetradecameric and heptameric proteins unless otherwise mentioned. Fresh GroEL (6 µM, 10 µL) and GroES (60 µM, 10 µL) were diluted three-fold with EDDA and buffer exchanged into buffer using Micro Biospin P-6 gel column (BioRad).

4.4.2. Native mass spectrometry:

Mass spectra of proteins were collected on a Q Exactive UHMR (Ultra-High Mass Range) Hybrid Quadrupole Orbitrap Mass Spectrometer (Thermo Scientific, CA) with the mass range of 350-80000 *m/z*. The instrument was calibrated using CsI (2 mg/ml in 50:50 IPA: H_2O) in positive mode. Capillary voltage varied from 1.0 - 1.6 kV for the highest signal and better desolvation. To obtain better resolved peaks, in-source trapping and activation (150 – 250 V) was used; higher collision energies are important for solution

with higher Mg^{2+}/ATP concentration. To increase the mass accuracy and ion abundances, HCD activation was also used (150-250 V) for ATP binding studies. The temperature of the instrument ion source was maintained at 100 °C for all the vT-ESI experiments. The temperature of the instrument ions source was varied to promote better desolvation and more abundance ion signals. The temperature of the vT-ESI source was controlled as described previously.[274] For melting experiments the response factors for multiple oligomeric states of the complexes in question were assumed to be identical, meaning that the detection of all signals for all *m/z* values were assumed to be unbiased. Mass spectra analyses were performed using UniDec[314] and/or Protein Metrics Intact Mass™ to determine the average charge state and experimental molecular weights. The Z_{avg} for $GroEL_{14}$-ATP_n was calculated by averaging the Z_{avg} for individual ATP bindings.

4.4.3. ATP Association Constants:

The K_a values for the binding of ATPs 1-14 by $GroEL_{14}$ were calculated using an ATP titration study. The solution conditions were 500 nM $GroEL_{14}$ in 200 mM EDDA buffer with 1 mM MgAc. ATP concentrations used in the study were: 0, 0.2, 0.4, 0.6, 0.8, 1, 2.5, 5, 10, 15, 20, 25, 30, 40, and 50 μM. Each concentration was analyzed at 3 different temperatures (10 °C, 25 °C, and 40 °C). The solution temperature was allowed to equilibrate for a minimum of 3 minutes before the measurement was conducted. Mass spectra were deconvoluted using UniDec and incorporated the 4 most abundant charge states of the $GroEL_{14}$-ATP_n distributions in each spectrum for the deconvolution. Macroscopic association constants (K_a) for ATP binding to $GroEL_{14}$ were calculated using

a sequential ligand binding model. Macroscopic K_a values were then statistically corrected to render intrinsic K_a values.

The binding constants were calculated using the **Equation 4-1** and then were statistically corrected using **Equation 4-2**.[315, 316] The statistical correction accounts for the number of sites available for a ligand (ATP in this case) to bind or dissociate. Sharon *et al.* discuss these equations in much more detail, especially in the supplemental information.[2]

Equation 4-1

$$K_i^{app} = \frac{I_i}{I_{i-1}[S]_{free}}$$

Equation 4-2

$$K_i^{app} = \frac{N - i + 1}{i} K_i^{int}$$

Where K_i^{app} is the apparent binding constant, I_i is the intensity of the ith bound ATP, I_{i-1} is the intensity of the preceding binding, and $[S]_{free}$ is the free ligand concentration. Where N is the number of total binding sites, i is the number of bound ATPs, and K_i^{int} is the intrinsic binding constant.

4.4.4. vT-ESI-MS experiments:

The temperature of the solution contained in the ESI emitter is controlled using a vT-ESI apparatus that has been described previously.[274] Briefly, the ESI emitter is positioned within an aluminum block and the temperature of the Al block is heated/cooled using a 3-tier Peltier chip controlled by a thermoelectric cooler (Meanwell LRS-100 24).

A ceramic rod also transferred heat efficiently from emitter. Borosilicate glass capillary tips were pulled in house using Sutter 1000 and ions were generated via a platinum wire inserted into the capillary. The temperature of solution in vT-ESI was calibrated using a T-Type thermocouple (Physitemp Clifton, NJ) inserted into the capillary.

4.5. Conclusion

Variable-temperature ESI native mass spectrometry was used to investigate the effects of ATP and GroES binding on the stability of the GroEL complex. This approach complements similar studies performed using differential scanning calorimetry (DSC), the traditional method used for studies of protein heat capacities (ΔC_p) and determinations of melting temperature (T_m).[96] The sensitivity and dynamic range of native MS afford the ability to detect previously hidden products, non-native states as well as reaction intermediates, including changes in the structure/conformation of the protein complex.[96] Temperature-dependent changes in structure/conformation originate from changes of both secondary (2°), tertiary (3°), and/or quaternary (4°) structure of protein complexes. T_m values for a given protein or protein complex may vary depending on solution conditions, solvent, pH, pressure, ionic strength, and presence/absence of other solutes, all of which contribute to the Gibbs energy of the system. Oftentimes low energy endotherms, changes in ΔC_p that occur at temperatures below the T_m, are observed owing to formation of misfolded states and/or subtle changes in conformation, changes in 3° structure ("conformational drift") under conditions whereby 2° structure is retained. The changes in Z_{avg} obtained using vT-ESI native MS also reflect temperature-dependent and

ATP-dependent conformation changes of GroEL and the GroEL-GroES complexes that arise from changes in the solvent accessible surface area (SASA) of the proteins that accompany ATP binding. Galan *et al.*[286] reported low temperature endotherms associated with ATP binding to GroEL using DSC; however, as noted above, the origin(s) of the ΔC_p signals are difficult to assign from such measurements.

In summary, this work demonstrates the utility of vT-ESI and high-resolution native mass spectrometry to investigate the role of co-factor and co-chaperone molecules in stability of chaperonins using a broad range of experimental conditions. Our results specifically shed light on the thermal stability of GroEL, GroES, and GroEL-GroES intermediates resulting from cooling and heating the solution. Although evidences for thermal instabilities of GroEL and GroEL-GroES complexes have been observed previously,[286] the specific effects have not been fully characterized. Thermodynamic studies, inclusive of ΔG, ΔH, and $T\Delta S$ that are currently underway, can reveal even greater insights on the formation of these complexes and for ATP binding that may provide greater details and may provide even further understanding of the GroEL/GroES operational mechanism. Nonetheless, this study clearly illustrates the utility vT-ESI native mass spectrometry for analysis of biologically complex systems. The presence of intermediates and their role/impact on the operation of the GroEL molecular machine are still open to debate, especially the potential role that the effects note in this study might impact our views of folding/refolding of non-native substrate proteins.

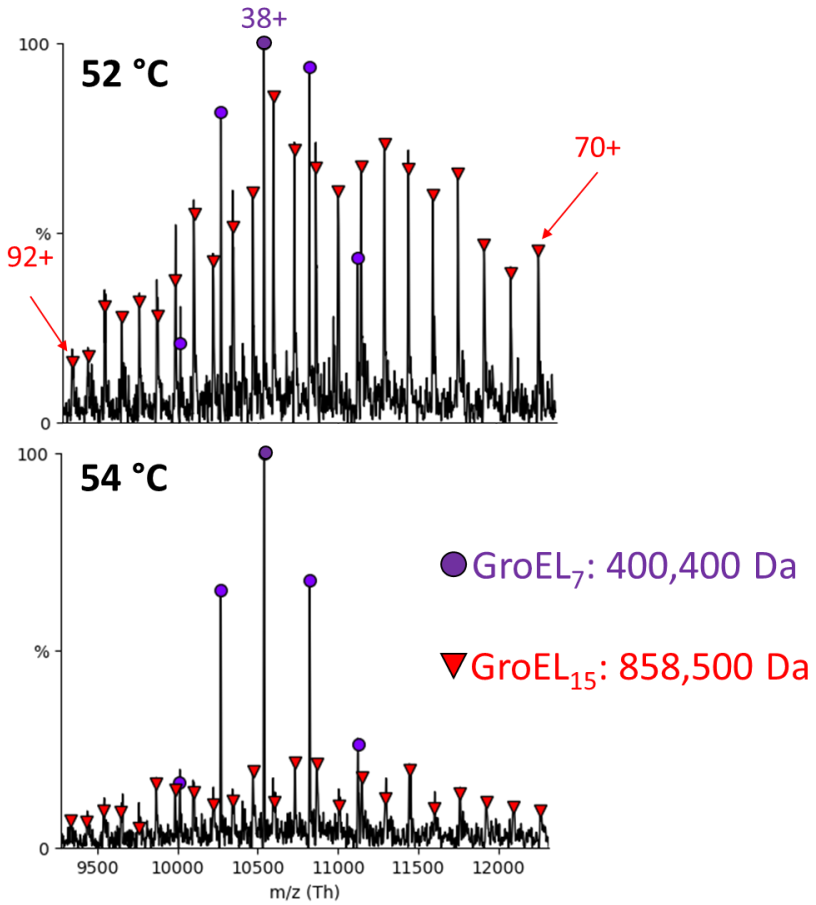

Figure 4.6 Temperature stability of $GroEL_{14}$. Mass spectra (Figure 2) of GroEL acquired at 52 and 54 °C provide evidence for thermal decomposition of $GroEL_{14}$. The most abundant signals in the m/z range from ~9,000 to 12,500 are assigned to $GroEL_7$ (36^+ to 40^+) and a series $GroEL_{15}$ ions (charge states 70^+ to 92^+); mass and charge assignments were initially determined using ProteinMetric Intact Mass™ program. Solution conditions used to acquire the mass spectra differ only in the temperature of the ESI solution. The most abundant ions detected at 52 °C correspond to $GroEL_7$ (blue circles) and $GroEL_{15}$ (red triangles), and at 54 °C the signals for $GroEL_7$ dominate the spectrum. The $GroEL_7$ charge state distribution (CSD) is consistent with a native-like heptamer, whereas the CSD for $GroEL_{15}$ is broad and consistent with non-native oligomers. The increased relative abundances for $GroEL_7$ are attribute to a reduction in the abundances $GroEL_{15}$ signals at 54° C spectrum vis-à-vis an increased abundance of $GroEL_7$. This assignment is based on comparisons of signal-to-noise ratios of the two spectra. At higher temperatures the signals for $GroEL_{15}$ are lower, possibly indicating that higher temperatures promote higher order oligomers that precipitate from solution.

The mass assignments for $GroEL_7$ and $GroEL_{14}$-$GroEL_1$ ions is supported by excellent agreement between calculated isotopically averaged mass and experimentally measured mass of 400.47 kDa vs. 400.40 kDa, and 858.5 ± 1 kDa vs. 858.0 kDa, respectively.

5. BINDING OF ATP TO GROEL: A CASE FOR VARIABLE-TEMPERATURE NATIVE MASS SPECTROMETRY THERMODYNAMIC STUDIES

5.1. Abstract

Understanding how large, oligomeric protein complexes respond to the binding of small ligands and other proteins is essential for describing the molecular basis of life. This in turn requires a complete characterization of the binding energetics and correlation of thermodynamic data with interacting structures, including effects of small molecules and solvent. However, the size of many protein oligomers, the myriad intermediate ligation states they can populate, and their often complex allostery typically restrict analysis by traditional methods to low resolution, ensemble averages. Here, we employ variable-temperature electrospray ionization native mass spectrometry to determine the thermodynamics for step-wise binding of ATP ligands to the 801 kDa GroEL complex—a tetradecamer chaperonin complex capable of binding up to 14 ATP molecules. Strong enthalpy-entropy compensation (EEC) and high degrees of cooperativity are observed for formation of GroEL-ATP_7 and GroEL-ATP_{14}, as evidenced by entropy favored ATP binding to the *cis* ring (formation of GroEL-ATP_{1-7}), with variations in EEC for subsequent binding of ATP to the *trans* ring (GroEL-ATP_{8-14}), as expected for negative inter-ring cooperativity. Entropy driven ATP binding to the GroEL tetradecamer is consistent with ligand induced conformational changes of the GroEL tetradecamer, though the magnitude of the entropy change suggests that reorganization of GroEL-hydrating water molecules and/or expulsion of water from the GroEL cavity may also play a key role. By permitting

the thermodynamics of individual ligand binding reactions to be specified for a large, nearly MDa complex, this approach fundamentally expands our view of chaperonin functional chemistry. Moreover, this work and related studies of lipid-membrane protein complex interactions illustrate unparalleled capabilities of vT-ESI-nMS for thermodynamics studies of protein-ligand and protein-protein interactions.

5.2. Background

Electrospray ionization native mass spectrometry (ESI-nMS) has evolved as powerful method for studies of protein-cofactor, protein-ligand, and non-covalent protein-protein interactions. MS-based strategies are attractive because they require only very small amounts of sample, permit product stoichiometries to be directly obtained and allow reaction kinetics and thermodynamics can be quantified. Klassen and co-workers recently reported a new strategy, "quantifying biomolecular interactions using slow mixing mode (SLOMO) novel nanoflow ESI-MS", for determination of equilibrium binding affinities (K_D at 25 °C)) for biomolecular interactions, [317] and they demonstrated the utility of this approach for a number of peptide- and protein-ligand systems. Interactions of proteins with cofactors, ligands and other proteins often result in conformational changes and/or reorganization of solvent that result in substantial shifts in enthalpy (ΔH) and entropy ($-T\Delta S$). At the same time, solution temperature, pressure, and concentration can influence changes in the "native" structure of biomolecules through manipulation of these thermodynamic contributions.[90, 91, 96, 103] Changes in thermodynamic contributions are often hallmarks of changing conformational states and vice-versa.[96]

Thermodynamic analysis is thus a powerful approach for probing fundamental mechanisms as well as for extracting critical information on structure-activity relationships that are important for drug discovery and drug design, including water-mediated interactions.[318-320]

Electrospray ionization produces ions by formation of nanodroplets from which solvent rapidly evaporates, and the associated evaporative cooling of the nanodroplet contents to temperatures of 130-150 K.[19] Beauchamp and coworkers described this evaporative drying process as "freeze-drying". We have used this approach to track the structural evolution of hydrated biomolecules in route to forming solvent-free, gas-phase ions,[176] and we, and others, have shown that this approach can be used to capture native and non-native protein states that co-exist in solution. These conditions are similar to cryogenic-electron microscopy (cryo-EM) structures of large molecule complexes that are obtained from water droplets that are rapidly cooled to cryogenic temperatures. There exist important parallels between cryo-EM ESI-MS/cryo-IM-MS (*vide infra*) in that both techniques take advantage of kinetic-trapping of molecules as they exist in solution.[5, 12, 185]

While traditional solution-based techniques can be used to robustly examine temperature-dependent interactions between biomolecules and their ligands, they generally report the ensemble average of ligand bound states present in solution. Recent work leveraging the molecular resolution of nMS has shown that species-resolved thermodynamic analysis is possible.[8, 15, 321] Combined with nMS, vT-ESI allows for thermodynamic measurements of solution-phase structures with the benefit of mass

separation.[3, 13, 15] This type of species-specific thermodynamic analysis can be especially valuable for complex or heterogeneous protein-ligand systems where the binding mechanism fundamentally changes as a result of a perturbation or shift in conditions without a measurable alteration to the observed Gibbs free energy (ΔG). In these cases, enthalpic and entropic contributions to the Gibbs free energy shift in opposite directions, a phenomenon known as enthalpy-entropy compensation (EEC). [104, 108, 322-324]

We previously reported EEC results for protein complex-lipid binding that varied with lipid head group, tail length and showed that mutant forms of AmtB altered phosphatidylglycerol (PG) binding site having distinct changes in the thermodynamic signatures.[8] VT-nESI studies of lipid binding to the human G-protein-gated inward rectifier potassium channel, Kir3.2, displays distinct thermodynamic strategies to engage phosphatidylinostitol (PI) and phosphorylated forms. The addition of a 4'-phosphate to PI results in an increase in favorable entropy. PI with two or more phosphates exhibits more complex binding, where lipids appear to bind to nonidentical sides on Kir3.2; interactions of 4,5-bibis-phosphate with Kir3.2 is solely driven by large, favorable entropy whereas 3'phosphate to PI(4,5)P_2 displays altered thermodynamics.[15] The lipid acyl chain has a marked impact on binding thermodynamics, and in some cases enthalpy is favored. More recent studies using vT-ESI nMS combined with ion mobility showed that IscU exists in structured, intermediate, and disordered forms that rearrange to more extended conformations at higher temperatures. Comparisons of Zn-IscU and apo-IscU reveals that Zn(II) binding attenuates the cold/heat denaturation of IscU, promotes refolding of IscU,

favors the structured and intermediate conformations, and inhibits formation of the disordered high-charge states.[325] Finally, these results provide a structural rationalization for the role of Zn(II) in stabilizing IscU conformations and IscS in altering the IscU active site to prepare for Zn(II) release and cluster synthesis. Collectively, these studies highlight how vT-ESI-nMS can be applied as a powerful approach for studies of relationships among temperature, conformation and ligand interactions in a complex biomolecular system.

Molecular chaperones represent another large class of essential biomolecules for which ligand binding and conformational changes are intimately linked to function. The chaperonin family of molecular chaperones, or Hsp60s, are large oligomeric protein complexes that utilize the energy of ATP hydrolysis to actively facilitate protein folding. The canonical bacterial chaperonin, GroEL, is an 801 kDa tetradecamer protein complex from *E. coli* that consists of two heptameric stacked rings. Each GroEL subunit consists of three domains—apical, intermediate, and equatorial.[112-114] The apical domain is highly dynamic and is responsible for binding protein substrates and the co-chaperonin GroES. The intermediate domain acts as a hinge between the equatorial and the apical regions of each subunit, and the equatorial domain of each subunit is the least dynamic and serves as the interfacial contact between each heptameric ring. [115-118] The equatorial domain also harbors the ATP binding site for each subunit.[113] While the structure, dynamics, and ATP binding of GroEL has been extensively investigated,[119, 288, 289, 326-334] a number of fundamental questions about how ATP binding and hydrolysis controls the GroEL functional cycle remain unresolved.

A particular limitation for addressing many of the issues is the complexity of the GroEL-ATP system. There are minimally 14 potential states of ATP-bound GroEL. At the same time, ATP binding to the GroEL tetradecamer is known to induce structural changes in the tertiary structure of the GroEL subunits while simultaneously rearranging the quaternary structure of the oligomer.[119, 329] It has been shown via X-ray crystallography and cryo-EM that the binding of ATP by GroEL induces an extension and twisting of the apical domain[333] and a small "rocking" of the equatorial domain.[320, 329] The binding of ATP by GroEL is also influenced by the presence of small ions (*e.g.*, Mg^{2+} and K^{+}). Mg^{2+} is necessary for the binding of ATP and K^{+} is thought to activate the ATPase activity of GroEL.[335] It has also been proposed that NH_4^{+} ions can act as a surrogate for K^{+} ions.[336-338] These nucleotide-driven structural rearrangements interact to create a complex and layered set of allosteric transitions that govern the GroEL protein folding cycle. This ligand binding and structural complexity constrains the detail that can be robustly extracted from ensemble thermodynamic studies.

Recently, we reported results using native mass spectrometry (nMS) that reveal new insights about GroEL oligomer stability and the stoichiometry of GroEL-ATP/GroES interactions.[11] Using variable-temperature electrospray ionization (vT-ESI) we found that GroEL-ATP binding was temperature and ATP-concentration dependent, suggesting that more detailed thermodynamic analysis might reveal new insights into how the GroEL nanomachine operates. Here we report the thermodynamic measurements (ΔH, ΔS, and ΔG) of ATP and ADP binding to GroEL utilizing nMS with vT-ESI, along with studies that observe how endogenous ions affect the GroEL-ATP binding interaction. We

demonstrate that this approach can extract rigorous thermodynamic measurements for step-wise binding of ATP to a GroEL tetradecamer. We further show that EEC plays a central role in the binding of ATP to a GroEL ring, with important mechanistic implication for how GroEL functions. These results thus lay the groundwork for the development of new strategies for detailed thermodynamic analysis of other complex, multi-dentate biomolecular systems. The ability to measure and understand the underlying thermodynamics of protein-cofactor, protein-ligand and protein-protein interactions has been the focus of much research particularly in drug discovery efforts.[339, 340]

5.3. Results and Discussion

5.3.1. Thermodynamics of GroEL-ATP$_n$ binding in ethylenediammonium diacetate (EDDA) buffer

Figure 5.1A contains deconvoluted mass spectra obtained for solutions of GroEL containing magnesium acetate and EDDA taken at temperatures of 5 °C, 23 °C, and 41 °C, and panel 1B shows the intrinsic equilibrium constants (K_a) for each GroEL-ATP binding reaction. The intrinsic binding constants are statistically corrected to account for the number of modes in which ligands may associate or dissociate from the complex based on the distribution of available monomers (see methods).[315, 316] It is interesting to note that the binding of up to GroEL-ATP$_{14}$ is only observed at lower temperatures for 25 μM ATP and that binding affinity is decreased at higher temperatures. The deconvoluted mass spectra also reveal potential cooperativity in binding at lower temperatures, *e.g.*, note the increase in the abundance of GroEL-ATP$_{14}$ at 5 °C. The association constants represent

the sequential binding of ATP to GroEL. The K_a values vary significantly with solution temperature with binding of ATP being favored for each reaction at 5 °C compared to 41 °C, except for GroEL-ATP_{13}. Most pronounced of all the constants, however, is GroEL-ATP_{14} where the temperature dependance is most easily observed. A similar effect for the GroEL-ATP_{14} K_a value was observed by Sharon et al., albeit their study was only conducted at room temperature.[2] A depression in the GroEL-$ATP_{8\text{-}13}$ K_a values are hallmark of negative inter-ring cooperativity and is most apparent at low solution temperatures.

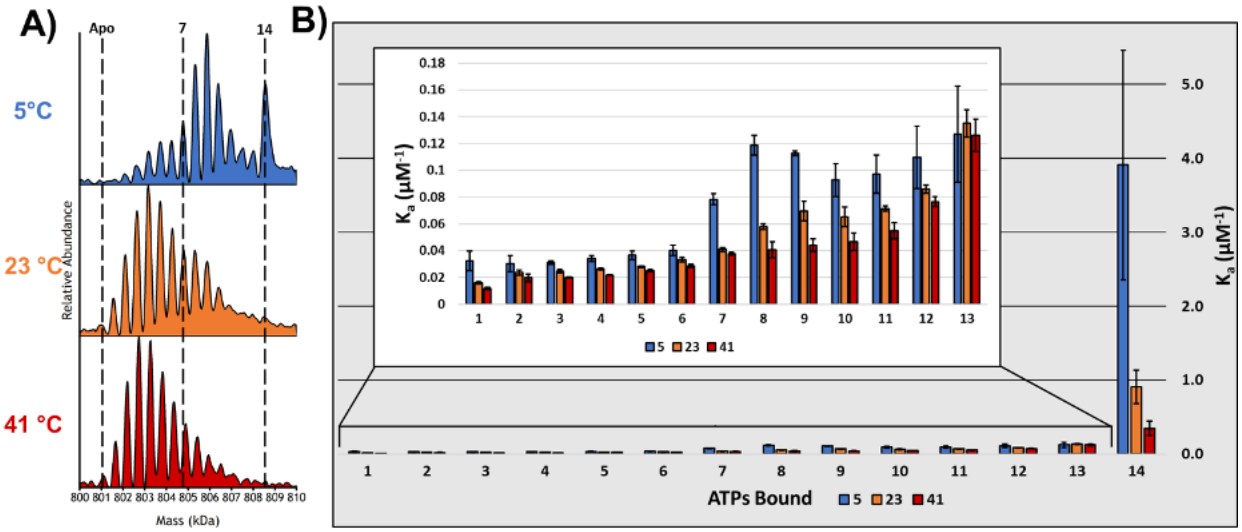

Figure 5.1 A) Deconvoluted mass spectra of 500 nM GroEL in a solution of 200 mM EDDA, 1 mM $MgAc_2$, and 25 µM ATP at 3 different temperatures. Binding affinity diminishes as solution temperature is increased. Bimodality in the ATP binding distributions is likely to be a consequence of negative cooperativity between the *cis* and *trans* rings. B) This bar charts shows the intrinsic K_a values calculated for the 14 ATP binding reactions for GroEL at 3 different temperatures 5 °C, 23 °C, and 41 °C. The inset shows a bar chart that expands the first 13 binding reactions so that details may be more observed easily. Binding affinity is temperature dependent and colder solution temperatures enhance the effect of inter-ring negative cooperativity, as the affinity for ATP decreases more substantially when binding in the *trans* ring begins.

Deconvoluted MS data shown in **Figure 5.2A** display the concentration-dependent trend of ATP binding at 25 °C for 10, 25, and 50 µM ATP in EDDA. From the K_a values, Van't Hoff analysis was used to calculate the thermodynamic constants associated with each binding reaction. **Figure 5.2B** and **C** show enthalpy, entropy, and Gibbs free energy values at 25 °C. Low temperature Gibbs free energy values show the most diverse pattern in which binding of ATP becomes more favored until GroEL-$ATP_{8\text{-}9}$ (**Figure 5.5**). The ΔG terms increase slightly with each additional ATP bound before becoming disproportionately favored for GroEL-ATP_{14}. As the solution temperature increases, the

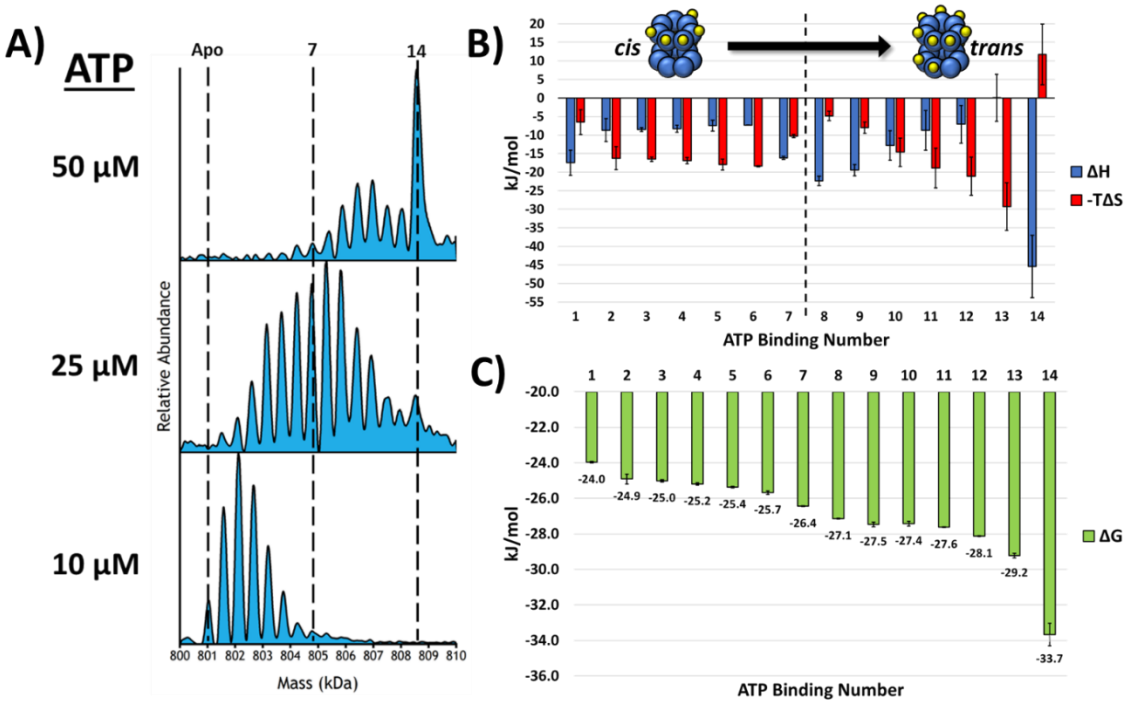

Figure 5.2 A) Stacked deconvoluted spectra showing the increased binding observed as the concentration of ATP is increased B) Bar chart showing the ΔH and -TΔS contributions at 25 °C for each of the ATP binding reactions. The cis ring binding reactions are mostly entropy-driven while the transition to the trans ring is driven enthalpically. The GroEL-ATP_{14} binding reaction is the most enthalpically favored and the least entropically favored which indicates that the structure of GroEL is becoming more rigid upon binding of GroEL-ATP_{14}. C) The overall Gibbs free energy associated with each of the 14 ATP binding reactions. All error bars are the standard deviation of 3 replicates.

variations in the ΔG values diminish. ΔΔG values for 41 °C – 5 °C in **Figure 5.6** reveal that binding for the *cis* ring (GroEL-ATP_{1-7}) becomes more favored as the temperature is increased when compared to the initial (GroEL-ATP_{8-10}) ATP binding reactions of the *trans* ring.

Binding of ATP by GroEL in EDDA is largely driven by entropy as shown in **Figure 5.2B**. EEC is observed for ATP binding and explains the comparative lack of ΔG fluctuation across the range of ATP binding reactions. With the exception of the first and last ATP binding reactions, binding of ATP to the *cis* ring of GroEL is largely entropically driven and is indicative of the structural rearrangement. The contributions of enthalpy and entropy begin to switch with binding of GroEL-ATP_{7-10}, which coincides with the filling of the *cis* ring and beginning of binding to the *trans* ring. These values switch again for GroEL-ATP_{11-13} and yet again for GroEL-ATP_{14}. The binding of the ATP_{14} is the only binding reaction with any amount of unfavorable entropy. This seems to indicate that the final structural rearrangement in the *trans* ring is very ordered compared to preceding binding reactions (GroEL-ATP_{11-13}) and is very favored enthalpically which explains its highly favorable ΔG value.

5.3.2. Thermodynamics of GroEL-ADP_n binding in ammonium acetate (AmAc) buffer

Subsequent thermodynamic studies attempted to quantify GroEL-ATP binding thermodynamics in AmAc and showed that the nucleotides observed binding to the GroEL complex were ADP and not ATP, suggesting that a substantial level of hydrolysis occurs

under these conditions. Excess NH_4^+ ions allow for rapid ATP hydrolysis turnover in GroEL, thus not allowing the determination of GroEL-ATP binding equilibrium constants. As a result, the data were used to quantify the thermodynamic contributions of GroEL-ADP binding in comparison to GroEL-ATP binding in EDDA solution conditions. **Figure 5.3A** shows the ADP concentration-dependent binding of GroEL post-hydrolysis. When compared to **Figure 5.2A**, it is clear that GroEL binds fewer ADP molecules than ATP

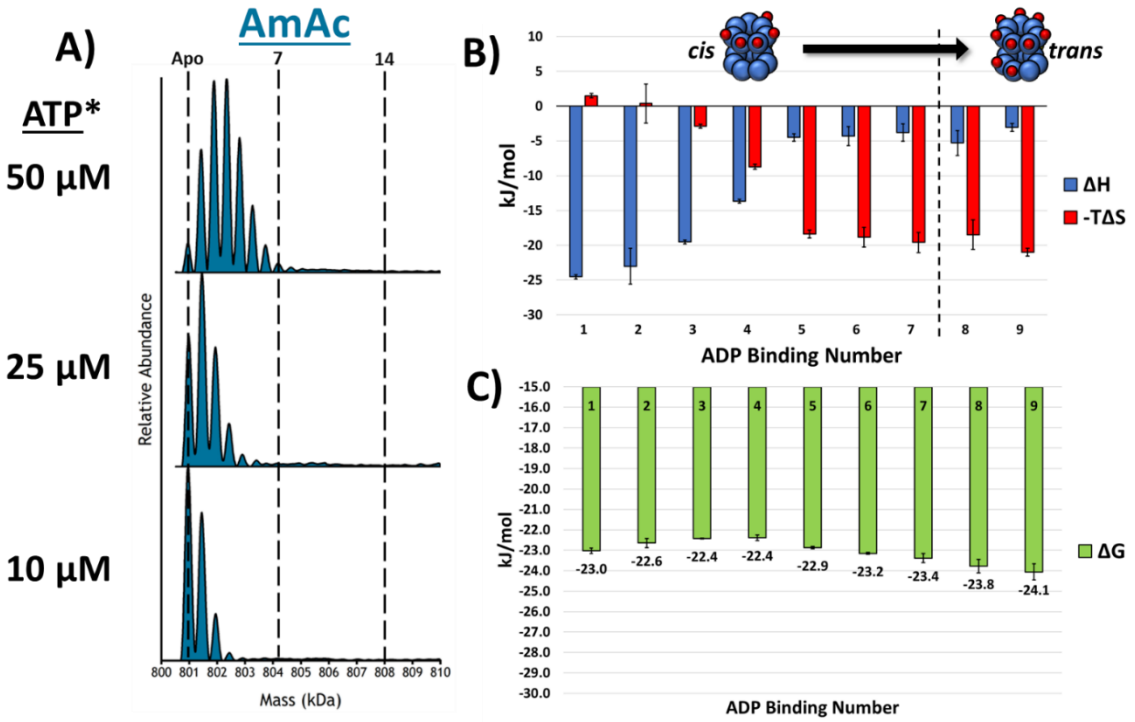

Figure 5.3 A) These stacked deconvoluted spectra show that as ADP concentration is increased the binding of ADP is does not show any cooperativity. B) Bar chart showing the ΔH and -TΔS contributions at 25 °C for each of the ADP binding reactions. The enthalpy and entropy show a singular transition from GroEL-$ADP_{4\text{-}5}$and are overall much less dynamic than the binding of ATP in EDDA. C) This bar chart displays the Gibbs free energy measurements for the ADP binding reactions at 25 °C. EEC is more heavily present in the ADP data set as the Gibbs free energy varies by less than 2 kJ/mol. All error bars are the standard deviation of at least 3 replicates. *(**Note**: ATP was added to the solution but only ADP binding was observed.)

(in EDDA), and signs of cooperative binding of ADP remain absent. **Figures 5.3B** and **C** show the thermodynamic constants for GroEL-ADP_n at 25 °C; the thermodynamic constants were only calculated up to GroEL-ADP_9 due to poor fits for the Van't Hoff plots for GroEL-ADP_{10-14}. The enthalpy and entropy terms switch at GroEL-ADP_{4-5} displaying EEC, which causes the Gibbs free energy terms to vary only slightly. The comparison of Gibbs free energy values between ADP and ATP binding also demonstrates that ADP binds more weakly than ATP in EDDA. In EDDA the ΔG for the binding of ATP at 25 °C is about 2-3 kJ/mol more favorable than in ADP binding in AmAc conditions.

As shown in **Figure 5.1**, the ATP binding affinity of GroEL in EDDA is temperature dependent, and changes in the ΔG values for the *cis* ring binding reactions is of greater magnitude than for several of those in the *trans* ring (**Figure 5.6**). The initial ATP binding to the *cis* ring is more favorable compared to the *trans* ring binding reactions, which are more allosterically disfavored as evidenced by subtle differences in symmetry between the rings observed in ATP-bound cryo-EM structures.[326] A potential structural explanation concerns the inter-ring hydrophobic contacts in the region of A109 on helix D that are extensively perturbed by the binding of ATP in the binding pocket of the equatorial domain.[114, 331] The disturbance of these contacts is theorized to be responsible for inter-ring negative cooperativity upon the binding of ATP.[320, 331, 341] At higher temperatures increased dynamics in this region would only serve to further weaken this contact, that would in turn increase the prevalence of the negatively cooperative mechanism.

As mentioned before, the existence of EEC contributes to the small fluctuations in ΔG as more ATP is bound to GroEL. EEC is a phenomenon that as ΔH or TΔS varies the other tends to compensate in an opposite direction (see **Figures 5.2C**, **5.3C**, and **5.9**); this effect has been observed in thermodynamic measurements of other interactions. The entropy term encompasses not only the conformational entropy of the structures but also the entropy of the solvent;[109] the enthalpy term is subject to the same contributions of structure and solvent.[106, 342] For example, in the GroEL system binding of ATP leads to extension of the apical domain and release of confined water, both of which are entropically favorable.[318-320] However, a more extended, labile apical domain obviates a loss of favorable binding contacts (Van der Waals, H-bonding, and salt bridging) which would be enthalpically less favorable. The resultant ΔH value for that interaction would be increased and -TΔS would "compensate" by decreasing, *i.e.*, become more favorable.

The data contained in **Figure 5.2B** reveal that ATP binding in the formation of GroEL-$ATP_{1\text{-}7}$ is largely driven by entropy. The entropy is thought to arise from rotation of the "hinge" region of the intermediate domain and extension of the apical domain initiated by loss of salt bridge contacts (E255-K207 and R197-E386) that connect adjacent apical domains in the subunits of the apo-GroEL.[320, 329] The enthalpy and entropy terms for binding GroEL-$ATP_{7\text{-}10}$ switch and the binding becomes mostly enthalpically driven. EEC is expected owing to negative cooperativity associated with inter-ring communication accompanying GroEL-ATP binding. Saibil et al. report that upon ATP binding to the *cis* ring of GroEL the equatorial domain shifts slightly which causes loss of

a key hydrophobic contacts.[320, 331] The loss of these contacts is thought to be the structural progenitor of the inter-ring negative cooperativity and may explain why entropy and the overall Gibbs free energy favorability is decreased for the initial ATP binding reactions of the *trans* ring (**Figures 5.2B, 5.5,** and **5.6**). Entropy then dominates for the formation of GroEL-$ATP_{11\text{-}13}$, which is most likely associated with similar structural changes seen in the *cis* ring. This explanation is consistent with observations made by Chapman et al., specifically increased binding affinity when up to 3 ATP molecules are bound to a ring.[330] The GroEL-ATP_{14} binding reaction coincides with the most favorable binding and is the only binding reaction that has an associated negative entropy. The GroEL-ATP_{14} binding reaction is largely enthalpically favorable because the restructuring of the complexe occurs during the formation of GroEL-$ATP_{10\text{-}13}$ making GroEL-ATP_{14} more enthalpically favored.

The data in **Figure 5.1A** show that as solution temperature is increased, the binding affinity for ATP diminishes. It is interesting to note the behavior of the profile for the deconvoluted spectra; at colder solution temperatures, there exists a bimodality to the bound ATP distribution. The two distributions coincide with the filling of each ring of GroEL. Horovitz et al. demonstrated that the binding of ATP to GroEL can be explained through a nested-cooperativity model where each ring binds concertedly (Monod-Wyman-Changeux (MWC)) and the behavior between the rings is coupled sequentially (Koshland-Nemethy-Filmer (KNF)).[121] Binding of GroEL-ATP_{14} observed in the MS data can be interpreted as a highly cooperative reaction as the relative intensity of the GroEL-ATP_{14} signal is largely disproportionate compared to the preceding distribution of signals

(GroEL-ATP_{8-13}). As the *trans* ring begins to bind several ATP molecules (GroEL-ATP_{8-10}) the cooperative effect allosterically begins to favor binding of a full ring. At higher temperatures much of this cooperative signature is lost as binding of ATP to the *cis* ring becomes favored.

Another interesting point that has arisen during our thermodynamic studies is the clear differences observed in the thermodynamic signatures for the *cis* and *trans* rings of GroEL. The *cis* ring ATP binding is entropically favored whereas the *trans* ring ATP binding is much more diverse in its thermodynamic contributions. The binding of GroEL-ATP_{1-7} is entropy favored owing to the large conformational change in the apical domains, while the initial ATP binding reactions (GroEL-ATP_{8-10}) in the *trans* ring are disfavored entropically; however, following binding of up to 3 ATP molecules to the *trans* ring the entropy and enthalpy switch for the subsequent binding reactions up to GroEL-ATP_{13}.

The concerted (MWC) model of ligand binding postulates that the binding of one ligand to a protomer (subunit) induces changes in affinity for all the other protomers collectively into a relaxed or tense state.[125] In contrast, the sequential (KNF) model argues that the binding of a ligand to a subunit will only have immediate effect (positive or negative) on its neighboring subunits.[127] The thermodynamic signature for the GroEL-ATP_1 binding reaction shows that it is enthalpically driven but the GroEL-ATP_{2-6} binding reactions are driven entropically and have entropic values that are relatively unchanging. This thermodynamic pattern in conjunction with the mass spectral data suggest that binding in the *cis* ring is largely sequential in the EDDA solution. The GroEL-ATP_1 reaction sets into effect a “chain reaction” that affects adjacent subunits via allosteric

transitions. If the binding were purely concerted, then the binding distribution should be like that seen in the *trans* ring where once 2 or 3 ATP molecules are bound then the distributions heavily shift to the filled state (GroEL-ATP_{14}). These observations may be due to the difference in solution conditions used when comparing to solution-phase experiments. In these thermodynamic experiments there is no added K^+ or GroES which will ultimately change the affinity for ATP and conformation of GroEL. However, the observations made by the authors do support similar effects reported by previous investigators; specifically, the observation of cooperative binding of ATP that is non-stochastic.[115, 121, 319, 343] Therefore, it is possible that the binding of ATP to GroEL is still governed via a nested-cooperativity model, but that the *cis* ring binding is governed sequentially, *trans* ring binding is concerted, and inter-ring communication is sequential but is negatively cooperative.

Thermodynamic data for the binding of ADP in AmAc reveal distinct differences between the two nucleotides when compared to the EDDA/ATP data. The presence of EEC at 25 °C causes the ΔG values in **Figures 5.2C** and **5.3C** to remain relatively constant. However, the underlying ΔH and TΔS values show a stark mechanistic difference between the two interactions. Initial binding reactions (GroEL-ADP_{1-4}) for ADP-binding are driven enthalpically and not until GroEL-ADP_5 does entropy become dominant. In the EDDA/ATP data, entropy becomes dominant much sooner (GroEL-ADP_2) and several switching transitions occur as a function of sequential ATP binding. The lack of various switching reactions in the AmAc/ADP data confers an overall lack of cooperative binding of ADP; this conclusion is strengthened by the nMS data showing

gaussian distribution for ADP binding at all observed ADP concentrations and by studies conducted by other researchers observing lower affinities associated with the binding of ADP.[289, 344] It has been shown that binding of ADP can cause conformational shifts in GroEL,[301, 345] which are corroborated possibly by the entropic domination seen for GroEL-ADP_{5-9}. However, these entropic shifts do not seem to be resultant from an allosteric transition[346] that leads to increased affinity for further ligation reactions.

5.3.3. Effects of ions on GroEL-ATP binding

An essential ligand in the function of GroEL is the K^+ ion. However, it has been reported that NH_4^+ ions can act as substitutes for K^+ ions and activate ATPase activity of GroEL. To test this effect, ATP was added to GroEL solutions in AmAc and EDDA buffers. Observed mass shifts in AmAc experiments show that GroEL hydrolyzes most of the ATP in solution and that only signals corresponding to GroEL-ADP_n are observed (mass shifts of 460 Da corresponding closely to [Mg^{2+} + ADP]). When compared to experiments conducted in EDDA buffer it is clear that ATPase activity in GroEL is observed in the presence of NH_4^+ (**Figure 5.4**). To verify the presence of GroEL-driven ATP hydrolysis in AmAc, a hydrolysis deficient mutant of GroEL (D398A) was introduced into the same solution composition and was found to bind only [Mg^{2+} + ATP] pairs (**Figure 5.4**). Another experiment conducted with wtGroEL in AmAc conditions revealed that the binding distribution of ADP was identical regardless of whether ADP or ATP was initially added to the solution (**Figure 5.7**).

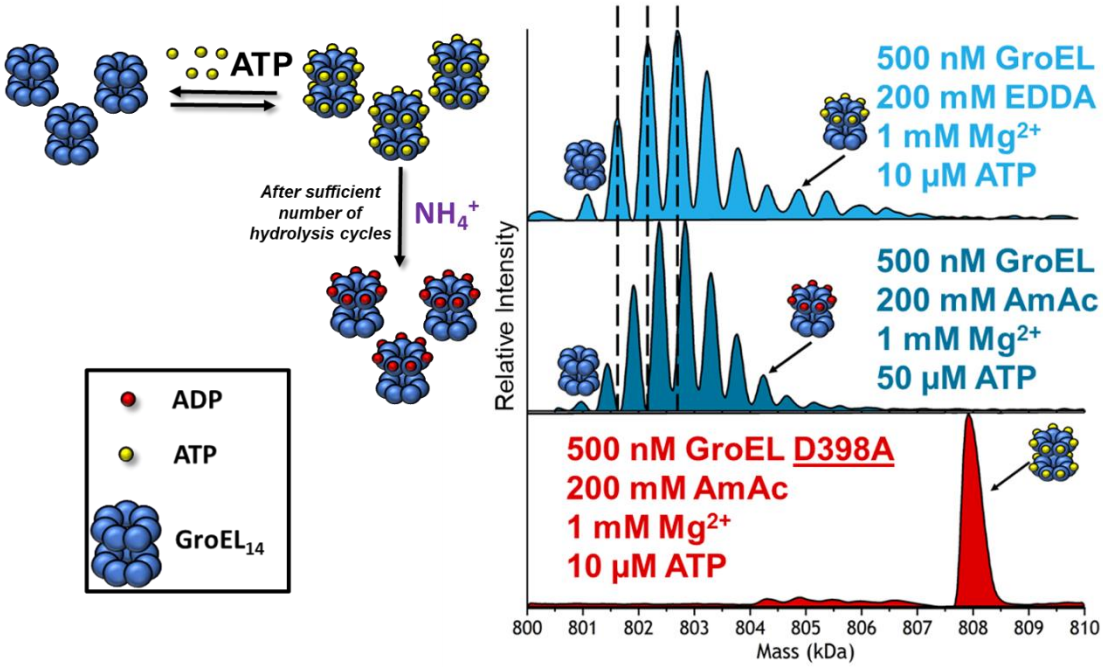

Figure 5.4 Stacked spectra showing the difference in mass shifts observed for nucleotide binding observed in EDDA and AmAc solutions. Black lines are used to aid the viewer and show that the mass shifts for EDDA are assigned to $[ATP + Mg^{2+}]_n$ while the mass shifts for AmAc conditions are assigned to $[ADP + Mg^{2+}]_n$. A hydrolysis deficient mutant (D398A) was also analyzed in an AmAc solution (red) which shows the elevated level of cooperative binding in the presence of NH_4^+ ions and the absence of hydrolysis. Also note for the D398A mutant that the affinity of GroEL for ATP is drastically increased in AmAc compared to EDDA conditions.

Co-solutes can contribute extensively to the chemical potential landscape available to biomolecules in solution. In the case of GroEL-ATP binding, Mg^{2+} and K^+ ions are vital to GroEL function. Mg^{2+} ions are essential for the binding of ATP to proteins and K^+ ions have been known as strong activators of ATPase activity. In previous work we have shown that the Mg^{2+} concentration impacts the stoichiometry of GroES binding to GroEL[11] (also see **Figure 5.8**), which illustrates the importance of Mg^{2+} concentration for proper functioning of the GroEL nanomachine. Lorimer et al. have shown that K^+ ions are necessary for the modulation of the ATPase mechanism of GroEL.[124, 347, 348] It is

interesting to note that other researchers have also reported that NH_4^+ and other monovalent cations can act as K^+ ion surrogates.[335, 336] For the GroEL-ATP_n thermodynamics data, the "traditional" nMS buffer of AmAc was avoided due to the potential for ATP hydrolysis. The data in **Figure 5.4** show that in EDDA, GroEL is unable to hydrolyze any measurable amount of ATP. Conversely, in AmAc, GroEL is able to initiate turnover of ATP and hydrolyze it to form ADP. The consequence of this reaction in 200 mM AmAc buffer is that ATP to GroEL binding is not observed; only ADP binding is observed. The rate of ATP hydrolysis in AmAc is fast compared to the time scale of loading the sample and the start of data acquisition (~5 min). Even in experiments with ratios of 500:1 ATP:$GroEL_{14}$, GroEL was able to hydrolyze enough ATP to the point where the nucleotide binding patterns were indistinguishable from experiments in which ADP was added initially (**Figure 5.7**). These observations are in agreement with hydrolysis rates obtained in previous GroEL-ATP hydrolysis studies.[347, 349] In the absence of hydrolysis (D398A GroEL, **Figure 5.4**), the affinity of GroEL for ATP and the cooperativity of ATP binding are enhanced more so than in EDDA buffer, which lacks NH_4^+ ions. The observation of elevated cooperative binding may indicate that small ions (NH_4^+ and K^+) are allosteric ligands for GroEL ATPase functionality. Heavy metal replacement strategies in X-ray crystallographic structures have shown 3 potential binding sites for monovalent cations for each GroEL subunit.[336]

5.4. Conclusion

Variables such as solution temperature, pressure, and concentration influence changes in the "native" structure of biomolecules through manipulation of fundamental thermodynamic contributions (ΔH, ΔS, and ΔG). Using vT-nESI we were able to conduct thermodynamic measurements of ATP and ADP binding for the sequential binding of both nucleotides. The thermodynamic data show complex patterns of enthalpy-entropy compensation (EEC) for binding of ATP; such EEC patterns are somewhat lessened for the binding of ADP. In EDDA there also are different thermodynamic mechanisms of ATP binding for the *cis* and *trans* rings as the thermodynamic trends for the formation of GroEL-ATP_{1-7} are distinctly different from GroEL-ATP_{8-14}. This agrees with previous findings from other researchers that propose a nested cooperativity mechanism for ATP binding. The *m/z* dispersion afforded by using MS allows for the analysis of individual binding reactions which are otherwise not observable using solution-based methods. This level of sensitivity and specificity provides a compelling case for nMS thermodynamic analysis of other systems.

Here, we also describe the effects of solution composition for the binding of ATP to GroEL. Mg^{2+} concentration, presence of NH_4^+ ions, and solution temperature were all shown to be relevant factors that affect the GroEL-ATP interaction. The MS data support the existence of significant cooperative binding of ATP in EDDA solutions, which is enhanced further in AmAc solutions for hydrolysis deficient GroEL (D398A). The synergistic effects of monovalent cations in binding of ATP and ATPase activity in GroEL

remain an interesting aspect that necessitates further study to elucidate their role in the manipulating the free energy landscape available to chaperonin complexes.

5.5. Methods

5.5.1. Sample Preparation

GroEL tetradecamer and D398A GroEL tetradecamer were expressed and purified by the Rye research lab at the Texas A&M Department of Biochemistry and Biophysics. Aliquots of the GroEL samples were stored at -80 °C in a Tris buffer. Aliquots were buffer-exchanged into ammonium acetate (AmAc) or ethylenediamonium diacetate (EDDA) (obtained from Sigma-Aldrich) using BioRad biospin P-6 size exclusion (6000 Da cutoff) columns to remove unwanted salt contamination. Magnesium acetate ($MgAc_2$) and Na-ATP were obtained from Sigma-Aldrich and fresh solutions were prepared prior to each experiment.

5.5.2. Experimental

Data was collected on a Thermo Q Exactive UHMR (ultra-high mass range) mass spectrometer. Constituents for each sample were mixed immediately prior to analysis. For the thermodynamic analysis of GroEL-ATP binding solution conditions were: 1 mM $MgAc_2$, 200 mM EDDA, 500 nM GroEL (14mer), and varying concentrations of ATP. The vT-nESI device was used to modulate the temperature of the solution; more information pertaining to operation of the device can be found in previous work.[13] Solution temperatures used for this study were 5 °C to 41 °C; above 41 °C degradation

products of the GroEL complex begin to become observable. The resolution setting was maintained at 25000, with 5 microscans, and injection time of 200 ms, capillary temperature was 150 °C, trap gas pressure was set to 7.0 (N_2), desolvation voltage (in-source trapping)[46] was set to -200 V, and HCD energy was set to 200 V (the latter two energy parameters only apply to EDDA buffer conditions). Under these conditions the ATP-bound states of GroEL were nearly baseline-resolved in most circumstances (**Figures 5.11** and **5.13**). Thirteen solution temperatures, every 3 °C from 5 °C to 41 °C at 8 ATP concentrations (0, 1, 5, 10, 15, 25, 35, and 50 μM ATP) were analyzed in $n = 3$ trials. Each trial entailed the preparation of new solutions for buffers, GroEL, $MgAc_2$, and ATP solutions.

5.5.3. Data Processing

Each spectrum was deconvoluted using UniDec[232] and incorporated the 4 most abundant ATP distributions (see **Table 5.1** in supporting information for assignment statistics). Baseline reduction was avoided in the UniDec software as to not bias the data. The area of each peak to be integrated was determined by extrapolating the local minimum between peaks down to baseline to serve as the limit of integration. The resulting relative abundances were used in a sequential binding model (**Figure 5.10**) to fit K_d (dissociation constant) values.[8, 350] The reciprocal of the K_d yields the K_a; the natural logs of the K_a values were plotted against inverse temperature (in K) for Van't Hoff analysis (**Figures 5.12** and **5.14**). The slope of the fit line is used to calculate ΔH and the y-intercept is used to calculate ΔS in accordance with the **Equation 5-1**.

Equation 5-1

$$\ln(K_a) = -\frac{\Delta H}{RT} + \frac{\Delta S}{R}$$

Using **Equation 5-2** the Gibbs free energy terms were calculated in units of $\frac{kJ}{mol}$.

Equation 5-2

$$\Delta G = \Delta H - T\Delta S$$

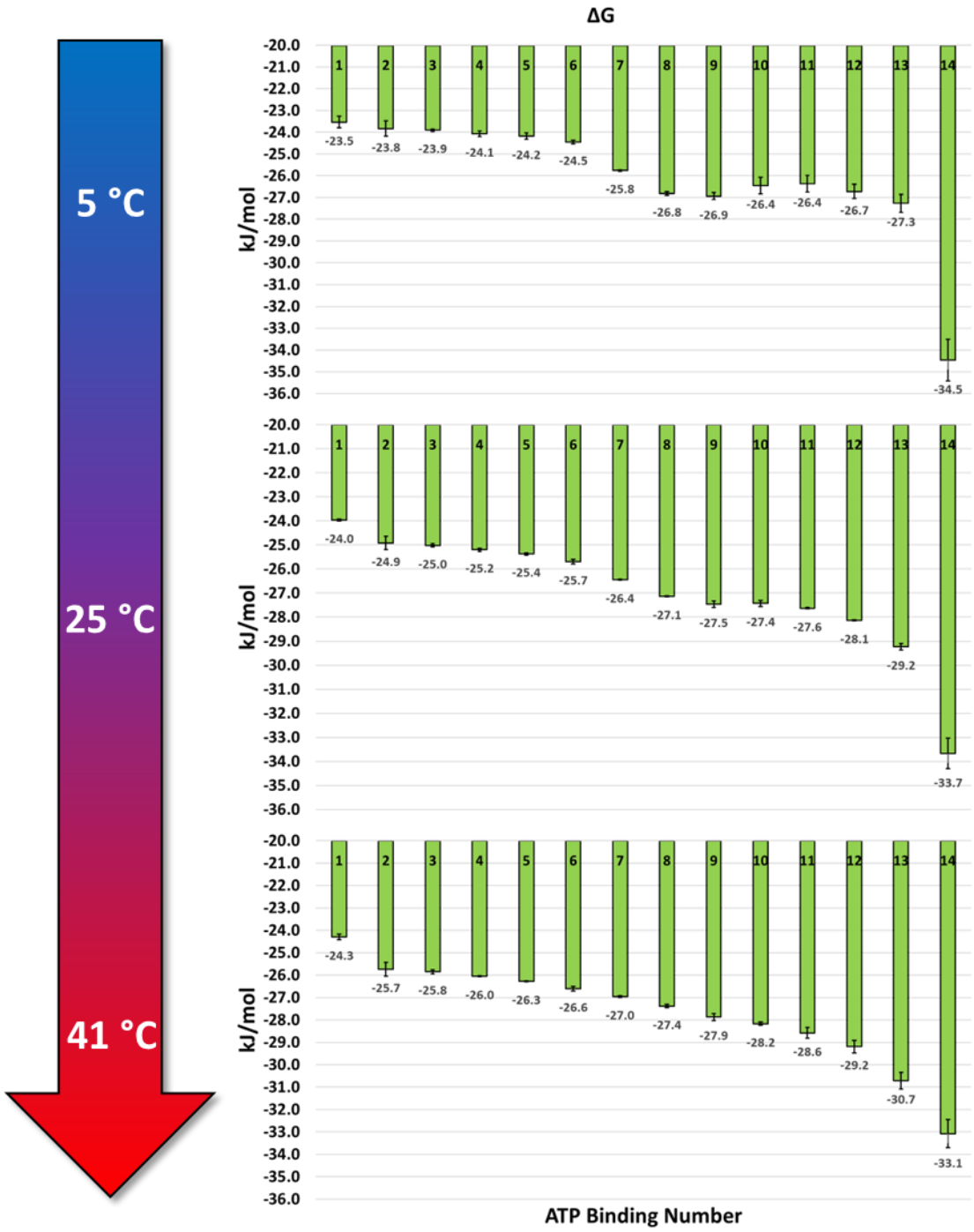

Figure 5.5 Stacked plots displaying the changes in ΔG at various temperatures. As the solution temperature increases, the bimodality observed for the sequential ATP binding becomes diminished.

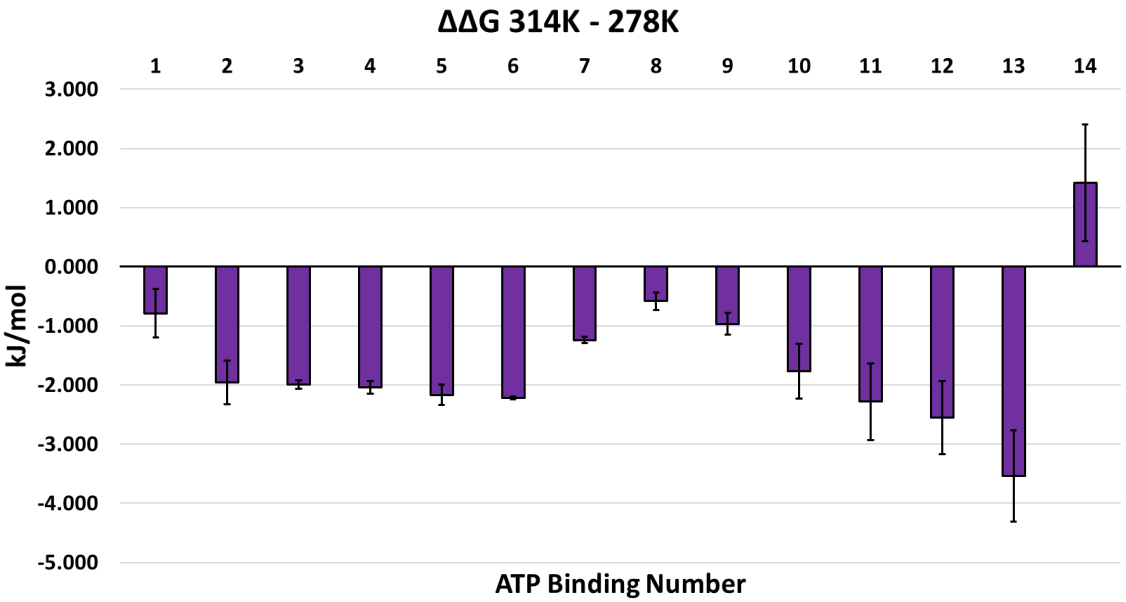

Figure 5.6 This bar chart shows the difference in ΔG from 5 °C to 41 °C. The relative increase in the early binding reactions may explain why binding of ATP becomes less favored at higher temperatures as cis ring binding becomes more favored compared to trans ring binding.

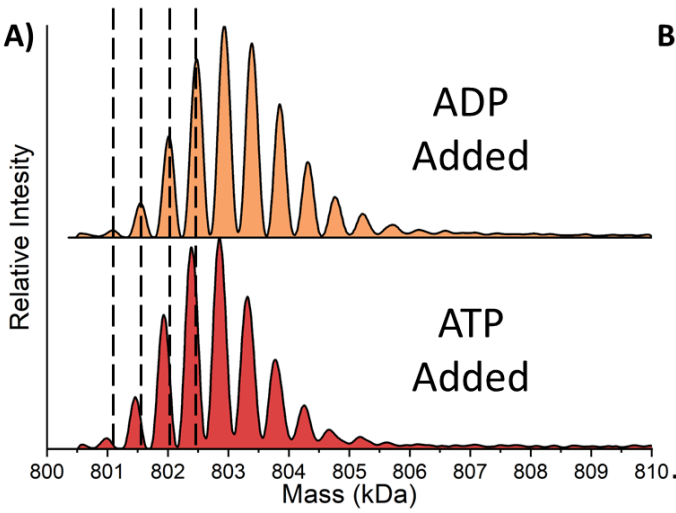

B)

	ATP Added		ADP Added	
	Mass (Da)	ΔMass (Da)	Mass (Da)	ΔMass (Da)
Apo	800969		801086	
1	801439	470	801545	459
2	801908	469	802012	467
3	802364	456	802472	460
4	802830	466	802932	460
5	803295	465	803386	454
6	803754	459	803846	460
7	804233	479	804309	463
8	804648	415	804757	448
9	805148	500	805213	456
10	805603	455	805709	496
11			806143	434
12			806590	447
Average		**463.4**		**458.7**

Figure 5.7 A) Stacked deconvoluted mass spectra showing the similarities in the binding distributions when either ADP is directly added to a solution containing GroEL, or ATP is added under conditions where hydrolysis occurs. Solution conditions are 500 nM GroEL, 50μM ATP or ADP, 1mM $MgAc_2$, and 200 mM AmAc at 25 °C. B) Table containing the peak centroid data for A. Mass shift values are in the form $\Delta\boldsymbol{Mass} = (\boldsymbol{n}+\mathbf{1}) - \boldsymbol{n}$. Note: measured mass of apo complex for ATP vs ADP is shifted by about 120 Da explaining why subsequent peaks are not exactly aligned in panel A.

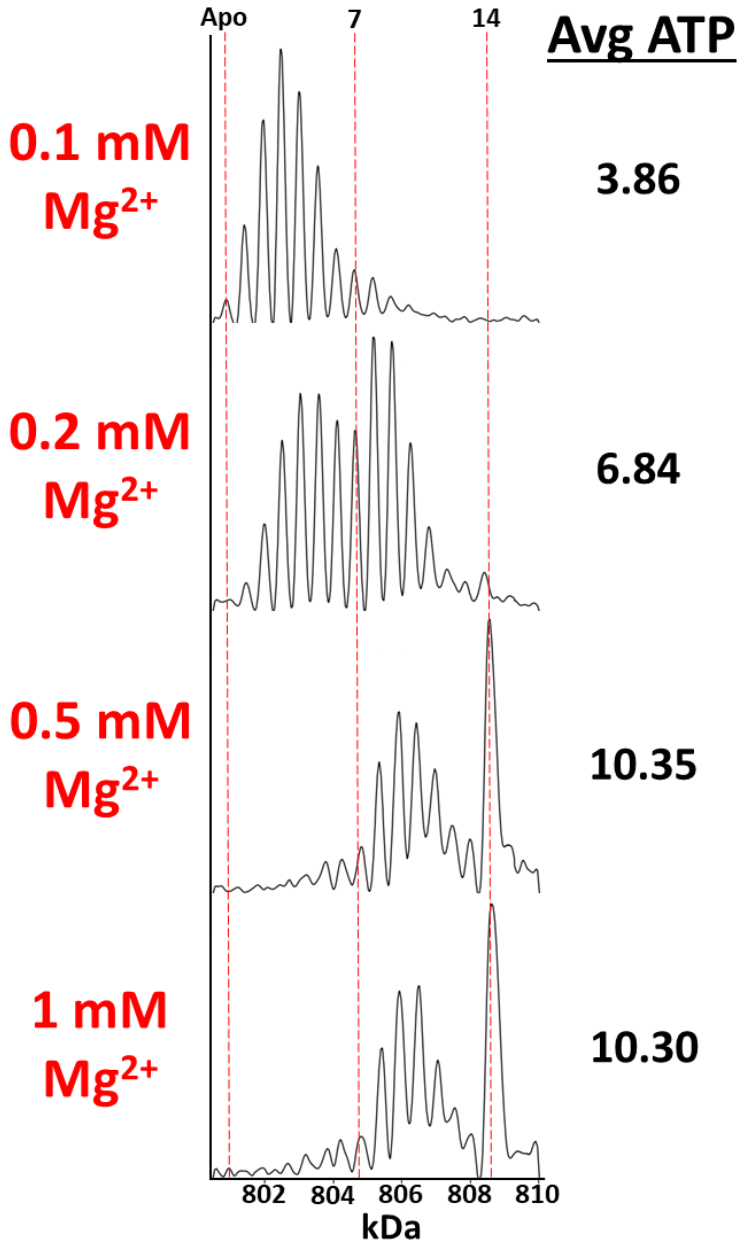

Figure 5.8 Deconvoluted mass spectra of 500 nM GroEL in a solution of 200 mM EDDA and 25 µM ATP at 5 °C at varying Mg^{2+} concentrations. These stacked spectra show how the binding of ATP can be heavily dependent on the Mg^{2+} concentration. Average ATP is a weighted average of the total ATP molecules bound to GroEL. The increase in affinity for ATP begins to level off at 0.5 mM Mg^{2+}.

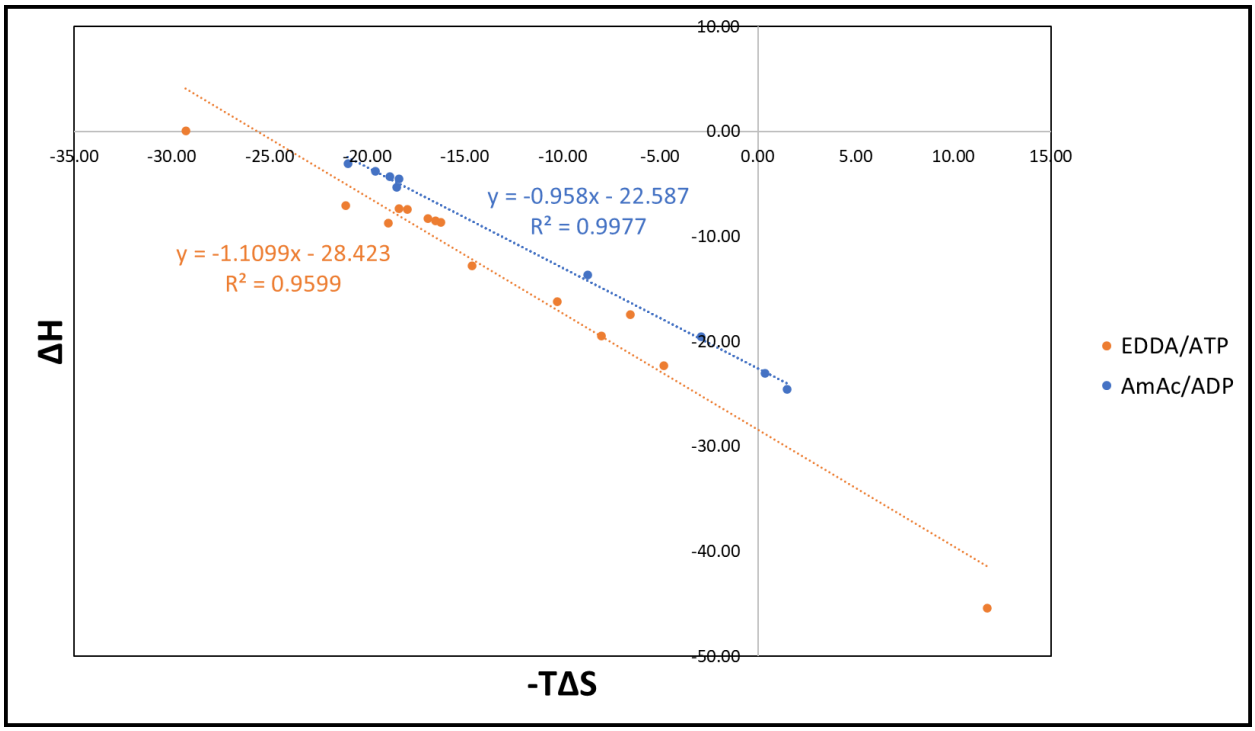

Figure 5.9 This plot is intended to show the EEC of entropy and enthalpy for GroEL-ATP binding in EDDA and GroEL-ADP binding in AmAc. The slope of the fit line being close to unity is a measure of the level of EEC where perfect EEC would be m = 1 (where m is the slope of the line).

Table 5.1 Average mass shift and error associated with the assignment of each [ATP + Mg^{2+}] (theoretical mass is ~531 Da) binding.

ATP #	Average Mass Shift (Da)	Standard Deviation (±Da)	% Error
1	548.6	18.4	3.31%
2	551.5	20.0	3.87%
3	536.5	3.9	1.04%
4	538.7	2.4	1.44%
5	539.7	16.0	1.63%
6	522.5	26.6	1.61%
7	531.4	6.6	0.07%
8	539.9	14.5	1.67%
9	542.4	3.0	2.15%
10	539.1	8.0	1.53%
11	519.1	26.4	2.25%
12	523.7	8.3	1.37%
13	527.4	6.9	0.67%
14	551.6	17.6	3.89%

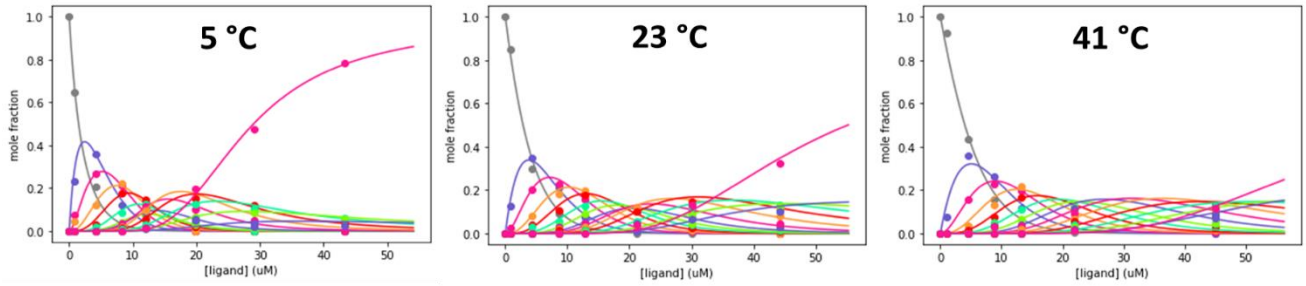

Figure 5.10 These mole fraction vs ATP concentration plots are used to calculate the K_a values. Three temperatures are shown and the n=14 binding event (pink line) is shown to decrease in relative abundance as temperature is increased.

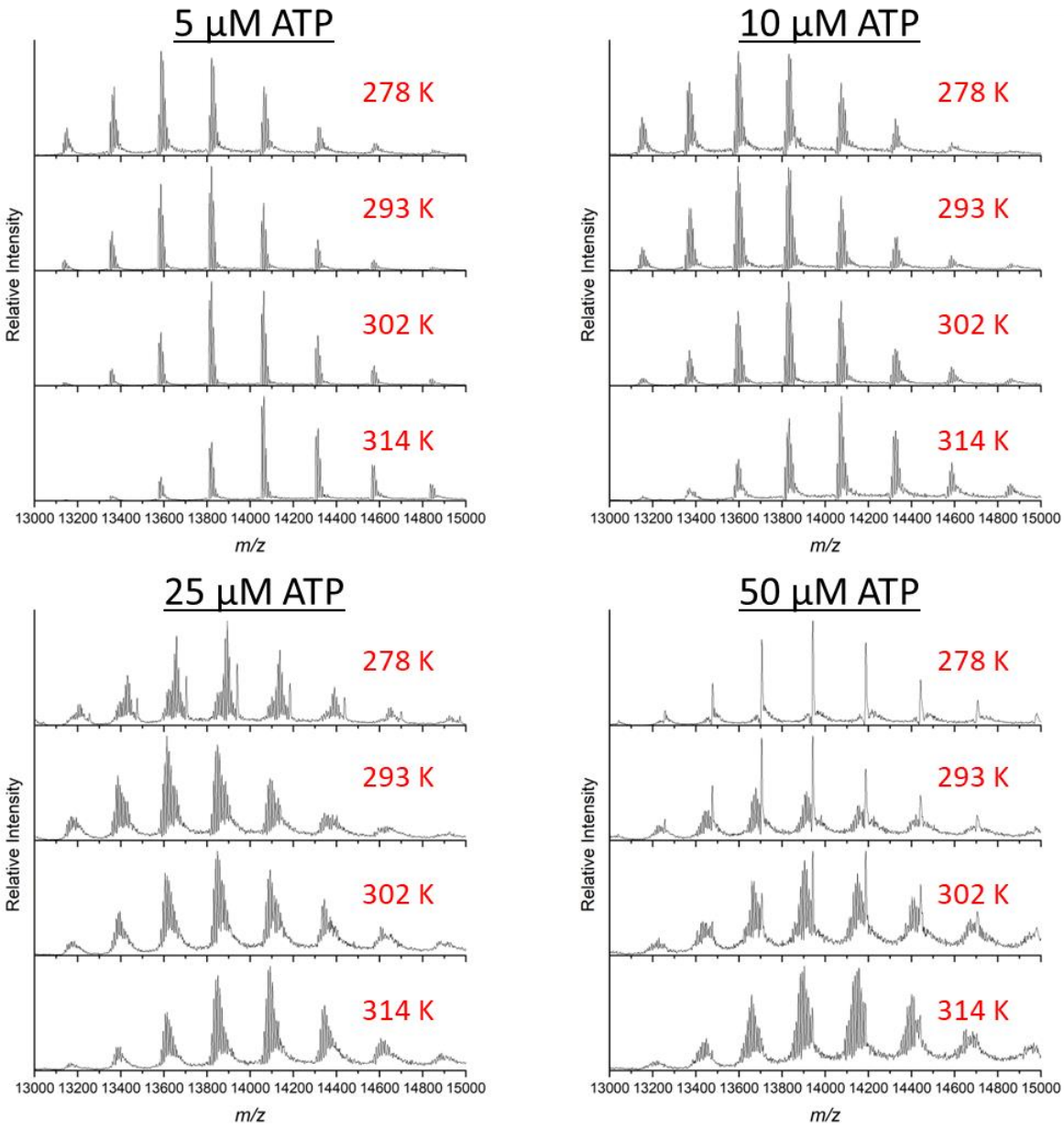

Figure 5.11 Representative spectra of GroEL-ATP_n binding at various temperatures and ATP concentrations. Overall, ATP binding signals were well resolved as demonstrated above. Solution conditions are 500 nM GroEL, 200 mM EDDA, 1 mM $MgAc_2$, and various concentrations of ATP.

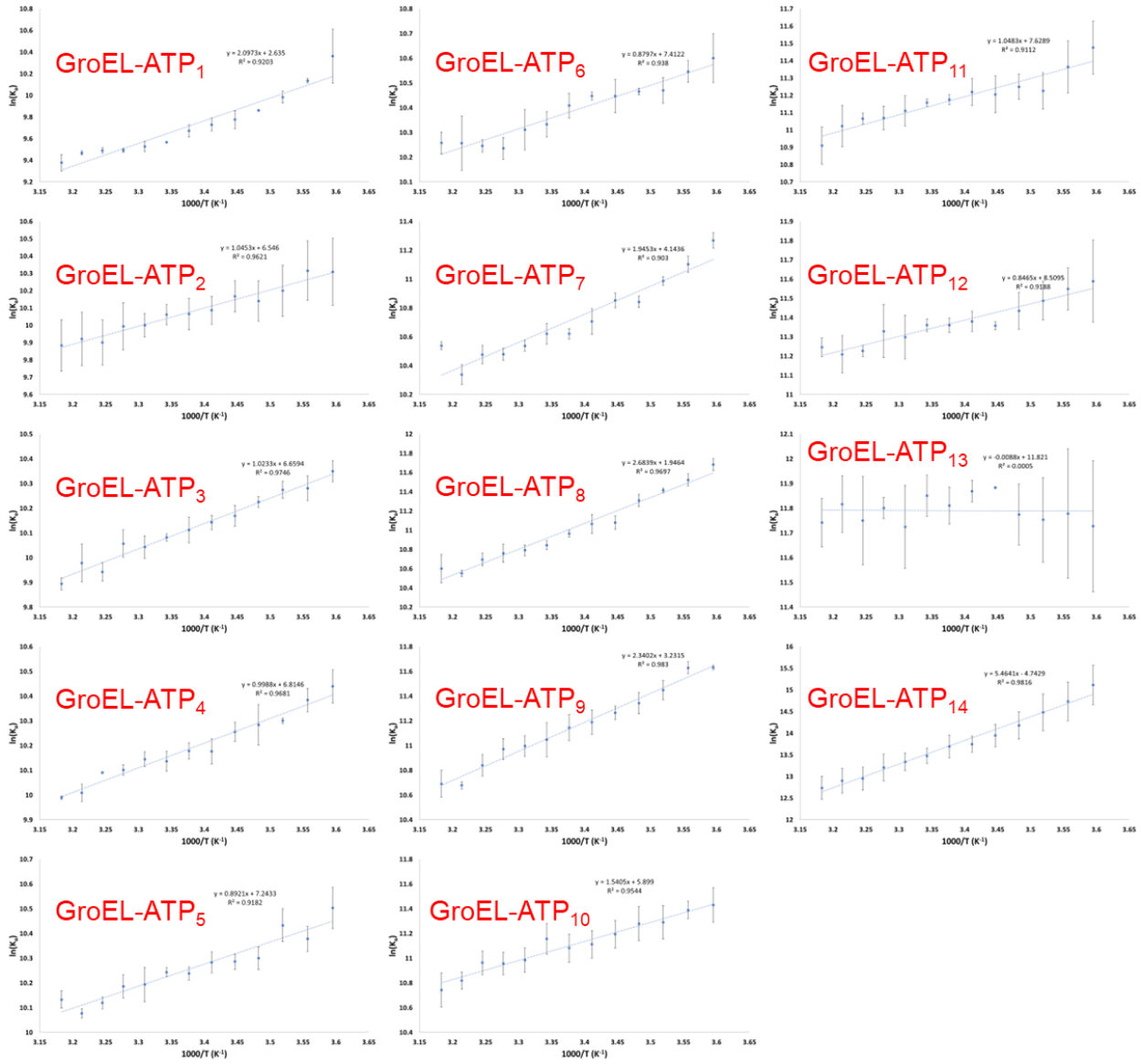

Figure 5.12 Van't Hoff plots for GroEL-ATP$_n$ binding in 200 mM EDDA (K_a vs 1000/T (K)).

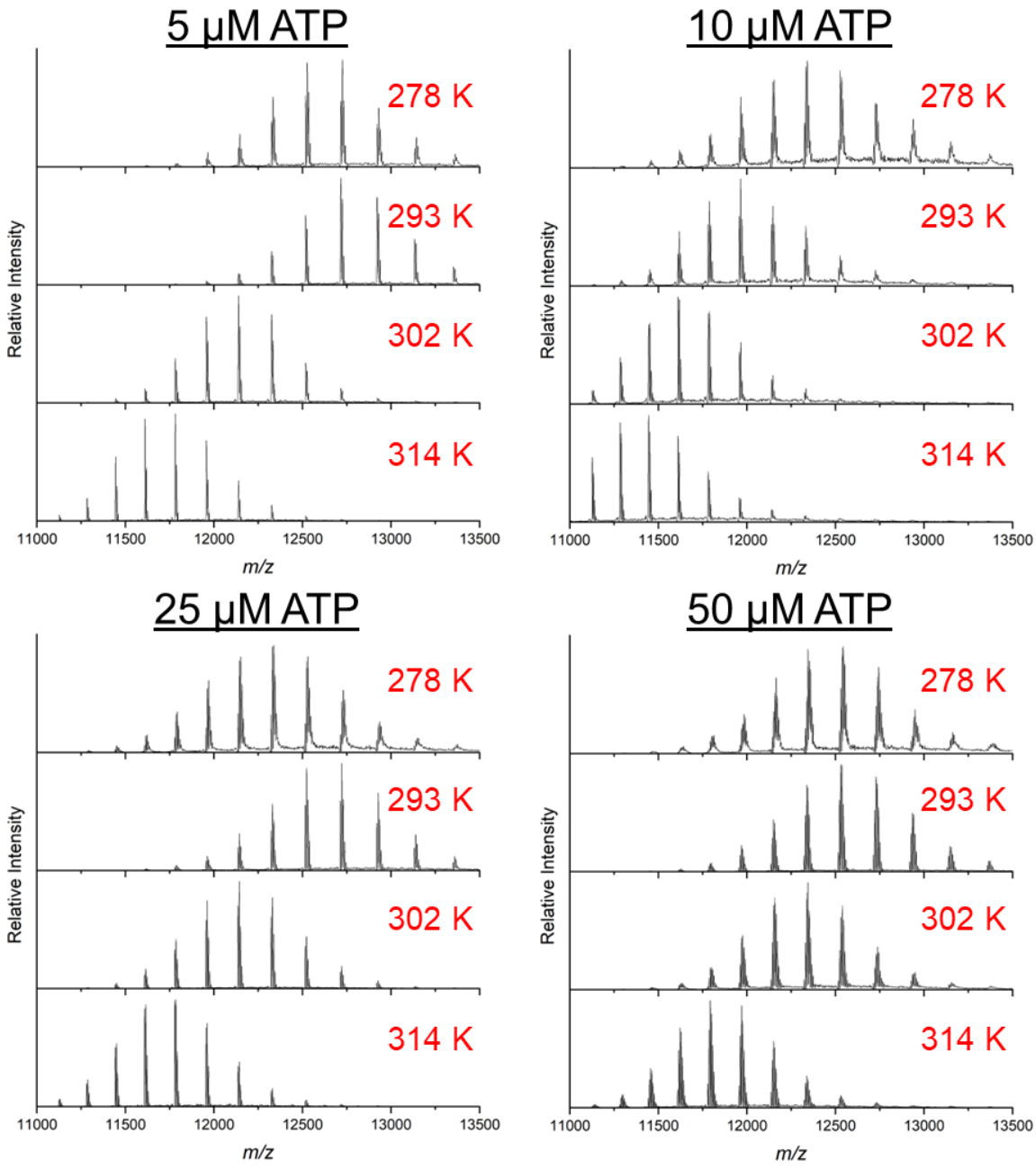

Figure 5.13 Representative spectra of GroEL-ADP_n binding at various temperatures and ATP concentrations. Overall, ATP binding signals were well resolved as demonstrated above. Solution conditions are 500 nM GroEL, 200 mM AmAc, 1 mM $MgAc_2$, and various concentrations of ATP. Note: ATP was added to the solution but only ADP binding was observed.

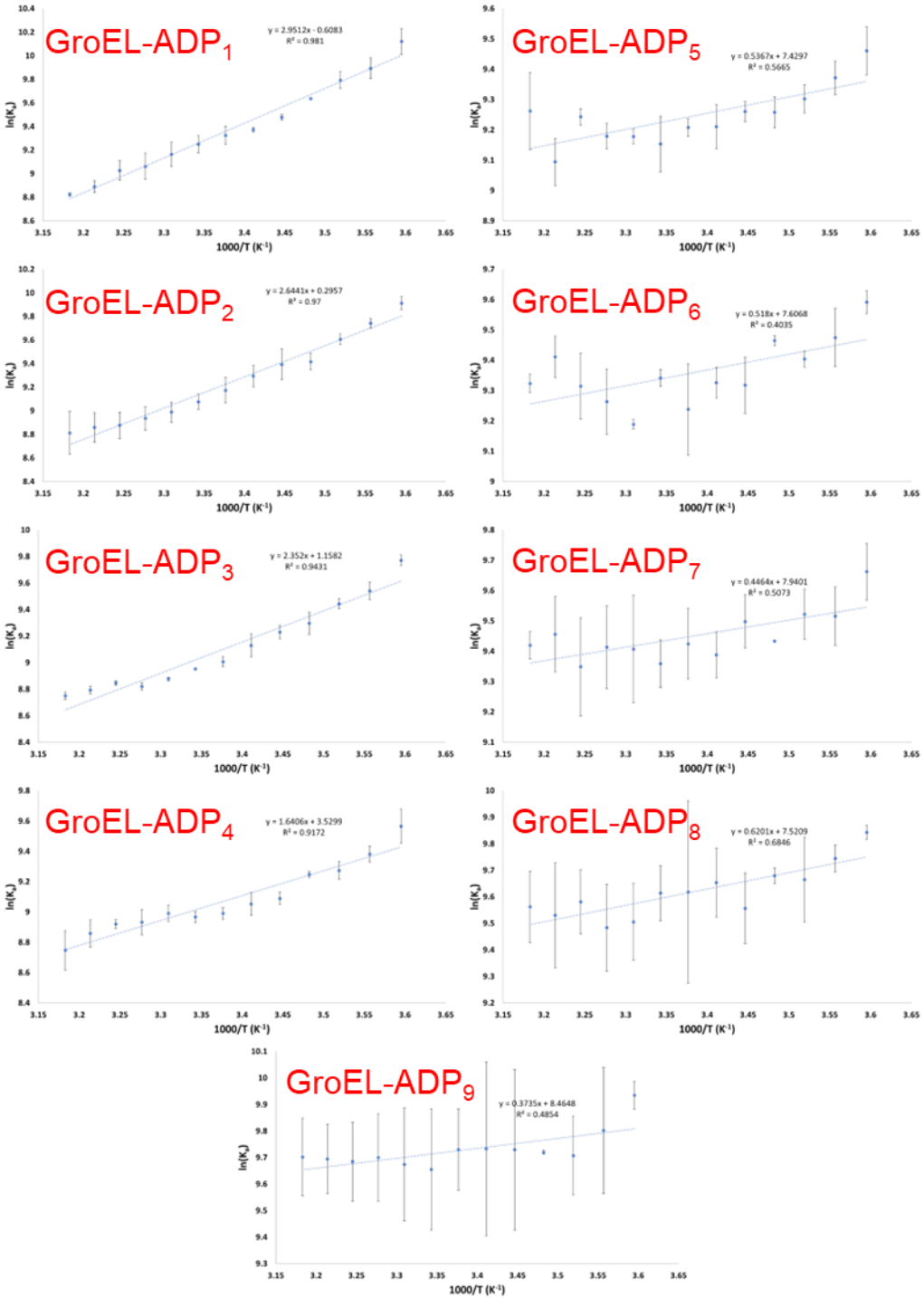

Figure 5.14 Van't Hoff plots for GroEL-ADP$_n$ binding in 200 mM AmAc (K_a vs 1000/T (K)). Note: ATP was added to the solution but only ADP binding was observed.

6. AMMONIUM IONS INDUCE HYDROLYSIS AND HIGHLY COOPERATIVE BINDING OF ATP BY GROEL

6.1. Background

GroEL is tetradecamer chaperonin protein complex composed of two heptameric rings which are further composed of seven 57 kDa monomers each.[112-114, 327, 351] The structure of the monomer subunits has been characterized by 3 distinct regions: apical, intermediate, and equatorial domains.[112-114, 327, 351] The apical domain is the most dynamics and provides a docking site for the co-chaperonin, GroES, the intermediate domain serves as hinge about which the apical domain is allosterically modulated, and the equatorial domain possess the nucleotide binding pocket and provides a firm interface for inter-ring binding and stability of the complex.[113, 301, 331, 345, 352, 353] GroEL exists to aid in protein folding, providing an "Anfinsen cage" environment to promote protein native structure.[112, 119, 354] The binding of ATP has been shown to induce allosteric transitions in the GroEL complex, such as extension of the apical domain to prepare for GroES docking.[113, 115, 121, 289, 329, 331, 341, 343, 352, 354] These allosteric transitions have drawn the attention of many researchers as binding of ATP to GroEL has been observed to be allosterically coupled. Horovitz et al proposed that ATP binding by GroEL is concerted intra-ring and sequential inter-ring; to describe this interpretation, the term nested-cooperativity was coined.[121] However, there still exists many aspects of GroEL function and structure that remain clouded, particularly the role of small ions

(Mg^{2+}, NH_4^+, and K^+) which have been shown to modulate ATP affinity and hydrolysis.[124, 335, 347]

Research conducted by Lorimer et al. has shown evidence that K^+ ions drive hydrolysis of ATP, which, in turn, affects rates of substrate folding. However, they also report that NH_4^+ ions can initiate similar levels of ATP hydrolysis and substrate folding.[335] Small monovalent cations (especially K^+) have been seen in XRD structures to bind in the nucleotide binding pocket.[334, 352, 355] It is theorized that in conjunction with Mg^{2+} that these ions help coordinate ATP stable enough for hydrolysis by the D52 residue.[334] In previous studies we have observed the effects ATP concentration, Mg^{2+} concentration, temperature, and buffer compositions on ATP and GroES binding.[11] However, we recently observed that ammonium acetate buffers promoted hydrolysis and elevated cooperative binding of ATP for a hydrolysis deficient mutant GroEL (D398A).[11]

Here, we report observations pertaining to the behavior of ATP binding in GroEL and the effects that NH_4^+ ions have on the binding mechanisms of ATP. We find that NH_4^+ is a suitable mimetic for K^+ in initiation of ATPase activity and that increased concentrations of AmAc correlated to faster rates of hydrolysis. Also, we note that AmAc modulates cooperativity of ATP binding in GroEL wild-type and the D398A mutant.

6.2. Results

Initial studies of ATP binding in GroEL were conducted using EDDA buffer to avoid potential ATPase activity brought on by the presence of NH_4^+ ions. When nucleotide

binding studies began in AmAc buffer, it was quickly realized that only ADP-binding was observed, which indicated that GroEL was hydrolyzing ATP to form ADP. To study this effect further, a hydrolysis deficient mutant, D398A, of GroEL was studied, which possesses a hydrolysis rate of ~2 % of that of wild type (wt)GroEL. **Figure 6.1** shows deconvoluted spectra that exhibit the change in binding affinity and pattern of nucleotides for both wt and D398A GroEL in AmAc and EDDA. In EDDA both types of GroEL bind ATP with a similar affinity and pattern. However, in AmAc the D398A mutant exhibits elevated levels of cooperative binding, forming primarily GroEL-ATP_{14}. The wtGroEL is

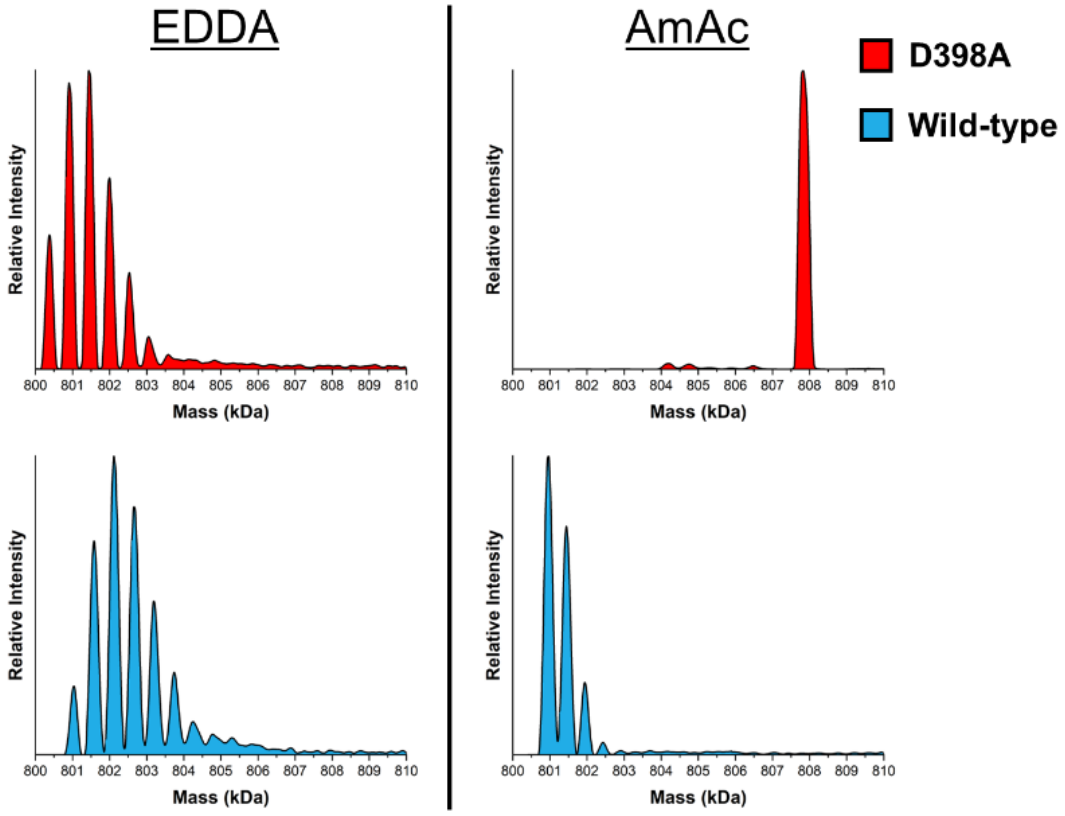

Figure 6.1 Comparison of wtGroEL and D398A mutant in both 200 mM EDDA (*left*) and 200 mM AmAc (*right*). ATP binding in EDDA is rather similar, but in AmAc the wtGroEL quickly hydrolyses ATP leading to much less nucleotide binding. The D398A mutant is slow to hydrolyze and is shown binding up to GroEL-ATP_{14}. Solution Conditions: 500 nM $wtGroEL_{14}$, 10 µM ATP, and 1 mM Mg^{2+}.

observed to only bind ADP at a lower affinity to that of ATP at the same concentration. The rate of hydrolysis of wtGroEL in 200 mM AmAc is sufficiently fast to hydrolyze the available ATP, leaving mostly ADP for GroEL to bind.

The ATP binding in the GroEL mutant was observed to be ATP-concentration dependent. **Figure 6.2** shows the deconvoluted spectral data for GroEL D398A in decreasing concentrations of ATP. It is interesting to note the level of cooperative binding displayed in the data. As the concentration of ATP is decreased the primarily ATP-bound

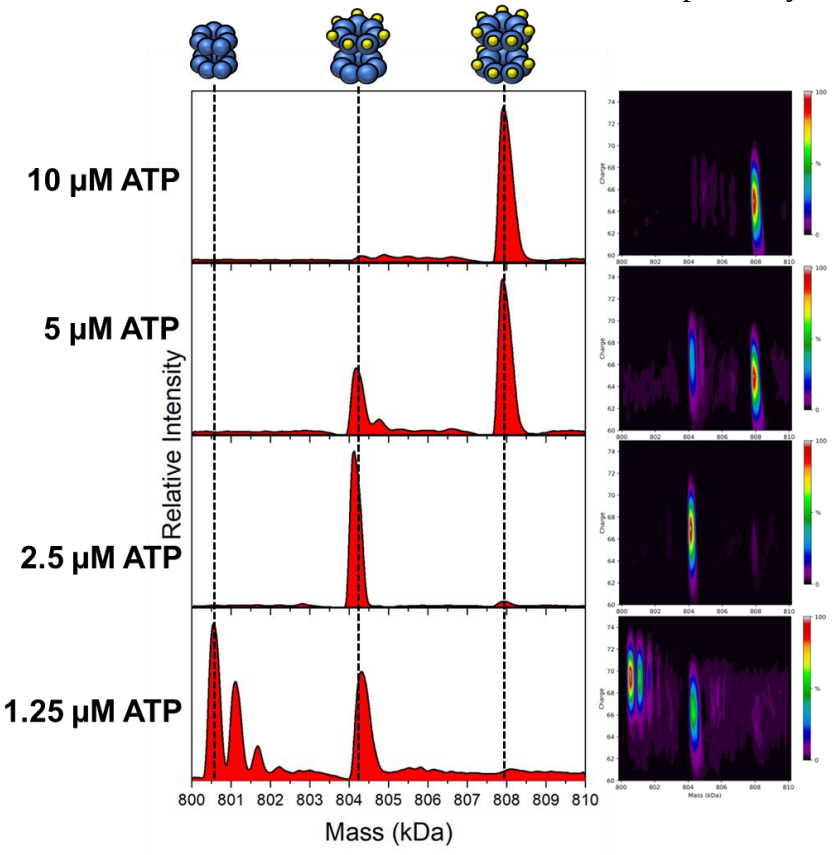

Figure 6.2 Deconvoluted spectra of GroEL D398A in response to different concentrations of ATP. Cooperative binding is elevated in the D398A mutant because the mutant can not hydrolyze ATP efficiently. The average charge state of the ATP-bound mutant also shifts in response to the filling of each ring with ATP as seen in the 2D plots of charge vs mass (*right*). Solution Conditions: 500 nM (D398A)GroEL$_{14}$, 1 mM Mg^{2+}, and 200 mM AmAc.

state transition form GroEL-ATP_{14} (full *trans* ring) to GroEL-ATP_7 (full *cis* ring) to GroEL-ATP_{1-3} (initial filling of *cis* ring). Most of intermediate binding steps are not observed, which corroborates the existence of significant levels of cooperative binding. In conjunction with the cooperative filling of the *cis* and *trans* rings the observed charge state of the GroEL-ATP_n ions shifts as each ring is filled. The average charge state (Z_{avg}) for

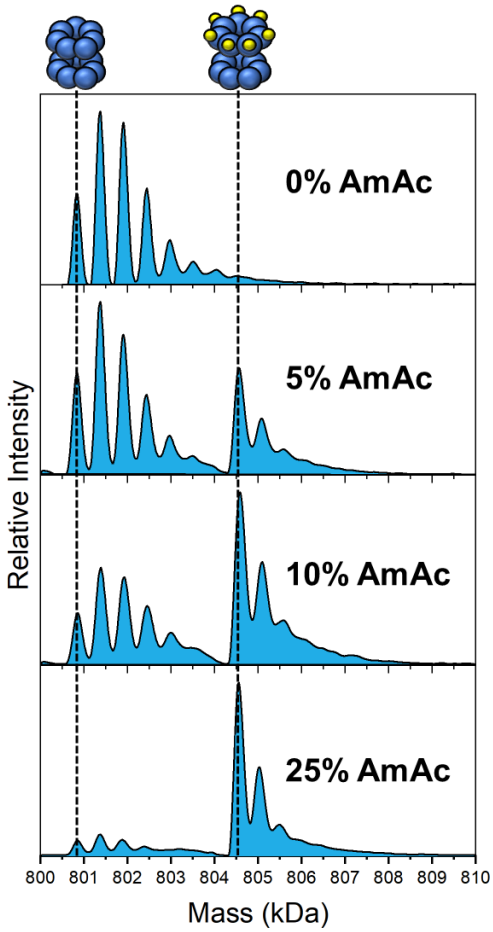

Figure 6.3 Deconvoluted spectra depicting wtGroEL-ATP binding in response to increasing concentration of AmAc. Data that are shown correspond to first minute of spectra acquisition. Increased AmAc concentrations coincided with increased coopertiviy, preferentially forming GroEL-ATP_7, and increased rate of ATP hydrolysis. Solution Conditions: 500 nM $wtGroEL_{14}$, 10 µM ATP, 1 mM Mg^{2+}, and 200 mM EDDA replaced by volume with 200 mM AmAc.

apo GroEL is 69.5^{+}, GroEL-ATP_7 is 66.2^{+}, and GroEL-ATP_{14} is 64.3^{+}. This phenomenon of such large transitions in Z_{avg} is not observed for wtGroEL in EDDA solutions.

To examine the effects of NH_4^+ ions on wtGroEL in a more controlled manner we mixed the buffers EDDA and AmAc (with 10 µM ATP and 1 mM Mg^{2+}) to steadily increase the amount of AmAc present in the sample with each subsequent experiment. The effect of increasing the NH_4^+ ion concentration available for wtGroEL in EDDA leads to increased cooperative binding of ATP, similar to that see in **Figure 6.2** for GroEL D398A. In **Figure 6.3** GroEL-ATP_7 becomes the dominant signal with increasing NH_4^+ concentration. Signals corresponding to GroEL-$ATP_{5\text{-}6}$ are absent and the intensity of

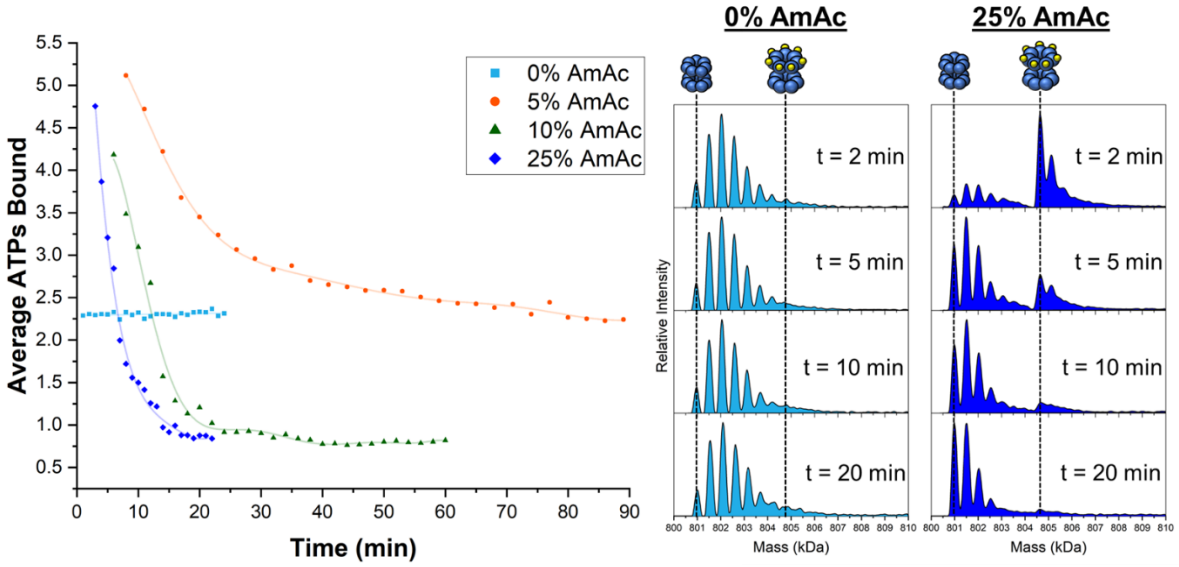

Figure 6.4 (*Left*) Plot of average ATP bound vs time. Portions of the 200 mM EDDA buffer were replaced by 200 mM AmAc buffer (given in percent by volume of AmAc in the legend) which led to loss of average numbers of ATP bound. This was interpreted as loss of ATP due to hydrolysis. (*Right*) Deconvoluted mass spectra showing the mass distribution of GroEL-ATP_n in 100:0 EDDA:AmAc and 75:25 EDDA:AmAc. Addition of AmAc greatly elevates cooperative binding in the *cis* ring (GroEL-ATP_7). However, over time the 100:0 EDDA:AmAc show no change in ATP binding, whereas the 75:25 EDDA:AmAc conditions show rapid loss of GroEL-ATP_7 and the increase in intensity of GroEL-$ATP_{0\text{-}3}$ signals. Solution Conditions: 500 nM $wtGroEL_{14}$, 10 µM ATP, and 1 mM Mg^{2+}.

GroEL-ATP_{0-4} diminishes with increasing NH_4^+ concentration. Once again, similar to the GroEL D398A mutant, a strong charge state shift is apparent upon formation of GroEL-ATP_7. ATP binding reaction are observed up to GroEL-ATP_{8-9} but no GroEL-ATP_{14} is observed for 10 µM ATP, however solutions containing 25µM ATP were observed to have GroEL-ATP_{14} products.

As a consequence of the addition of AmAc to the EDDA buffer, hydrolysis of ATP was observed the rate of which increased concomitantly with the NH_4^+ concentration. Hydrolysis is inferred from the decrease in bound ATP over time and the decrease in assigned mass shift of bound nucleotides with 530 Da being assigned to [Mg^{2+} + ATP] and 450 Da being assigned to [Mg^{2+} + ADP]. The timed experiments were held at a constant temperature of 25 °C using a custom variable temperature nano-electrospray ionization (vT-nESI) device.[13] **Figure 6.4** shows the average number of ATP molecules

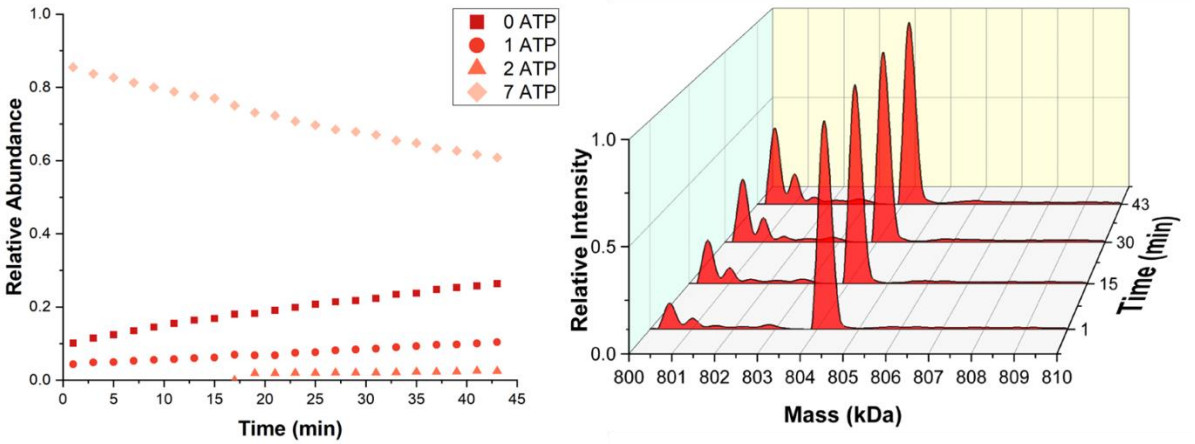

Figure 6.5 (*Left*) Plot of D398A GroEL-ATP_0, -ATP_1, -ATP_2, and -ATP_7 over time showing the slow rate of hydrolysis for the mutant. (*Right*) Waterfall plot showing the deconvoluted spectra of D398A GroEL-ATP over time. Note how the cooperativity of the ATP binding remains strong despite slow loss of GroEL-ATP_7. This observation indicates that ATP hydrolysis is likely concerted for the intra-ring unit. Solution Conditions: 500 nM (D398A)$GroEL_{14}$, 2.5 µM ATP, 1 mM Mg^{2+}, and 200 mM AmAc.

as a function of time. The rate of hydrolysis increases dramatically for 10 % and 25 % AmAc conditions with trends leveling off at about an average of 1 ATP bound within 20 and 15 minutes, respectively.

It is also interesting to note the progression of GroEL-ATP_n signals during hydrolysis. For wtGroEL the hydrolysis of ATP caused a shift in the abundance of GroEL-ATP_7 to GroEL-$ATP_{0\text{-}3}$; the intermediate binding reactions were not observed during the experiment. More interestingly for the GroEL D398A mutant in AmAc, a similar observation was made where the transition from GroEL-ATP_7 directly led to formation of GroEL-$ATP_{0\text{-}2}$. **Figure 6.5** shows the abundance of GroEL-$ATP_{0,1,2,7}$ as a function of time. The hydrolysis rate for the mutant is only about 2% that of wt but is still observable over several minutes. This evidence suggests that ATP hydrolysis by GroEL is "quantized" or cooperative for a full ring and not merely stochastic.

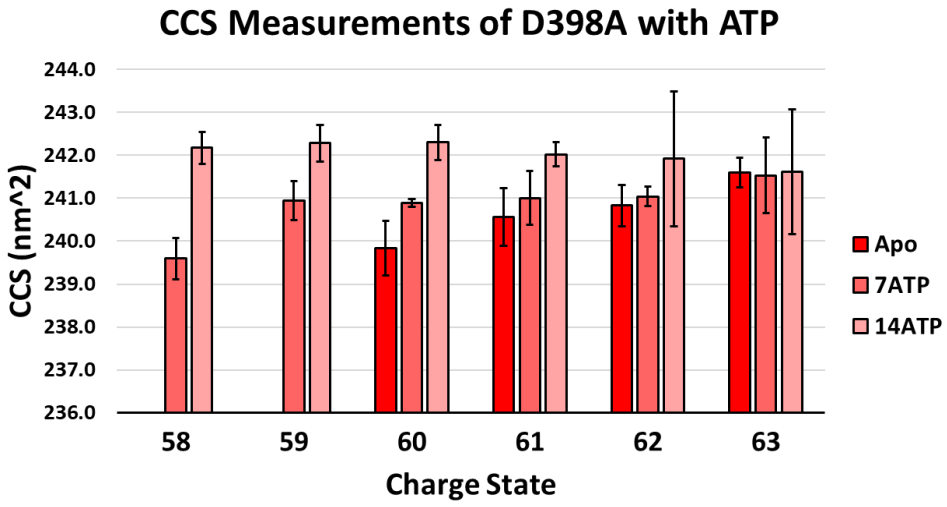

Figure 6.6 CCS measurements for D398A GroEL-ATP_0, -ATP_7, and -ATP_{14}. Note the slight increase in CCS as each ring is filled with ATP. Solution Conditions: 500 nM (D398A)$GroEL_{14}$, 10 μM ATP, 1 mM Mg^{2+}, and 200 mM AmAc.

Ion mobility (IM) data were collected (**Figure 6**) on the 3 main ATP bound states of the D398A mutatnt (GroEL-ATP_0, GroEL-ATP_7, and GroEL-ATP_{14}). The resulting collisional cross-sections (CCS) revealed that upon filling of each ring of GroEL there coincided a small increase in CCS which was charge state dependent. The increase in CCS across all 3 ATP-bound states is most clear for the 60^+ charge state; CCS measurements for GroEL-ATP_0, -ATP_7, and -ATP_{14} were 239.8, 240.9, and 242.3 nm^2, respectively. The CCS shifts are also apparent for lower charge states of GroEL-ATP_7 and -ATP_{14}, 58^+ and 59^+, where S/N is much higher for these ATP-bound states.

6.3. Discussion

6.3.1. The role of K^+ and NH_4^+ for ATP hydrolysis

Small ions are often necessary to ensure optimal functionality of protein complexes. In the case of GroEL, K^+ has been identified as an essential ion for preforming refolding function and even for the initiation of ATPase activity. Lorimer et al. also specify that other small ions such as Na^+, Li^+, and Cs^+ seemingly have no effect on the ATPase activity of GroEL, entailing that they are not appropriate substitutes for K^+.[335] However, NH_4^+ has been observed to be as effective as K^+ for activation of ATPase activity in GroEL. The ability for NH_4^+ to be a surrogate for K^+ explains initial observations for nucleotide binding by GroEL in AmAc, where only signals corresponding to GroEL-ADP_n are observed. The introduction of the GroEL D398A mutant to study binding in both EDDA and AmAc conditions demonstrated the 1) ATP binding by the mutant in EDDA was very similar to that of wt 2) due to the disrupted ability to hydrolyze ATP, the mutant

GroEL displayed elevated cooperativity in AmAc. The data presented in **Figure 6.1** for D398A in EDDA show that the mutant and wt behave very similarly for binding ATP, suggesting that mutation of the GroEL has not significantly altered the ATP affinity.

K^+ ions—and by extension NH_4^+ ions—have been shown to bind with the nucleotide in the nucleotide binding pocket located in the equatorial region of the GroEL.[334, 352, 355] This has been confirmed by heavy metal replacement XRD studies where thallium (a biological mimetic for K^+) was shown to bind in the same region as nucleotides along with 2 other potential binding sites, each in the intermediate and apical domains, though these sites may not be biologically active.[336] Several other XRD studies show that K^+ ions aid in the complexation of the thiophosphate chain in conjunction with Mg^{2+} to catalyze ATP hydrolysis. In respect to potential allosteric transitions upon ion binding, it is clear that EDDA somehow dampens certain aspects of positive cooperative binding of ATP and inhibits ATP hydrolysis (**Figure 6.4**). It is possible that EDDA solutions possess osmolyte characteristics that prevent certain allosteric transitions that may drive cooperative binding or that EDDA competes for binding in the nucleotide pocket but is too bulky to allow for efficient complexation to promote hydrolysis.

6.3.2. NH_4^+ concentration effect on rate of ATP hydrolysis

The theorization that EDDA may compete for binding in the nucleotide pocket draws support from data presented in **Figure 6.4** where increasing NH_4^+ ion concentration increases the apparent rate of ATP hydrolysis. Due to the limitations of the experimental

setup, the data acquisition begins several minutes after the ATP has been added to the sample. Despite this, it is clearly demonstrated that NH_4^+ concentration modulates the rate of ATP hydrolysis. This trend continues as in the case of 200 mM AmAc conditions there is no change in the average amount of nucleotides bound, indicating that all hydrolysis has already occurred in the few minutes of dead time from the mixing of the sample to the beginning of data acquisition.

6.3.3. Cooperativity of ATP binding

The comparison of the wt and mutant GroEL in EDDA is an interesting result that confirms that the mutation has not significantly altered the binding affinity of the complex (**Figure 6.1**), and, when compared to the AmAc results, signifies that the EDDA buffer in some way inhibits the functionality of the hydrolysis and the ATP affinity. In a previous study we show that in EDDA the filling of the *trans* ring is a highly cooperative event while the filling of the *cis* ring lacks the binding pattern associated with positive cooperativity. The AmAc data in **Figure 6.2** show markedly different results; however, in the absence of hydrolysis, the GroEL D398A nearly entirely forms GroEL-ATP_{14} in the presence of 10 μM ATP. When the ATP concentration is lowered to 2.5 μM, mostly GroEL-ATP_7 is formed. Note that the intermediate binding reactions are unobserved, which speaks to elevated levels of cooperativity observed in the spectra. When GroEL is able to bind 1 or 2 ATP the equilibria shift to fill the ring. This observation is consistent with Chapman et al. who reported a similar cooperative effect for the binding of up to 3

ATP molecules in a ring.[330] Unlike wtGroEL, the mutant is slow to hydrolyze which may be a reason for preferential stabilization of its fully saturated state.

The wtGroEL data, with low concentrations of NH_4^+ ions, exhibit a similar pattern of ATP binding as the mutant in AmAc conditions (**Figures 6.3** and **6.4**). Elevated levels of *cis* ring cooperative binding of ATP resulting in preferential formation of GroEL-ATP_7 become more prevalent as the concentration of NH_4^+ ions is increased. The binding pattern is similar to that of the mutant in AmAc except that more intermediate states (GroEL-$ATP_{1\text{-}4}$) are observed, which is more in agreement with Chapman's findings.[330] Interestingly, binding into the *trans* ring seems to be curtailed compared to the mutant. The activation of the ATPase mechanism may offer an explanation to this observation where the *trans* ring cannot bind ATP before the *cis* ring undergoes hydrolysis. However, this observation also points to the presence of negative inter-ring cooperativity; the filling of the *trans* ring is allosterically disfavored under hydrolysis-active conditions.

6.3.4. Relation to the nested-cooperativity model

The binding of ATP by GroEL is thought to follow the aforementioned nested-cooperativity model first proposed by Horovitz et al.[121] The model proposed that intraring binding is conducted in accordance with the Monod-Wyman-Changeux (MWC) model,[125] in which the entire ring existed in either a T or R state, and inter-ring binding is governed by the Koshland-Némethy-Filmer (KNF) model,[127] where allosteric transitions in one protomer can have allosteric effects on its immediate neighboring protomers.[2, 121, 122] The consequence of this model is that ATP binding occurs in a

non-stochastic manner where ATP molecules are bound by one ring at a time. The data presented in **Figures 6.1-6.5** support this model as the binding in AmAc conditions for both wt and D398A mutant show high levels of intra-ring cooperativity. The preferential formation of GroEL-ATP_7 in mixed buffer conditions shows that a cooperative transition occurs upon the binding of 1-3 ATP molecules that favors the filling of the *cis* ring and disfavors filling of the *trans* ring. The lack of significant ATP binding into the *trans* ring indicates an instability for the formation of a fully saturated GroEL complex under these conditions. This interpretation aligns well with the proposition of negative inter-ring cooperativity.

Another interesting observation exists for the time dependent binding data of the wt and mutant GroEL in relation to the cooperativity of ATP hydrolysis (**Figure 6.4**). The signals of the GroEL-ATP_n states shift from predominantly ATP_7 to ATP_{1-3} over several minutes, however, the intermediate binding reactions are not observed even as ATP is hydrolyzed. This observation supports a "conformational wave" model of ATP hydrolysis where, as ATP is hydrolyzed in one subunit the other subunits of the same ring hydrolyze ATP in a concerted manner.[120, 123] Even though the D398A mutant has been shown retain only ~2% of the wt hydrolysis rate, [114, 118, 326, 327, 329] the loss of GroEL-ATP_7 over tens of minutes results in the formation of GroEL-ATP_{0-2} which means that hydrolysis of ATP in the mutant is still concerted. Another possible explanation for this is that the hydrolysis of one ATP leads to destabilization of the rest of the ATP bound states.

6.3.5. Allosteric transitions of GroEL

The Z_{avg} of protein ions provides some indication of the solvent accessible surface area (SASA) for the protein during the transition to gas phase.[244, 245] The large charge state shift to lower charge that accompanies ATP filling the *cis* ring in AmAc is counterintuitive to what is known about the conformational transition upon binding of ATP. Upon binding of ATP, the apical domain has been shown to rotate around the intermediate domain and extend to facilitate docking of GroES. This extension of the apical domain should increase the SASA of the complex overall, yet upon formation of GroEL-ATP_7 in AmAc the average charge state decreases by 4 to 5 charges (**Figure 6.2**). The loss of overall charge may be explained by the exposure of hydrophobic residues and the burial of hydrophilic residues in the cavity upon ATP binding.[120, 352, 356-359] If these hydrophilic residues in the cavity are buried, they may not be prone to accept charge upon transition to the gas phase via ESI. Despite the loss of charge, IM-MS data show that upon filling of each ring of GroEL the cross-section measurement increases slightly for measurements of the same charge state. The shifts in CCS shown in **Figure 6.6** are smaller than expected but are statistically significant, showing that upon complete filling of a ring, GroEL does undergo a small elongation in overall structure as proposed by XRD studies.[112-114, 301, 352, 360] The shift in charge state coinciding with filling of the *trans* ring decreases by only 1 to 2 charges on average. This may indicate that the *trans* ring does not (or is unable to) undergo conformational transitions as drastic as observed for the *cis* ring binding. This effect has also been observed in XRD studies where the symmetry between the rings is lost for the formation of GroEL-ATP_{14}.

6.4. Methods

Wild-type and D398A mutant GroEL were overexpressed in *E. coli*, purified, aliquoted, and frozen at -80 °C. Prior to analysis GroEL was thawed and buffer exchanged, using Biorad Biospin P-6 size exclusion columns, into either AmAc or EDDA at a concentration of 2 µM. New solutions of MgAc and ATP were prepared each day prior to analysis. MgAc was obtained from Sigma and ATP was obtained from Sigma in the form of ATP disodium salt hydrate. Directly preceding analysis, the solutions were combined to the desired concentration of each solution constituent. All spectra were deconvoluted using the UniDec deconvolution software.[232]

All nMS analysis was conducted on a Thermo Scientific UHMR orbitrap, and all IM-MS analysis was conducted using a home-built 1.5 m drift tube coupled to the UHMR instrument; details pertaining to the IM-MS instrument have been published previously.[70, 234] The drift gas used was He at a measured pressure of 1.62 torr and at a field strength of 6.5 V/cm. The instrument tuning method was optimized to promote desolvated, declustered ions without causing dissociation of the GroEL complex. Capillary temperature was maintained at 200 °C, desolvation voltage (in-source trapping): -200V, HCD energy: 150 V, maximum inject time: 200 µs, orbitrap resolution setting: 25000, microscanning: 3, and trap gas setting (N_2): 7.0.

All time dependent studies were done at 25 °C in which the temperature of the emitter was controlled via a variable-temperature (vT)-ESI source. Details pertaining to

the vT-ESI source have been published previously.[13] All time-dependent data include the “dead time” associated with loading the emitter and beginning of data acquisition.

7. CONCLUSIONS

7.1. Conclusions

The use of vT-ESI affords the quantitation of thermodynamic values via nMS for a variety of interactions from small peptides to large protein complexes. An understanding of the underlying thermodynamic contributions to a system is vital to gaining a more comprehensive elucidation of biochemical mechanisms.

Osmolyte interactions with proteins was a long-standing project that showed some initial progress using cryo-IM-MS. The initial water network distribution that was expected to be observed was not present, but the formation of a SP dimer proved to be an interesting result. Ultimately with the introduction of the vT-ESI device, using cryo-IM-MS proved to be too time-consuming which is what led to doing these studies on the Synapt-G2. The EEC dynamic for the dimerization and TMAO complexation interactions was very interesting and led to more investigation of this topic. However, the mechanism switching for both of the dimerization and complexation reactions at around the same solution temperature was the most intriguing observation made during the project. The fact that the dimerization of the SP peptides at low temperature was subject to a lower entropy barrier and was correlated with the complexation of the SP monomer and TMAO demonstrates that the TMAO interaction is vital to formation of SP dimers. This observation has far-reaching implications for osmolyte induced protein folding, protein complex self-assembly, and how entropy drives these interactions.

Having the GroEL-ATP binding interaction be one of the first vT-ESI thermodynamic experiments was potentially hazardous due to the complexity of monitoring 14 binding reactions. However, this study truly shows the ability of nMS by enabling the observation of specific binding reactions. No other method currently available would be able to achieve this level of specificity in a similar time of analysis. Another thing to note was the agreement between the interpretation of the MS data with that of the solution-phase data. The nMS experiments observed thermodynamic patterns that seemed to indicate that there were signs of "nested cooperativity" in the binding of ATP by GroEL.

An interesting aside, almost accidental discovery, was the observation that NH_4^+ ions induce ATP hydrolysis in GroEL. Almost immediately upon this realization the differences in binding patterns between the GroEL in EDDA vs AmAc began to make sense. Further studies were conducted that showed the rate of hydrolysis was closely tied to the concentration of AmAc. This opens up possibilities for future kinetic studies on GroEL hydrolysis via nMS. Another observation to note was the increased cooperativity observed with the addition NH_4^+ ions to the EDDA buffer. It appears that in EDDA buffer the GroEL operates in some semi-functional manner as it is unable to hydrolyze ATP but still shows clear signs of cooperative binding. However, upon addition of NH_4^+ ions, hydrolytic activity becomes apparent and cooperative ATP binding is more prevalent, seemingly indicating that these conditions are more akin to native cellular conditions. The most likely explanation for this phenomenon is that EDDA can competitively bind with

other small ions in the ATP-binding pocket, but this action precludes hydrolysis activity. Future studies will need to be conducted with other amine containing compounds.

The most pressing concern for the vT-ESI thermodynamic studies and for nMS as whole is the comparison of results to solution-phase measurements. Concerns have been raised about the robustness of nMS techniques and accuracy of results obtained with nMS. These concerns break down further into concerns of "MS-friendly" buffers not being representative of biologically relevant solution conditions to variations between nano and direct infusion ESI. However, as with any measurement technique, results can be biased depending on the criterion used to categorize and interpret the results. For the results discussed in the previous chapters it is encouraging to see some broad agreement between the nMS data and vT-ESI thermodynamics data with previous literature, especially concerning the GroEL-ATP binding. The specificity with which the nMS results are able make measurements makes direct comparison with solution-phase measurements difficult for multiligand systems, as nMS can discern between various bound states of proteins and traditional solution-phase measurements are not. It will be necessary though to continue these experiments in an effort to streamline and better characterize these methods for future nMS thermodynamic studies.

Studies on small molecules' role in electrospray offered a more complete view of certain processes the underpin charging in ESI. Although that there are still interesting aberrations in the proposed mechanism of charge reduction in nMS—most notably TMAO—the work done so far has shown the ability to treat the conditions of the solution as another tuning parameter which is available to investigators.

The results discussed in Chapter 3 made very clear that charge reduction was an effect of the hydrophobicity of the charge reducing reagents, however, there are anomalies to every trend. TMAO is more hydrophilic than any of the amines and polyamines used in the study, yet TMAO is able to charge reduce with the highest level of proficiency. One of the central questions is if TMAO charge reduces through an osmolyte stabilization effect or if it charge reduces by removing more excess charges than other reagents. Initial IM-MS studies, targeted at detecting conformational changes in proteins, proved difficult to conduct as TMAO charge reduces proteins so effectively that instrument conditions must be changed to ensure transmission. This obviously is a problem for making direct comparisons between TMAO and non-TMAO data. More work is needed on this front for a better understanding of the most complete mechanism of TMAO-induced charge reduction.

7.2. Future Directions

7.2.1. GroEL-ATP

The initial studies with GroEL-ATP binding provided insight into the underlying thermodynamics of the nucleotide binding of GroEL. GroEL mutants with point-mutations were later introduces (such as the hydrolysis-deficient D398A mutant) to observed potential changes in the binding patterns and thermodynamics. New mutants, such as the single ring mutant (SR1) and c-terminal truncation mutant, are also slated to begin undergoing temperature dependent analysis for their nucleotide binding behavior.

SR1 will have binding interactions that are free of the inter-ring negative cooperativity present in the wtGroEL. Studies of this mutant will be excellent to determining how heptameric rings of GroEL operate on their own. The c-terminus of GroEL is highly dynamic and located inside the cavity forming the "floor" of each cavity. The c-terminus is thought to have a measurable impact on the binding allostery of ATP to GroEL. Thermodynamic studies would provide insight into potential entropic impacts of the internal environment of the cavity.

Lastly, solution-phase data report that GroEL binds ATP in an ordered manner, meaning that ATP binding occurs one ring at a time. However, to unambiguously conclude this using nMS is possible and would provide yet another example of the capabilities of nMS. Preliminary data using CID to dissociate $GroEL_{14}$-ATP_7 show some weak signals for the formation of apo-$GroEL_7$ and $GroEL_7$-ATP_7 with no intermediate ATP bound states. This entails that when the ring of $GroEL_{14}$ is split that only full and empty rings exist. A better method to use for this experiment is SID which is excellent for the elucidation of structural topology of protein complexes. Potential concerns are that SID may be too energetic and result in a loss of bound ligands, but to date, no amount of gas-phase collision energy used in preliminary studies has been shown to remove ATP ligands from GroEL or even GroEL subunits. SID studies would provide unequivocal evidence for stochastic vs concerted binding of ATP by GroEL.

7.2.2. GroEL Folding Reactions

The primary function of GroEL is to aid in the folding process of unfolded or misfolded substrate proteins. While GroEL-ATP and GroEL-GroES nMS studies were discussed earlier, a next step for these experiments will be the incorporation of substrate for analysis of the folding pathway reactions. The primary difficulty in these studies will be the incorporation of an unfolded protein into a nMS buffer in a way that will not perturb the function of GroEL itself. Folding studies have been completed using a double mutant of maltose binding protein (dmMBP) that folds on the time scale of minutes that may make an excellent test substrate for nMS guided studies. The utilization of nMS for studying this system will provide an excellent case study for the utility of nMS for measuring kinetics and stoichiometry of chaperonin interactions.

7.2.3. Doubly Charged Water Clusters

Early cryo-IM-MS studies on osmolyte interactions led to an interesting side-effect observed in the IM-MS spectra. Upon addition of TMAO to SP doubly charged water clusters were observed. This observation is not necessarily problematic, however doubly charged water clusters as low as n = 14 waters were observed. To have a water cluster this small with 2 positive charges residing in it would far surpass the Rayleigh limit for spherical droplets. This curious phenomenon was reproduced several times but remains largely unexplained. More cryo-IM-MS studies are needed along with MD simulations to give explanations as to how these doubly charged water clusters are formed and stabilized.

7.2.4. HT-Cryo-IM-MS

Cryo-IM-MS is a method that is plagued with inefficient ion transmission and a low duty cycle in the IM-MS mode. To improve the overall operation of the instrument, an HT pulsing mode for the IMS system was incorporated which raised the theoretical duty cycle to 50%. The initial experiments using the HT-IM mode decreased the amount of time needed to acquire an IM-MS spectrum from 4 hours to 15 minutes. However, some issues with the current instrument software were made apparent during these studies. The frequency measurements of the software were problematic as the input frequency did not match the output frequency measured in the circuit except for a few, seemingly arbitrary, frequencies. The frequency mismatch led to a host of problems for the timing of the interleaved ToF frequency and the IMS deconvolution. To fix these problems new software and hardware will be needed that does not have errors associated with the digital frequency output.

REFERENCES

1. Turecek, F. and F.W. Mclafferty, *Interpretation of Mass Spectra*. 4th ed., Mill Valley, Ca.: University Science Books.
2. Dyachenko, A., et al., *Allosteric mechanisms can be distinguished using structural mass spectrometry.* Proc Natl Acad Sci U S A, 2013. **110**(18): p. 7235-9.
3. Laganowsky, A., et al., *Membrane proteins bind lipids selectively to modulate their structure and function.* Nature, 2014. **510**(7503): p. 172-175.
4. Lutomski, C.A., et al., *Multiple Pathways in Capsid Assembly.* J Am Chem Soc, 2018. **140**(17): p. 5784-5790.
5. McCabe, J.W., et al., *The Ims Paradox: A Perspective on Structural Ion Mobility-Mass Spectrometry.* Mass Spectrom Rev, 2020.
6. Leney, A.C. and A.J. Heck, *Native Mass Spectrometry: What is in the Name?* J Am Soc Mass Spectrom, 2017. **28**(1): p. 5-13.
7. Bennett, J.L., G.T.H. Nguyen, and W.A. Donald, *Protein-Small Molecule Interactions in Native Mass Spectrometry.* Chem Rev, 2022. **122**(8): p. 7327-7385.
8. Cong, X., et al., *Determining Membrane Protein-Lipid Binding Thermodynamics Using Native Mass Spectrometry.* J Am Chem Soc, 2016. **138**(13): p. 4346-9.
9. Sharon, M. and A. Horovitz, *Probing allosteric mechanisms using native mass spectrometry.* Curr Opin Struct Biol, 2015. **34**: p. 7-16.
10. Campuzano, I.D.G. and W. Sandoval, *Denaturing and Native Mass Spectrometric Analytics for Biotherapeutic Drug Discovery Research: Historical, Current, and Future Personal Perspectives.* J Am Soc Mass Spectrom, 2021. **32**(8): p. 1861-1885.
11. Walker, T.E., et al., *Temperature Regulates Stability, Ligand Binding (Mg(2+) and ATP), and Stoichiometry of GroEL-GroES Complexes.* J Am Chem Soc, 2022. **144**(6): p. 2667-2678.
12. Laganowsky, A., D.E. Clemmer, and D.H. Russell, *Variable-Temperature Native Mass Spectrometry for Studies of Protein Folding, Stabilities, Assembly, and Molecular Interactions.* Annu Rev Biophys, 2022. **51**: p. 63-77.
13. McCabe, J.W., et al., *Variable-Temperature Electrospray Ionization for Temperature-Dependent Folding/Refolding Reactions of Proteins and Ligand Binding.* Anal Chem, 2021.
14. Woodall, D.W., et al., *Variable-Temperature ESI-IMS-MS Analysis of Myohemerythrin Reveals Ligand Losses, Unfolding, and a Non-Native Disulfide Bond.* Anal Chem, 2019. **91**(10): p. 6808-6814.

15. Qiao, P., et al., *Entropy in the Molecular Recognition of Membrane Protein-Lipid Interactions.* J Phys Chem Lett, 2021. **12**(51): p. 12218-12224.

16. Karas, M., D. Bachmann, and F. Hillenkamp, *Influence of the Wavelength in High-Irradiance Ultraviolet-Laser Desorption Mass-Spectrometry of Organic-Molecules.* Analytical Chemistry, 1985. **57**(14): p. 2935-2939.

17. Fenn, J.B., et al., *Electrospray Ionization-Principles and Practice.* Mass Spectrometry Reviews, 1990. **9**(1): p. 37-70.

18. Smith, J.N., R.C. Flagan, and J.L. Beauchamp, *Droplet evaporation and discharge dynamics in electrospray ionization.* Journal of Physical Chemistry A, 2002. **106**(42): p. 9957-9967.

19. Lee, S.W., et al., *Freeze-dried biomolecules: FT-ICR studies of the specific solvation of functional groups and clathrate formation observed by the slow evaporation of water from hydrated peptides and model compounds in the gas phase.* Journal of the American Chemical Society, 1998. **120**(45): p. 11758-11765.

20. McCabe, J.W., et al., *Implementing Digital-Waveform Technology for Extended m/z Range Operation on a Native Dual-Quadrupole FT-IM-Orbitrap Mass Spectrometer.* J Am Soc Mass Spectrom, 2021. **32**(12): p. 2812-2820.

21. Reilly, P.T.A., et al., *Will the Digital Mass Filter Be the Next High-Resolution High-Mass Analyzer?* J Am Soc Mass Spectrom, 2021. **32**(10): p. 2615-2620.

22. McLean, J.A., et al., *Ion mobility–mass spectrometry: a new paradigm for proteomics.* International Journal of Mass Spectrometry, 2005. **240**(3): p. 301-315.

23. Zhou, M., C. Huang, and V.H. Wysocki, *Surface-induced dissociation of ion mobility-separated noncovalent complexes in a quadrupole/time-of-flight mass spectrometer.* Anal Chem, 2012. **84**(14): p. 6016-23.

24. Voinov, V.G., et al., *Electron capture, collision-induced, and electron capture-collision induced dissociation in Q-TOF.* J Am Soc Mass Spectrom, 2011. **22**(4): p. 607-11.

25. Crowe, M.C. and J.S. Brodbelt, *Infrared multiphoton dissociation (IRMPD) and collisionally activated dissociation of peptides in a quadrupole ion trap with selective IRMPD of phosphopeptides.* J Am Soc Mass Spectrom, 2004. **15**(11): p. 1581-92.

26. Madsen, J.A., et al., *IR and UV photodissociation as analytical tools for characterizing lipid A structures.* Anal Chem, 2011. **83**(13): p. 5107-13.

27. Breuker, K. and F.W. McLafferty, *Native electron capture dissociation for the structural characterization of noncovalent interactions in native cytochrome C.* Angew Chem Int Ed Engl, 2003. **42**(40): p. 4900-4.

28. Breuker, K., et al., *Detailed unfolding and folding of gaseous ubiquitin ions characterized by electron capture dissociation.* J Am Chem Soc, 2002. **124**(22): p. 6407-20.

29. Whitehouse, C.M., et al., *Electrospray interface for liquid chromatographs and mass spectrometers.* Anal Chem, 1985. **57**(3): p. 675-9.

30. Keifer, D.Z., E.E. Pierson, and M.F. Jarrold, *Charge detection mass spectrometry: weighing heavier things.* Analyst, 2017. **142**(10): p. 1654-1671.

31. Kebarle, P. and U.H. Verkerk, *Electrospray: from ions in solution to ions in the gas phase, what we know now.* Mass Spectrom Rev, 2009. **28**(6): p. 898-917.

32. Gamero-Castano, M. and J.F. de la Mora, *Mechanisms of electrospray ionization of singly and multiply charged salt clusters.* Analytica Chimica Acta, 2000. **406**(1): p. 67-91.

33. Rayleigh, L., *London Math. Soc.* Proc. 17, 1879.

34. Xia, Z., J.B. DeGrandchamp, and E.R. Williams, *Native mass spectrometry beyond ammonium acetate: effects of nonvolatile salts on protein stability and structure.* Analyst, 2019. **144**(8): p. 2565-2573.

35. Benesch, J.L., et al., *Protein complexes in the gas phase: technology for structural genomics and proteomics.* Chem Rev, 2007. **107**(8): p. 3544-67.

36. Ruotolo, B.T. and C.V. Robinson, *Aspects of native proteins are retained in vacuum.* Curr Opin Chem Biol, 2006. **10**(5): p. 402-8.

37. Breuker, K. and F.W. McLafferty, *Stepwise evolution ofprotein native structure with electrospray into the gas phase.* PNAS, 2005. **- 105**(- 47).

38. Natalia Felitsyn, M.P., Paul Kebarle, *Origin and number of charges observed on multiply-protonated native proteins produced by ESI.* International Journal of Mass Spectrometry, 2002. **219**: p. 39-62.

39. Iavarone, A.T. and E.R. Williams, *Supercharging in electrospray ionization: effects on signal and charge.* International Journal of Mass Spectrometry, 2002. **219**(1): p. 63-72.

40. Gamero-Castano, M. and J.F. Mora, *Kinetics of small ion evaporation from the charge and mass distribution of multiply charged clusters in electrosprays.* J Mass Spectrom, 2000. **35**(7): p. 790-803.

41. Iavarone, A.T., J.C. Jurchen, and E.R. Williams, *Effects of solvent on the maximum charge state and charge state distribution of protein ions produced by electrospray ionization.* J Am Soc Mass Spectrom, 2000. **11**(11): p. 976-85.

42. Wilm, M. and M. Mann, *Analytical properties of the nanoelectrospray ion source.* Anal Chem, 1996. **68**(1): p. 1-8.

43. Gibson, G.T., S.M. Mugo, and R.D. Oleschuk, *Nanoelectrospray emitters: trends and perspective.* Mass Spectrom Rev, 2009. **28**(6): p. 918-36.

44. Benkestock, K., et al., *Influence of droplet size, capillary-cone distance and selected instrumental parameters for the analysis of noncovalent protein-ligand complexes by nano-electrospray ionization mass spectrometry.* J Mass Spectrom, 2004. **39**(9): p. 1059-67.

45. Susa, A.C., Z. Xia, and E.R. Williams, *Native Mass Spectrometry from Common Buffers with Salts That Mimic the Extracellular Environment.* Angew Chem Int Ed Engl, 2017. **56**(27): p. 7912-7915.

46. Fort, K.L., et al., *Expanding the structural analysis capabilities on an Orbitrap-based mass spectrometer for large macromolecular complexes.* Analyst, 2017. **143**(1): p. 100-105.

47. Susa, A.C., et al., *Charging of Proteins in Native Mass Spectrometry.* J Am Soc Mass Spectrom, 2017. **28**(2): p. 332-340.

48. Harper, C.C., et al., *Direct observation of ion emission from charged aqueous nanodrops: effects on gaseous macromolecular charging.* Chem Sci, 2021. **12**(14): p. 5185-5195.

49. Thinius, M., et al., *Charge Retention/Charge Depletion in ESI-MS: Experimental Evidence.* J Am Soc Mass Spectrom, 2020.

50. Ahadi, E. and L. Konermann, *Surface charge of electrosprayed water nanodroplets: a molecular dynamics study.* J Am Chem Soc, 2010. **132**(32): p. 11270-7.

51. Hogan, C.J., Jr., et al., *Combined charged residue-field emission model of macromolecular electrospray ionization.* Anal Chem, 2009. **81**(1): p. 369-77.

52. Aliyari, E. and L. Konermann, *Formation of Gaseous Proteins via the Ion Evaporation Model (IEM) in Electrospray Mass Spectrometry.* Anal Chem, 2020. **92**(15): p. 10807-10814.

53. Aliyari, E. and L. Konermann, *Formation of Gaseous Peptide Ions from Electrospray Droplets: Competition between the Ion Evaporation Mechanism and Charged Residue Mechanism.* Anal Chem, 2022. **94**(21): p. 7713-7721.

54. Peters, I., H. Metwally, and L. Konermann, *Mechanism of Electrospray Supercharging for Unfolded Proteins: Solvent-Mediated Stabilization of Protonated Sites During Chain Ejection.* Anal Chem, 2019. **91**(10): p. 6943-6952.

55. Metwally, H., Q. Duez, and L. Konermann, *Chain Ejection Model for Electrospray Ionization of Unfolded Proteins: Evidence from Atomistic Simulations and Ion Mobility Spectrometry.* Anal Chem, 2018. **90**(16): p. 10069-10077.

56. Mesleh, M.F., et al., *Structural information from ion mobility measurements: Effects of the long-range potential.* Journal of Physical Chemistry, 1996. **100**(40): p. 16082-16086.

57. Gabelica, V. and E. Marklund, *Fundamentals of ion mobility spectrometry.* Curr Opin Chem Biol, 2018. **42**: p. 51-59.

58. Kanu, A.B., et al., *Ion mobility-mass spectrometry.* J Mass Spectrom, 2008. **43**(1): p. 1-22.

59. Shvartsburg, A.A. and R.D. Smith, *Fundamentals of traveling wave ion mobility spectrometry.* Anal Chem, 2008. **80**(24): p. 9689-99.

60. Eldrid, C., et al., *Gas Phase Stability of Protein Ions in a Cyclic Ion Mobility Spectrometry Traveling Wave Device.* Anal Chem, 2019. **91**(12): p. 7554-7561.

61. Zinnel, N.F., P.J. Pai, and D.H. Russell, *Ion mobility-mass spectrometry (IM-MS) for top-down proteomics: increased dynamic range affords increased sequence coverage.* Anal Chem, 2012. **84**(7): p. 3390-7.

62. Silveira, J.A., et al., *Damping factor links periodic focusing and uniform field ion mobility for accurate determination of collision cross sections.* Anal Chem, 2012. **84**(6): p. 2818-24.

63. Uetrecht, C., et al., *Ion mobility mass spectrometry of proteins and protein assemblies.* Chem Soc Rev, 2010. **39**(5): p. 1633-55.

64. Liu, F.C., S.R. Kirk, and C. Bleiholder, *On the structural denaturation of biological analytes in trapped ion mobility spectrometry - mass spectrometry.* Analyst, 2016. **141**(12): p. 3722-30.

65. Ridgeway, M.E., et al., *Microheterogeneity within conformational states of ubiquitin revealed by high resolution trapped ion mobility spectrometry.* Analyst, 2015. **140**(20): p. 6964-72.

66. Michelmann, K., et al., *Fundamentals of trapped ion mobility spectrometry.* J Am Soc Mass Spectrom, 2015. **26**(1): p. 14-24.

67. Mabrouki, R., et al., *Improving FAIMS sensitivity using a planar geometry with slit interfaces.* J Am Soc Mass Spectrom, 2009. **20**(9): p. 1768-74.

68. Shvartsburg, A.A., et al., *Separation and classification of lipids using differential ion mobility spectrometry.* J Am Soc Mass Spectrom, 2011. **22**(7): p. 1146-55.

69. Reinecke, T., C.N. Naylor, and B.H. Clowers, *Ion multiplexing: Maximizing throughput and signal to noise ratio for ion mobility spectrometry.* TrAC Trends in Analytical Chemistry, 2019. **116**: p. 340-345.

70. Poltash, M.L., et al., *Fourier Transform-Ion Mobility-Orbitrap Mass Spectrometer: A Next-Generation Instrument for Native Mass Spectrometry.* Anal Chem, 2018. **90**(17): p. 10472-10478.

71. Knorr, F.J., et al., *Fourier transform ion mobility spectrometry.* Anal Chem, 1985. **57**(2): p. 402-6.

72. Clowers, B.H., et al., *Hadamard transform ion mobility spectrometry.* Anal Chem, 2006. **78**(1): p. 44-51.

73. Brock, A., N. Rodriguez, and R.N. Zare, *Hadamard Transform Time-of-Flight Mass Spectrometry.* Anal. Chem., 1998. **- 70**(- 18): p. - 3741.

74. Yu, J., et al., *Simulating, Predicting, and Minimizing False Peaks for Hadamard Transform Ion Mobility Spectrometry.* J Am Soc Mass Spectrom, 2020. **31**(9): p. 1957-1964.

75. B. A. Mamyrin, V.I.K., D. V. Shmikk, and V. A. Zagulin, *The mass-reflectron, a new nonmagnetic time-of-flight mass spectrometer with high resolution.* Sov. Phys., 1973. **37**(1): p. 45-48.

76. Campana, J.E., *Time-of-Flight Mass Spectrometry: a Historical Overview.* Instrumentation Science & Technology, 1987. **16**(1): p. 1-14.

77. Kingdon, K.H., *A Method for the Neutralization of Electron Space Charge by Positive Ionization at Very Low Gas Pressures.* Physical Review, 1923. **21**(4): p. 408-418.

78. Knight, R.D., *Storage of ions from laser-produced plasmas.* Applied Physics Letters, 1981. **38**(4): p. 221-223.

79. Marshall, A.G.C., M. B., *FOURIER TRANSFORM ION CYCLOTRON RESONANCE.* CHEMICAL PHYSICS LETTERS, 1974. **25**(2): p. 282-283.

80. Makarov, A., *Electrostatic axially harmonic orbital trapping: a high-performance technique of mass analysis.* Anal Chem, 2000. **72**(6): p. 1156-62.

81. Hu, Q., et al., *The Orbitrap: a new mass spectrometer.* J Mass Spectrom, 2005. **40**(4): p. 430-43.

82. Zubarev, R.A. and A. Makarov, *Orbitrap mass spectrometry.* Anal Chem, 2013. **85**(11): p. 5288-96.

83. Worner, T.P., et al., *Resolving heterogeneous macromolecular assemblies by Orbitrap-based single-particle charge detection mass spectrometry.* Nat Methods, 2020. **17**(4): p. 395-398.

84. Perry, R.H., R.G. Cooks, and R.J. Noll, *Orbitrap mass spectrometry: instrumentation, ion motion and applications.* Mass Spectrom Rev, 2008. **27**(6): p. 661-99.

85. Makarov, A. and E. Denisov, *Dynamics of ions of intact proteins in the Orbitrap mass analyzer.* J Am Soc Mass Spectrom, 2009. **20**(8): p. 1486-95.

86. Elliott, A.G., et al., *Single Particle Analyzer of Mass: A Charge Detection Mass Spectrometer with a Multi-Detector Electrostatic Ion Trap.* Int J Mass Spectrom, 2017. **414**: p. 45-55.

87. Miller, L.M., et al., *Characterization of Classical Vaccines by Charge Detection Mass Spectrometry.* Anal Chem, 2021. **93**(35): p. 11965-11972.

88. Doussineau, T., et al., *Charge Detection Mass Spectrometry for the Characterization of Mass and Surface Area of Composite Nanoparticles.* The Journal of Physical Chemistry C, 2014. **119**(20): p. 10844-10849.

89. Jarrold, M.F., *Applications of Charge Detection Mass Spectrometry in Molecular Biology and Biotechnology.* Chem Rev, 2022. **122**(8): p. 7415-7441.

90. Privalov, P.L. and N.N. Khechinashvili, *A thermodynamic approach to the problem of stabilization of globular protein structure: a calorimetric study.* J Mol Biol, 1974. **86**(3): p. 665-84.

91. Wintrode, P.L., G.I. Makhatadze, and P.L. Privalov, *Thermodynamics of ubiquitin unfolding.* Proteins, 1994. **18**(3): p. 246-53.

92. Ben-Naim, A., *Levinthal's question revisited, and answered.* J Biomol Struct Dyn, 2012. **30**(1): p. 113-24.

93. Vel´azquez-Campoy, A.O., H; Nezami, A.; Muzammil, S.; Freire, E., *Isothermal Titration Calorimetry*, in *Current Protocols in Cell Biology*. 2004, John Wiley & Sons, Inc.

94. Falconer, R.J., B. Schuur, and A.K. Mittermaier, *Applications of isothermal titration calorimetry in pure and applied research from 2016 to 2020.* J Mol Recognit, 2021. **34**(10): p. e2901.

95. Prabhu, N.V. and K.A. Sharp, *Heat capacity in proteins.* Annu Rev Phys Chem, 2005. **56**: p. 521-48.

96. Cooper, A., *Protein Heat Capacity: An Anomaly that Maybe Never Was.* The Journal of Physical Chemistry Letters, 2010. **1**(22): p. 3298-3304.

97. Bakk, A., J.S. Hoye, and A. Hansen, *Heat capacity of protein folding.* Biophys J, 2001. **81**(2): p. 710-4.

98. Ma, C.D., et al., *Modulation of hydrophobic interactions by proximally immobilized ions.* Nature, 2015. **517**(7534): p. 347-50.

99. Galamba, N., *Water's structure around hydrophobic solutes and the iceberg model.* J Phys Chem B, 2013. **117**(7): p. 2153-9.

100. Ben-Naim, A.M.Y., *Effects of Solutes on the Strength of Hydrophobic Interaction and Its Temperature Dependence.* The Journal of Physical Chemistry, 1974. **78**(2): p. 170-175.

101. Frank, H.S. and M.W. Evans, *Free Volume and Entropy in Condensed Systems III. Entropy in Binary Liquid Mixtures; Partial Molal Entropy in Dilute Solutions; Structure and Thermodynamics in Aqueous Electrolytes.* The Journal of Chemical Physics, 1945. **13**(11): p. 507-532.

102. Grabowska, J., A. Kuffel, and J. Zielkiewicz, *Revealing the Frank-Evans "Iceberg" Structures within the Solvation Layer around Hydrophobic Solutes.* J Phys Chem B, 2021. **125**(6): p. 1611-1617.

103. Privalov, P.L., *Cold denaturation of proteins.* Crit Rev Biochem Mol Biol, 1990. **25**(4): p. 281-305.

104. Edwards, A.A., et al., *Altered enthalpy-entropy compensation in picomolar transition state analogues of human purine nucleoside phosphorylase.* Biochemistry, 2009. **48**(23): p. 5226-38.

105. Liu, L., C. Yang, and Q.X. Guo, *A study on the enthalpy-entropy compensation in protein unfolding.* Biophysical Chemistry, 2000. **84**(3): p. 239-251.

106. Breiten, B., et al., *Water networks contribute to enthalpy/entropy compensation in protein-ligand binding.* J Am Chem Soc, 2013. **135**(41): p. 15579-84.

107. Douglas, J.F., J. Dudowicz, and K.F. Freed, *Crowding induced self-assembly and enthalpy-entropy compensation.* Phys Rev Lett, 2009. **103**(13): p. 135701.

108. Dragan, A.I., C.M. Read, and C. Crane-Robinson, *Enthalpy-entropy compensation: the role of solvation.* Eur Biophys J, 2017. **46**(4): p. 301-308.

109. Lumry, R. and S. Rajender, *Enthalpy-entropy compensation phenomena in water solutions of proteins and small molecules: a ubiquitous property of water.* Biopolymers, 1970. **9**(10): p. 1125-227.

110. El-Baba, T.J., et al., *Melting Proteins: Evidence for Multiple Stable Structures upon Thermal Denaturation of Native Ubiquitin from Ion Mobility Spectrometry-Mass Spectrometry Measurements.* J Am Chem Soc, 2017. **139**(18): p. 6306-6309.

111. Kohler, M., et al., *Temperature-controlled electrospray ionization mass spectrometry as a tool to study collagen homo- and heterotrimers.* Chem Sci, 2019. **10**(42): p. 9829-9835.

112. Braig, K., et al., *The Crystal-Structure of the Bacterial Chaperonin Groel at 2.8-Angstrom.* Nature, 1994. **371**(6498): p. 578-586.

113. Boisvert, D.C.W., J.; Otwinowski, Z.; Norwich, A. L.; Sigler, P. B., *The 2.4 A crystal structure of the bacterial chaperon in GroEL complexed with ATPyS.* Nat. Struct. Biol., 1996. **3**(2): p. 170-177.

114. Xu, Z., A.L. Horwich, and P.B. Sigler, *The crystal structure of the asymmetric GroEL-GroES-(ADP)7 chaperonin complex.* Nature, 1997. **388**(6644): p. 741-50.

115. Rye, H.S., et al., *Distinct actions of cis and trans ATP within the double ring of the chaperonin GroEL.* Nature, 1997. **388**(6644): p. 792-798.

116. Roh, S.H., et al., *Subunit conformational variation within individual GroEL oligomers resolved by Cryo-EM.* Proc Natl Acad Sci U S A, 2017. **114**(31): p. 8259-8264.

117. Fei, X., et al., *Formation and structures of GroEL:GroES2 chaperonin footballs, the protein-folding functional form.* Proc Natl Acad Sci U S A, 2014. **111**(35): p. 12775-80.

118. Yang, D., X. Ye, and G.H. Lorimer, *Symmetric GroEL:GroES2 complexes are the protein-folding functional form of the chaperonin nanomachine.* Proc Natl Acad Sci U S A, 2013. **110**(46): p. E4298-305.

119. Horwich, A.L., G.W. Farr, and W.A. Fenton, *GroEL-GroES-mediated protein folding.* Chem Rev, 2006. **106**(5): p. 1917-30.

120. Yifrach, O. and A. Horovitz, *Allosteric control by ATP of non-folded protein binding to GroEL.* J Mol Biol, 1996. **255**(3): p. 356-61.

121. Yifrach, O. and A. Horovitz, *Nested Cooperativity in the Atpase Activity of the Oligomeric Chaperonin Groel.* Biochemistry, 1995. **34**(16): p. 5303-5308.

122. Yifrach, O. and A. Horovitz, *Two lines of allosteric communication in the oligomeric chaperonin GroEL are revealed by the single mutation Arg196-->Ala.* J Mol Biol, 1994. **243**(3): p. 397-401.

123. Todd, M.J., P.V. Viitanen, and G.H. Lorimer, *Dynamics of the chaperonin ATPase cycle: implications for facilitated protein folding.* Science, 1994. **265**(5172): p. 659-66.

124. Todd, M.J., P.V. Viitanen, and G.H. Lorimer, *Hydrolysis of Adenosine 5'-Triphosphate by Escherichia-Coli Groel - Effects of Groes and Potassium-Ion.* Biochemistry, 1993. **32**(33): p. 8560-8567.

125. Monod, J., J. Wyman, and J.P. Changeux, *On the Nature of Allosteric Transitions: A Plausible Model.* J Mol Biol, 1965. **12**: p. 88-118.

126. Ackers, G.K. and M.L. Johnson, *Linked Functions in Allosteric Proteins - Extension of the Concerted (Mwc) Model for Ligand-Linked Subunit Assembly and Its Application to Human Hemoglobins.* Journal of Molecular Biology, 1981. **147**(4): p. 559-582.

127. Koshland, D.E., Jr., G. Nemethy, and D. Filmer, *Comparison of experimental binding data and theoretical models in proteins containing subunits.* Biochemistry, 1966. **5**(1): p. 365-85.

128. Cho, S.S., et al., *Entropic Stabilization of Proteins by TMAO.* The Journal of Physical Chemistry B, 2011. **115**(45): p. 13401-13407.

129. Liao, Y.T., et al., *Trimethylamine N-oxide stabilizes proteins via a distinct mechanism compared with betaine and glycine.* Proc Natl Acad Sci U S A, 2017. **114**(10): p. 2479-2484.

130. Mukaiyama, A., et al., *Osmolyte effect on the stability and folding of a hyperthermophilic protein.* Proteins, 2008. **71**(1): p. 110-8.

131. Ganguly, P., et al., *Protein Stability in TMAO and Mixed Urea-TMAO Solutions.* J Phys Chem B, 2020. **124**(29): p. 6181-6197.

132. Baskakov, I. and D.W. Bolen, *Forcing Thermodynamically Unfolded Proteins to Fold.* Journal of Biological Chemistry, 1998. **273**(9): p. 4831-4834.

133. Levine, Z.A., et al., *Regulation and aggregation of intrinsically disordered peptides.* Proc Natl Acad Sci U S A, 2015. **112**(9): p. 2758-63.

134. Yancey, P.H. and G.N. Somero, *Methylamine Osmoregulatory Solutes of Elasmobranch Fishes Counteract Urea Inhibition of Enzymes.* Journal of Experimental Zoology, 1980. **212**(2): p. 205-213.

135. Wang, A. and D.W. Bolen, *A naturally occurring protective system in urea-rich cells: mechanism of osmolyte protection of proteins against urea denaturation.* Biochemistry, 1997. **36**(30): p. 9101-8.

136. Canchi, D.R., et al., *Molecular mechanism for the preferential exclusion of TMAO from protein surfaces.* J Phys Chem B, 2012. **116**(40): p. 12095-104.

137. Hunger, J., et al., *Water-mediated interactions between trimethylamine-N-oxide and urea.* Phys Chem Chem Phys, 2015. **17**(1): p. 298-306.

138. Bolen, D.W. and G.D. Rose, *Structure and energetics of the hydrogen-bonded backbone in protein folding.* Annu Rev Biochem, 2008. **77**: p. 339-62.

139. Auton, M. and D.W. Bolen, *Predicting the energetics of osmolyte-induced protein folding/unfolding.* Proc Natl Acad Sci U S A, 2005. **102**(42): p. 15065-8.

140. Attri, P., P. Venkatesu, and M.J. Lee, *Influence of osmolytes and denaturants on the structure and enzyme activity of alpha-chymotrypsin.* J Phys Chem B, 2010. **114**(3): p. 1471-8.

141. O'Brien, E.P., et al., *Interactions between hydrophobic and ionic solutes in aqueous guanidinium chloride and urea solutions: Lessons for protein denaturation mechanism.* Journal of the American Chemical Society, 2007. **129**(23): p. 7346-7353.

142. Tobi, D., R. Elber, and D. Thirumalai, *The dominant interaction between peptide and urea is electrostatic in nature: A molecular dynamics simulation study.* Biopolymers, 2003. **68**(3): p. 359-369.

143. Klimov, D.K., J.E. Straub, and D. Thirumalai, *Aqueous urea solution destabilizes A beta(16-22) oligomers.* Proceedings of the National Academy of Sciences of the United States of America, 2004. **101**(41): p. 14760-14765.

144. Linhananta, A., S. Hadizadeh, and S.S. Plotkin, *An effective solvent theory connecting the underlying mechanisms of osmolytes and denaturants for protein stability.* Biophys J, 2011. **100**(2): p. 459-68.

145. Frank, H.S. and F. Franks, *Structural Approach to the Solvent Power of Water for Hydrocarbons; Urea as a Structure Breaker.* The Journal of Chemical Physics, 1968. **48**(10): p. 4746-4757.

146. Canchi, D.R. and A.E. Garcia, *Cosolvent effects on protein stability.* Annu Rev Phys Chem, 2013. **64**: p. 273-93.

147. Ladbury, J.E., *Just add water! The effect of water on the specificity of protein-ligand binding sites and its potential application to drug design.* Chemistry & Biology, 1996. **3**(12): p. 973-980.

148. Bogan, A.A. and K.S. Thorn, *Anatomy of hot spots in protein interfaces.* J Mol Biol, 1998. **280**(1): p. 1-9.

149. Papoian, G.A., et al., *Water in protein structure prediction.* Proc Natl Acad Sci U S A, 2004. **101**(10): p. 3352-7.

150. Levy, Y. and J.N. Onuchic, *Water and proteins: a love-hate relationship.* Proc Natl Acad Sci U S A, 2004. **101**(10): p. 3325-6.

151. Levy, Y. and J.N. Onuchic, *Water Mediation in Protein Folding and Molecular Recognition*, in *Annual Review of Biophysics and Biomolecular Structure*. 2006, Annual Reviews: Palo Alto. p. 389-415.

152. Nandi, N., K. Bhattacharyya, and B. Bagchi, *Dielectric relaxation and solvation dynamics of water in complex chemical and biological systems.* Chem Rev, 2000. **100**(6): p. 2013-46.

153. Pal, S.K., J. Peon, and A.H. Zewail, *Biological water at the protein surface: Dynamical solvation probed directly with femtosecond resolution.* Proceedings of the National Academy of Sciences of the United States of America, 2002. **99**(4): p. 1763-1768.

154. Halle, B., *Protein hydration dynamics in solution: a critical survey.* Philos Trans R Soc Lond B Biol Sci, 2004. **359**(1448): p. 1207-23; discussion 1223-4, 1323-8.

155. Rodier, F., et al., *Hydration of protein-protein interfaces.* Proteins, 2005. **60**(1): p. 36-45.

156. Nucci, N.V., M.S. Pometun, and A.J. Wand, *Mapping the hydration dynamics of ubiquitin.* J Am Chem Soc, 2011. **133**(32): p. 12326-9.

157. Duboue-Dijon, E. and D. Laage, *Comparative study of hydration shell dynamics around a hyperactive antifreeze protein and around ubiquitin.* J Chem Phys, 2014. **141**(22): p. 22D529.

158. Kempf, B. and E. Bremer, *Uptake and synthesis of compatible solutes as microbial stress responses to high-osmolality environments.* Archives of Microbiology, 1998. **170**(5): p. 319-330.

159. Yancey, P.H., et al., *Trimethylamine oxide counteracts effects of hydrostatic pressure on proteins of deep-sea teleosts.* J Exp Zool, 2001. **289**(3): p. 172-6.

160. Hunger, J., et al., *Complex formation in aqueous trimethylamine-N-oxide (TMAO) solutions.* J Phys Chem B, 2012. **116**(16): p. 4783-95.

161. Zou, Q., et al., *The molecular mechanism of stabilization of proteins by TMAO and its ability to counteract the effects of urea.* J Am Chem Soc, 2002. **124**(7): p. 1192-202.

162. Sahle, C.J., et al., *Influence of TMAO and urea on the structure of water studied by inelastic X-ray scattering.* Phys Chem Chem Phys, 2016. **18**(24): p. 16518-26.

163. Pincus, D.L., C. Hyeon, and D. Thirumalai, *Effects of trimethylamine N-oxide (TMAO) and crowding agents on the stability of RNA hairpins.* J Am Chem Soc, 2008. **130**(23): p. 7364-72.

164. Ma, J., I.M. Pazos, and F. Gai, *Microscopic insights into the protein-stabilizing effect of trimethylamine N-oxide (TMAO).* Proc Natl Acad Sci U S A, 2014. **111**(23): p. 8476-81.

165. Yancey, P., et al., *Living with water stress: evolution of osmolyte systems.* Science, 1982. **217**(4566): p. 1214-1222.

166. Meersman, F., et al., *Counteraction of urea by trimethylamine N-oxide is due to direct interaction.* Biophys J, 2009. **97**(9): p. 2559-66.

167. Celinski, S.A. and J.M. Scholtz, *Osmolyte effects on helix formation in peptides and the stability of coiled-coils.* Protein Sci, 2002. **11**(8): p. 2048-51.

168. Mazur, K., I.A. Heisler, and S.R. Meech, *THz spectra and dynamics of aqueous solutions studied by the ultrafast optical Kerr effect.* J Phys Chem B, 2011. **115**(11): p. 2563-73.

169. Knake, L., et al., *Solvation Dynamics of Trimethylamine N-Oxide in Aqueous Solution Probed by Terahertz Spectroscopy.* J Phys Chem B, 2015. **119**(43): p. 13842-51.

170. Arsiccio, A. and J.E. Shea, *Pressure Unfolding of Proteins: New Insights into the Role of Bound Water.* J Phys Chem B, 2021. **125**(30): p. 8431-8442.

171. Batchelor, J.D., et al., *Impact of protein denaturants and stabilizers on water structure.* J Am Chem Soc, 2004. **126**(7): p. 1958-61.

172. Rezus, Y.L. and H.J. Bakker, *Effect of urea on the structural dynamics of water.* Proc Natl Acad Sci U S A, 2006. **103**(49): p. 18417-20.

173. Soper, A.K., E.W. Castner, and A. Luzar, *Impact of urea on water structure: a clue to its properties as a denaturant?* Biophysical Chemistry, 2003. **105**(2-3): p. 649-666.

174. Sagle, L.B., et al., *Investigating the hydrogen-bonding model of urea denaturation.* J Am Chem Soc, 2009. **131**(26): p. 9304-10.

175. Wallqvist, A., D.G. Covell, and D. Thirumalai, *Hydrophobic interactions in aqueous urea solutions with implications for the mechanism of protein denaturation.* Journal of the American Chemical Society, 1998. **120**(2): p. 427-428.

176. Servage, K.A., et al., *Cryogenic Ion Mobility-Mass Spectrometry: Tracking Ion Structure from Solution to the Gas Phase.* Acc Chem Res, 2016. **49**(7): p. 1421-8.

177. Silveira, J.A., et al., *From solution to the gas phase: stepwise dehydration and kinetic trapping of substance P reveals the origin of peptide conformations.* J Am Chem Soc, 2013. **135**(51): p. 19147-53.

178. Servage, K.A., et al., *From solution to gas phase: the implications of intramolecular interactions on the evaporative dynamics of substance P during electrospray ionization.* J Phys Chem B, 2015. **119**(13): p. 4693-8.

179. Fort, K.L., et al., *From solution to the gas phase: factors that influence kinetic trapping of substance P in the gas phase.* J Phys Chem B, 2014. **118**(49): p. 14336-44.

180. Suvas, S., *Role of Substance P Neuropeptide in Inflammation, Wound Healing, and Tissue Homeostasis.* J Immunol, 2017. **199**(5): p. 1543-1552.

181. Silveira, J.A., et al., *Cryogenic ion mobility-mass spectrometry captures hydrated ions produced during electrospray ionization.* J Phys Chem A, 2013. **117**(5): p. 953-61.

182. Servage, K.A., et al., *Water-Mediated Dimerization of Ubiquitin Ions Captured by Cryogenic Ion Mobility-Mass Spectrometry.* J Phys Chem Lett, 2015. **6**(24): p. 4947-51.

183. Hebert, M.J. and D.H. Russell, *Hydration of Guanidinium Ions: An Experimental Search for Like-Charged Ion Pairs.* J Phys Chem Lett, 2019. **10**(6): p. 1349-1354.

184. May, J.C. and D.H. Russell, *A mass-selective variable-temperature drift tube ion mobility-mass spectrometer for temperature dependent ion mobility studies.* J Am Soc Mass Spectrom, 2011. **22**(7): p. 1134-45.

185. Kim, D., et al., *Ions from Solution to the Gas Phase: A Molecular Dynamics Simulation of the Structural Evolution of Substance P during Desolvation of Charged Nanodroplets Generated by Electrospray Ionization.* J Am Chem Soc, 2017. **139**(8): p. 2981-2988.

186. Conant, C.R., et al., *Substance P in the Gas Phase: Conformational Changes and Dissociations Induced by Collisional Activation in a Drift Tube.* J Am Soc Mass Spectrom, 2019. **30**(6): p. 932-945.

187. McLean, J.A., *The mass-mobility correlation redux: the conformational landscape of anhydrous biomolecules.* J Am Soc Mass Spectrom, 2009. **20**(10): p. 1775-81.

188. Lyu, J., et al., *Discovery of Potent Charge-Reducing Molecules for Native Ion Mobility Mass Spectrometry Studies.* Anal Chem, 2020. **92**(16): p. 11242-11249.

189. Su, Z. and C.L. Dias, *Individual and combined effects of urea and trimethylamine N-oxide (TMAO) on protein structures.* Journal of Molecular Liquids, 2019. **293**.

190. Hong, J. and S. Xiong, *TMAO-Protein Preferential Interaction Profile Determines TMAO's Conditional In Vivo Compatibility.* Biophys J, 2016. **111**(9): p. 1866-1875.

191. Rueger, M., et al., *Self-association of the neuroregulatory peptide substance P and Its C-terminal sequences.* Biopolymers, 1984. **23**(4): p. 747-58.

192. Lopez, C.F., R.K. Darst, and P.J. Rossky, *Mechanistic elements of protein cold denaturation.* J Phys Chem B, 2008. **112**(19): p. 5961-7.

193. Matysiak, S., P.G. Debenedetti, and P.J. Rossky, *Role of hydrophobic hydration in protein stability: a 3D water-explicit protein model exhibiting cold and heat denaturation.* J Phys Chem B, 2012. **116**(28): p. 8095-104.

194. Krone, M.G., et al., *Role of water in mediating the assembly of Alzheimer amyloid-beta Abeta16-22 protofilaments.* J Am Chem Soc, 2008. **130**(33): p. 11066-72.

195. Shi, L., et al., *"Wet" Versus "Dry" Folding of Polyproline.* J Am Soc Mass Spectrom, 2016. **27**(6): p. 1037-47.

196. Raab, S.A., et al., *Protons Are Fast and Smart; Proteins Are Slow and Dumb: On the Relationship of Electrospray Ionization Charge States and Conformations.* J Am Soc Mass Spectrom, 2021. **32**(7): p. 1553-1561.

197. El-Baba, T.J., et al., *Solvent Mediation of Peptide Conformations: Polyproline Structures in Water, Methanol, Ethanol, and 1-Propanol as Determined by Ion Mobility Spectrometry-Mass Spectrometry.* J Am Soc Mass Spectrom, 2019. **30**(1): p. 77-84.

198. Yan, X., R.M. Bain, and R.G. Cooks, *Organic Reactions in Microdroplets: Reaction Acceleration Revealed by Mass Spectrometry.* Angew Chem Int Ed Engl, 2016. **55**(42): p. 12960-12972.

199. Wei, Z., et al., *Accelerated Reaction Kinetics in Microdroplets: Overview and Recent Developments.* Annu Rev Phys Chem, 2020. **71**: p. 31-51.

200. Saunders, A.J., et al., *Osmolyte-induced changes in protein conformational equilibria.* Biopolymers, 2000. **53**(4): p. 293-307.

201. Jahan, I. and S.M. Nayeem, *Effect of Osmolytes on Conformational Behavior of Intrinsically Disordered Protein alpha-Synuclein.* Biophys J, 2019. **117**(10): p. 1922-1934.

202. Gault, J., et al., *Mass Spectrometry Reveals the Direct Action of a Chemical Chaperone.* J Phys Chem Lett, 2018. **9**(14): p. 4082-4086.

203. Bolen, D.W. and I.V. Baskakov, *The osmophobic effect: natural selection of a thermodynamic force in protein folding.* J Mol Biol, 2001. **310**(5): p. 955-63.

204. Graziano, G., *A rationale for the contrasting activity (towards globular proteins) of tert-butyl alcohol and trimethylamine N-oxide.* Phys Chem Chem Phys, 2012. **14**(37): p. 13088-94.

205. Davidovic, M., et al., *Protein Cold Denaturation as Seen From the Solvent.* Journal of the American Chemical Society, 2009. **131**(3): p. 1025-1036.

206. Liu, S. and B.C. Gibb, *High-definition self-assemblies driven by the hydrophobic effect: synthesis and properties of a supramolecular nanocapsule.* Chemical Communications, 2008(32).

207. Yamashita, M. and J.B. Fenn, *Electrospray Ion-Source - Another Variation on the Free-Jet Theme.* Journal of Physical Chemistry, 1984. **88**(20): p. 4451-4459.

208. Yamashita, M. and J.B. Fenn, *Negative-Ion Production with the Electrospray Ion-Source.* Journal of Physical Chemistry, 1984. **88**(20): p. 4671-4675.

209. Yin, S. and J.A. Loo, *Top-Down Mass Spectrometry of Supercharged Native Protein-Ligand Complexes.* Int J Mass Spectrom, 2011. **300**(2-3): p. 118-122.

210. Nshanian, M., et al., *Enhancing Sensitivity of Liquid Chromatography-Mass Spectrometry of Peptides and Proteins Using Supercharging Agents.* Int J Mass Spectrom, 2018. **427**: p. 157-164.

211. Konermann, L., *Addressing a Common Misconception: Ammonium Acetate as Neutral pH "Buffer" for Native Electrospray Mass Spectrometry.* J Am Soc Mass Spectrom, 2017. **28**(9): p. 1827-1835.

212. Limbach, P.A., P.F. Crain, and J.A. McCloskey, *Molecular mass measurement of intact ribonucleic acids via electrospray ionization quadrupole mass spectrometry.* J Am Soc Mass Spectrom, 1995. **6**(1): p. 27-39.

213. Pacholarz, K.J., et al., *Mass spectrometry based tools to investigate protein-ligand interactions for drug discovery.* Chem Soc Rev, 2012. **41**(11): p. 4335-55.

214. Ruotolo, B.T., et al., *Ion mobility-mass spectrometry analysis of large protein complexes.* Nat Protoc, 2008. **3**(7): p. 1139-52.

215. Hernandez, H. and C.V. Robinson, *Determining the stoichiometry and interactions of macromolecular assemblies from mass spectrometry.* Nat Protoc, 2007. **2**(3): p. 715-26.

216. Heck, A.J. and R.H. Van Den Heuvel, *Investigation of intact protein complexes by mass spectrometry.* Mass Spectrom Rev, 2004. **23**(5): p. 368-89.

217. Stiving, A.Q., et al., *Collision Cross Sections of Charge-Reduced Proteins and Protein Complexes: A Database for Collision Cross Section Calibration.* Anal Chem, 2020. **92**(6): p. 4475-4483.

218. Zhou, M., S. Dagan, and V.H. Wysocki, *Impact of charge state on gas-phase behaviors of noncovalent protein complexes in collision induced dissociation and surface induced dissociation.* Analyst, 2013. **138**(5): p. 1353-62.

219. Pacholarz, K.J. and P.E. Barran, *Use of a charge reducing agent to enable intact mass analysis of cysteine-linked antibody-drug-conjugates by native mass spectrometry.* EuPA Open Proteom, 2016. **11**: p. 23-27.

220. Pagel, K., et al., *Alternate dissociation pathways identified in charge-reduced protein complex ions.* Anal Chem, 2010. **82**(12): p. 5363-72.

221. Mehmood, S., et al., *Charge reduction stabilizes intact membrane protein complexes for mass spectrometry.* J Am Chem Soc, 2014. **136**(49): p. 17010-2.

222. Hall, Z., et al., *Charge-state dependent compaction and dissociation of protein complexes: insights from ion mobility and molecular dynamics.* J Am Chem Soc, 2012. **134**(7): p. 3429-38.

223. Ahadi, E. and L. Konermann, *Ejection of solvated ions from electrosprayed methanol/water nanodroplets studied by molecular dynamics simulations.* J Am Chem Soc, 2011. **133**(24): p. 9354-63.

224. Konermann, L., et al., *Unraveling the mechanism of electrospray ionization.* Anal Chem, 2013. **85**(1): p. 2-9.

225. Iribarne, J.V., *On the evaporation of small ions from charged droplets.* The Journal of Chemical Physics, 1976. **64**(6).

226. Loscertales, I.G. and J. Fernández de la Mora, *Experiments on the kinetics of field evaporation of small ions from droplets.* The Journal of Chemical Physics, 1995. **103**(12): p. 5041-5060.

227. delaMora, J.F., *On the outcome of the coulombic fission of a charged isolated drop.* Journal of Colloid and Interface Science, 1996. **178**(1): p. 209-218.

228. Martin, L.M. and L. Konermann, *Enhancing Protein Electrospray Charge States by Multivalent Metal Ions: Mechanistic Insights from MD Simulations and Mass Spectrometry Experiments.* J Am Soc Mass Spectrom, 2020. **31**(1): p. 25-33.

229. Consta, S., *Fragmentation reactions of charged aqueous clusters.* Journal of Molecular Structure-Theochem, 2002. **591**: p. 131-140.

230. Hogan, C.J., Jr. and J.F. de la Mora, *Ion mobility measurements of nondenatured 12-150 kDa proteins and protein multimers by tandem differential mobility analysis-mass spectrometry (DMA-MS).* J Am Soc Mass Spectrom, 2011. **22**(1): p. 158-72.

231. Hogan, C.J., Jr., et al., *Charge carrier field emission determines the number of charges on native state proteins in electrospray ionization.* J Am Chem Soc, 2008. **130**(22): p. 6926-7.

232. Marty, M.T., et al., *Bayesian deconvolution of mass and ion mobility spectra: from binary interactions to polydisperse ensembles.* Anal Chem, 2015. **87**(8): p. 4370-6.

233. Poltash, M.L., et al., *Development and Evaluation of a Reverse-Entry Ion Source Orbitrap Mass Spectrometer.* J Am Soc Mass Spectrom, 2019. **30**(1): p. 192-198.

234. McCabe, J.W., et al., *First-Principles Collision Cross Section Measurements of Large Proteins and Protein Complexes.* Anal Chem, 2020. **92**(16): p. 11155-11163.

235. Metwally, H., et al., *Mechanism of Protein Supercharging by Sulfolane and m-Nitrobenzyl Alcohol: Molecular Dynamics Simulations of the Electrospray Process.* Anal Chem, 2016. **88**(10): p. 5345-54.

236. Allen, S.J., A.M. Schwartz, and M.F. Bush, *Effects of polarity on the structures and charge states of native-like proteins and protein complexes in the gas phase.* Anal Chem, 2013. **85**(24): p. 12055-61.

237. Foley, E.D.B., et al., *On the mechanism of protein supercharging in electrospray ionisation mass spectrometry: Effects on charging of additives with short- and long-chain alkyl constituents with carbonate and sulphite terminal groups.* Anal Chim Acta X, 2019. **1**: p. 100004.

238. Tang, M., et al., *Comparison of Gas-Phase Basicities and Ion-Molecule Reactions of Aminobenzoic Acids.* Journal of Mass Spectrometry, 1995. **30**(7): p. 977-984.

239. Catalina, M.I., et al., *Decharging of globular proteins and protein complexes in electrospray.* Chemistry, 2005. **11**(3): p. 960-8.

240. Foreman, D.J. and S.A. McLuckey, *Recent Developments in Gas-Phase Ion/Ion Reactions for Analytical Mass Spectrometry.* Anal Chem, 2020. **92**(1): p. 252-266.

241. Stutzman, J.R., et al., *Microdroplet Fusion Chemistry for Charge State Reduction of Synthetic Polymers via Bipolar Dual Spray with Anionic Reagents.* J Am Soc Mass Spectrom, 2019. **30**(9): p. 1742-1749.

242. Davidson, K.L., et al., *Nonspecific aggregation in native electrokinetic nanoelectrospray ionization.* International Journal of Mass Spectrometry, 2017. **420**: p. 35-42.

243. Xia, Z. and E.R. Williams, *Effect of droplet lifetime on where ions are formed in electrospray ionization.* Analyst, 2018. **144**(1): p. 237-248.

244. Konermann, L., E.A. Silva, and O.F. Sogbein, *Electrochemically induced pH changes resulting in protein unfolding in the ion source of an electrospray mass spectrometer.* Anal Chem, 2001. **73**(20): p. 4836-44.

245. Benesch, J.L.P., F. Sobott, and C.V. Robinson, *Thermal dissociation of multimeric protein complexes by using nanoelectrospray mass spectrometry.* Analytical Chemistry, 2003. **75**(10): p. 2208-2214.

246. Snyder, D.T., S.R. Harvey, and V.H. Wysocki, *Surface-induced Dissociation Mass Spectrometry as a Structural Biology Tool.* Chem Rev, 2022. **122**(8): p. 7442-7487.

247. Stiving, A.Q., et al., *Surface-Induced Dissociation: An Effective Method for Characterization of Protein Quaternary Structure.* Anal Chem, 2019. **91**(1): p. 190-209.

248. Consta, S., *Manifestation of Rayleigh instability in droplets containing multiply charged macroions.* J Phys Chem B, 2010. **114**(16): p. 5263-8.

249. Consta, S. and V. Kwan, *Effect of droplet size and counterions on the spatial distribution of ions.* 2019.

250. Boisvert, D.C., et al., *The 2.4 Å crystal structure of the bacterial chaperonin GroEL complexed with ATPγS.* Nature Structural Biology, 1996. **3**(2): p. 170-177.

251. Horwich, A.L., G.W. Farr, and W.A. Fenton, *GroEL−GroES-Mediated Protein Folding.* Chemical Reviews, 2006. **106**(5): p. 1917-1930.

252. Ranson, N.A., et al., *Allosteric signaling of ATP hydrolysis in GroEL–GroES complexes.* Nature Structural & Molecular Biology, 2006. **13**(2): p. 147-152.

253. Saibil, H.R., et al., *Structure and Allostery of the Chaperonin GroEL.* Journal of Molecular Biology, 2013. **425**(9): p. 1476-1487.

254. Sot, B., et al., *GroEL stability and function. Contribution of the ionic interactions at the inter-ring contact sites.* J Biol Chem, 2003. **278**(34): p. 32083-90.

255. Lars, S., et al., *Conformational Sampling and Nucleotide-Dependent Transitions of the GroEL Subunit Probed by Unbiased Molecular Dynamics Simulations.* PLoS Comput Biol 2011. **7**(3): p. e1002004.

256. Xu, Z., A.L. Horwich, and P.B. Sigler, *The crystal structure of the asymmetric GroEL–GroES–(ADP)7 chaperonin complex.* Nature, 1997. **388**(6644): p. 741-750.

257. Roh, S.-H., et al., *Subunit conformational variation within individual GroEL oligomers resolved by Cryo-EM.* Proceedings of the National Academy of Sciences, 2017: p. 201704725.

258. Viitanen, P.V., et al., *Chaperonin-facilitated refolding of ribulose bisphosphate carboxylase and ATP hydrolysis by chaperonin 60 (groEL) are potassium dependent.* Biochemistry, 1990. **29**(24): p. 5665-5671.

259. Lin, Z. and H.S. Rye, *GroEL-mediated protein folding: making the impossible, possible.* Critical reviews in biochemistry and molecular biology, 2006. **41**(4): p. 211-239.

260. Lorimer, G., *Protein folding Folding with a two-stroke motor.* Nature, 1997. **388**(6644): p. 720-721.

261. Grason, J.P., J.S. Gresham, and G.H. Lorimer, *Setting the chaperonin timer: A two-stroke, two-speed, protein machine.* Proceedings of the National Academy of Sciences, 2008. **105**(45): p. 17339.

262. Rye, H.S., et al., *Distinct actions of cis and trans ATP within the double ring of the chaperonin GroEL.* Nature, 1997. **388**(6644): p. 792-798.

263. Yang, D., X. Ye, and G.H. Lorimer, *Symmetric GroEL:GroES₂ complexes are the protein-folding functional form of the chaperonin nanomachine.* Proceedings of the National Academy of Sciences, 2013. **110**(46): p. E4298.

264. Bigman, L.S. and A. Horovitz, *Reconciling the controversy regarding the functional importance of bullet- and football-shaped GroE complexes.* J Biol Chem, 2019. **294**(37): p. 13527-13529.

265. Taguchi, H., *Reaction Cycle of Chaperonin GroEL via Symmetric "Football" Intermediate.* Journal of Molecular Biology, 2015. **427**(18): p. 2912-2918.

266. Yaginuma, H., et al., *Diversity in ATP concentrations in a single bacterial cell population revealed by quantitative single-cell imaging.* Scientific Reports, 2014. **4**(1): p. 6522.

267. Horovitz, A., et al., *Chaperonin Mechanisms: Multiple and (Mis)Understood?* Annual Review of Biophysics, 2022.

268. Rostom, A.A. and C.V. Robinson, *Detection of the Intact GroEL Chaperonin Assembly by Mass Spectrometry.* Journal of the American Chemical Society, 1999. **121**(19): p. 4718-4719.

269. Robinson, C.V., et al., *Conformation of GroEL-bound α-lactalbumin probed by mass spectrometry.* Nature, 1994. **372**(6507): p. 646-651.

270. Clemmer, D.E., D.H. Russell, and E.R. Williams, *Characterizing the Conformationome: Toward a Structural Understanding of the Proteome.* Accounts of Chemical Research, 2017. **50**(3): p. 556-560.

271. McCabe, J.W., et al., *THE IMS PARADOX: A PERSPECTIVE ON STRUCTURAL ION MOBILITY-MASS SPECTROMETRY.* Mass Spectrometry Reviews, 2021. **40**(3): p. 280-305.

272. Dyachenko, A., et al., *Allosteric mechanisms can be distinguished using structural mass spectrometry.* Proceedings of the National Academy of Sciences, 2013. **110**(18): p. 7235.

273. van Duijn, E., et al., *Monitoring macromolecular complexes involved in the chaperonin-assisted protein folding cycle by mass spectrometry.* Nature Methods, 2005. **2**(5): p. 371-376.

274. McCabe, J.W., et al., *Variable-Temperature Electrospray Ionization for Temperature-Dependent Folding/Refolding Reactions of Proteins and Ligand Binding.* Analytical Chemistry, 2021. **93**(18): p. 6924-6931.

275. Shirzadeh, M., et al., *Structural Analysis of the Effect of a Dual-FLAG Tag on Transthyretin.* Biochemistry, 2020. **59**(9): p. 1013-1022.

276. Privalov, P.L., *Cold Denaturation of Protein.* Critical Reviews in Biochemistry and Molecular Biology, 1990. **25**(4): p. 281-306.

277. Woodall, D.W., et al., *Melting of Hemoglobin in Native Solutions as measured by IMS-MS.* Analytical Chemistry, 2020. **92**(4): p. 3440-3446.

278. Marchand, A., et al., *Studying biomolecular folding and binding using temperature-jump mass spectrometry.* Nature Communications, 2020. **11**(1): p. 566.

279. Lee, S.-W., et al., *Freeze-Dried Biomolecules: FT-ICR Studies of the Specific Solvation of Functional Groups and Clathrate Formation Observed by the Slow Evaporation of Water from Hydrated Peptides and Model Compounds in the Gas Phase.* Journal of the American Chemical Society, 1998. **120**(45): p. 11758-11765.

280. Clare, D.K., et al., *An expanded protein folding cage in the GroEL-gp31 complex.* J Mol Biol, 2006. **358**(3): p. 905-11.

281. Donald, L.J., et al., *Multiple equilibria of the Escherichia coli chaperonin GroES revealed by mass spectrometry.* Protein Science, 2005. **14**(5): p. 1375-1379.

282. Raab, S.A., et al., *Evidence for Many Unique Solution Structures for Chymotrypsin Inhibitor 2: A Thermodynamic Perspective Derived from vT-ESI-IMS-MS Measurements.* Journal of the American Chemical Society, 2020. **142**(41): p. 17372-17383.

283. Boudker, O., M.J. Todd, and E. Freire, *The structural stability of the co-chaperonin GroES.* Journal of molecular biology, 1997. **272**(5): p. 770-779.

284. Geels, R.B.J., et al., *Thermal activation of the co-chaperonins GroES and gp31 probed by mass spectrometry.* Rapid Communications in Mass Spectrometry, 2008. **22**(22): p. 3633-3641.

285. Dyachenko, A., S. Tamara, and A.J.R. Heck, *Distinct Stabilities of the Structurally Homologous Heptameric Co-Chaperonins GroES and gp31.* Journal of The American Society for Mass Spectrometry, 2019. **30**(1): p. 7-15.

286. Galán, A., et al., *ATP hydrolysis induces an intermediate conformational state in GroEL.* European Journal of Biochemistry, 1999. **259**(1-2): p. 347-355.

287. Hansen, J.E. and A. Gafni, *Fluorescence detection of conformational changes in GroEL induced by thermal switching and nucleotide binding.* J Biol Chem, 1994. **269**(9): p. 6286-9.

288. Terada, T.P. and K. Kuwajima, *Thermodynamics of nucleotide binding to the chaperonin GroEL studied by isothermal titration calorimetry: evidence for noncooperative nucleotide binding.* Biochim Biophys Acta, 1999. **1431**(2): p. 269-81.

289. Inobe, T., et al., *Nucleotide binding to the chaperonin GroEL: non-cooperative binding of ATP analogs and ADP, and cooperative effect of ATP.* Biochim Biophys Acta, 2001. **1545**(1-2): p. 160-73.

290. Chapman, E., et al., *Requirement for binding multiple ATPs to convert a GroEL ring to the folding-active state.* Proceedings of the National Academy of Sciences, 2008. **105**(49): p. 19205.

291. Schmidt, M., et al., *Symmetric complexes of GroE chaperonins as part of the functional cycle.* Science, 1994. **265**(5172): p. 656.

292. Koike-Takeshita, A., et al., *Crystal Structure of a Symmetric Football-Shaped GroEL:GroES2-ATP14 Complex Determined at 3.8Å Reveals Rearrangement between Two GroEL Rings.* Journal of Molecular Biology, 2014. **426**(21): p. 3634-3641.

293. Ye, X. and G.H. Lorimer, *Substrate protein switches GroE chaperonins from asymmetric to symmetric cycling by catalyzing nucleotide exchange.* Proceedings of the National Academy of Sciences, 2013. **110**(46): p. E4289.

294. Wilson, J.E. and A. Chin, *Chelation of divalent cations by ATP, studied by titration calorimetry.* Anal Biochem, 1991. **193**(1): p. 16-9.

295. Sakane, I., et al., *Structural stability of covalently linked GroES heptamer: advantages in the formation of oligomeric structure.* J Mol Biol, 2007. **367**(4): p. 1171-85.

296. Owen, B.B., et al., *The Dielectric Constant of Water as a Function of Temperature and Pressure.* The Journal of Physical Chemistry, 1961. **65**(11): p. 2065-2070.

297. Matysiak, S., P.G. Debenedetti, and P.J. Rossky, *Role of Hydrophobic Hydration in Protein Stability: A 3D Water-Explicit Protein Model Exhibiting Cold and Heat Denaturation.* The Journal of Physical Chemistry B, 2012. **116**(28): p. 8095-8104.

298. Hunt, J.F., et al., *The crystal structure of the GroES co-chaperonin at 2.8 Å resolution.* Nature, 1996. **379**(6560): p. 37-45.

299. Zondlo, J., et al., *Monomer-heptamer equilibrium of the Escherichia coli chaperonin GroES.* Biochemistry, 1995. **34**(33): p. 10334-9.

300. Bartolucci, C., et al., *Crystal Structure of Wild-type Chaperonin GroEL.* Journal of Molecular Biology, 2005. **354**(4): p. 940-951.

301. Fei, X., et al., *Crystal structure of a GroEL-ADP complex in the relaxed allosteric state at 2.7 A resolution.* Proc Natl Acad Sci U S A, 2013. **110**(32): p. E2958-66.

302. Sewell, B.T., et al., *A mutant chaperonin with rearranged inter-ring electrostatic contacts and temperature-sensitive dissociation.* Nat Struct Mol Biol, 2004. **11**(11): p. 1128-33.

303. Azem, A., S. Diamant, and P. Goloubinoff, *Effect of Divalent Cations on the Molecular Structure of the GroEL Oligomer.* Biochemistry, 1994. **33**(21): p. 6671-6675.

304. Chaudhry, C., et al., *Role of the γ-phosphate of ATP in triggering protein folding by GroEL–GroES: function, structure and energetics.* The EMBO Journal, 2003. **22**(19): p. 4877-4887.

305. Clare, Daniel K., et al., *ATP-Triggered Conformational Changes Delineate Substrate-Binding and -Folding Mechanics of the GroEL Chaperonin.* Cell, 2012. **149**(1): p. 113-123.

306. Landry, S.J., et al., *Characterization of a functionally important mobile domain of GroES.* Nature, 1993. **364**(6434): p. 255-258.

307. Llorca, O., et al., *GroEL under heat-shock. Switching from a folding to a storing function.* J Biol Chem, 1998. **273**(49): p. 32587-94.

308. Lin, Z., et al., *Repetitive Protein Unfolding by the trans Ring of the GroEL-GroES Chaperonin Complex Stimulates Folding.* Journal of Biological Chemistry, 2013. **288**(43): p. 30944-30955.

309. Roseman, A.M., et al., *The Chaperonin ATPase Cycle: Mechanism of Allosteric Switching and Movements of Substrate-Binding Domains in GroEL.* Cell, 1996. **87**(2): p. 241-251.

310. Rye, H.S., et al., *GroEL-GroES Cycling: ATP and Nonnative Polypeptide Direct Alternation of Folding-Active Rings.* Cell, 1999. **97**(3): p. 325-338.

311. Sakikawa, C., et al., *On the Maximum Size of Proteins to Stay and Fold in the Cavity of GroEL underneath GroES *.* Journal of Biological Chemistry, 1999. **274**(30): p. 21251-21256.

312. Motojima, F. and M. Yoshida, *Polypeptide in the chaperonin cage partly protrudes out and then folds inside or escapes outside.* The EMBO Journal, 2010. **29**(23): p. 4008-4019.

313. Weaver, J., et al., *GroEL actively stimulates folding of the endogenous substrate protein PepQ.* Nature Communications, 2017. **8**(1): p. 15934.

314. Marty, M.T., et al., *Bayesian Deconvolution of Mass and Ion Mobility Spectra: From Binary Interactions to Polydisperse Ensembles.* Analytical Chemistry, 2015. **87**(8): p. 4370-4376.

315. Garces, J.L., et al., *Model-Independent Link between the Macroscopic and Microscopic Descriptions of Multidentate Macromolecular Binding: Relationship*

between Stepwise, Intrinsic, and Microscopic Equilibrium Constants. Journal of Physical Chemistry B, 2009. **113**(46): p. 15145-15155.

316. Garces, J.L., et al., *A hierarchical approach to cooperativity in macromolecular and self-assembling binding systems.* J Biol Phys, 2008. **34**(1-2): p. 213-35.

317. Bui, D.T., et al., *Quantifying Biomolecular Interactions Using Slow Mixing Mode (SLOMO) Nanoflow ESI-MS.* ACS Central Science, 2022.

318. Macro, N., et al., *Slowdown of Water Dynamics from the Top to the Bottom of the GroEL Cavity.* J Phys Chem Lett, 2021. **12**(24): p. 5723-5730.

319. Gruber, R., T. Mondal, and A. Horovitz, *GroEL Allostery Illuminated by a Relationship between the Hill Coefficient and the MWC Model.* Biophys J, 2019. **117**(10): p. 1915-1921.

320. Clare, D.K., et al., *ATP-triggered conformational changes delineate substrate-binding and -folding mechanics of the GroEL chaperonin.* Cell, 2012. **149**(1): p. 113-23.

321. Shi, L., et al., *Characterizing intermediates along the transition from polyproline I to polyproline II using ion mobility spectrometry-mass spectrometry.* J Am Chem Soc, 2014. **136**(36): p. 12702-11.

322. Zhang, J., C.P. Jones, and A.R. Ferre-D'Amare, *Global analysis of riboswitches by small-angle X-ray scattering and calorimetry.* Biochim Biophys Acta, 2014. **1839**(10): p. 1020-1029.

323. Wallerstein, J., et al., *Entropy-Entropy Compensation between the Protein, Ligand, and Solvent Degrees of Freedom Fine-Tunes Affinity in Ligand Binding to Galectin-3C.* JACS Au, 2021. **1**(4): p. 484-500.

324. Wand, A.J. and K.A. Sharp, *Measuring Entropy in Molecular Recognition by Proteins.* Annu Rev Biophys, 2018. **47**: p. 41-61.

325. Lin, C.W., et al., *Mechanistic Insights into IscU Conformation Regulation for Fe-S Cluster Biogenesis Revealed by Variable Temperature Electrospray Ionization Native Ion Mobility Mass Spectrometry.* Biochemistry, 2022.

326. Saibil, H.R., et al., *Structure and allostery of the chaperonin GroEL.* J Mol Biol, 2013. **425**(9): p. 1476-87.

327. Sigler, P.B., et al., *Structure and function in GroEL-mediated protein folding.* Annu Rev Biochem, 1998. **67**: p. 581-608.

328. Horovitz, A., et al., *Chaperonin Mechanisms: Multiple and (Mis)Understood?* Annu Rev Biophys, 2022. **51**: p. 115-133.

329. Ranson, N.A., et al., *Allosteric signaling of ATP hydrolysis in GroEL-GroES complexes.* Nat Struct Mol Biol, 2006. **13**(2): p. 147-52.

330. Chapman, E., et al., *Requirement for binding multiple ATPs to convert a GroEL ring to the folding-active state.* Proc Natl Acad Sci U S A, 2008. **105**(49): p. 19205-10.

331. Ranson, N.A., et al., *ATP-bound states of GroEL captured by cryo-electron microscopy.* Cell, 2001. **107**(7): p. 869-79.

332. Motojima, F. and M. Yoshida, *Discrimination of ATP, ADP, and AMPPNP by chaperonin GroEL: hexokinase treatment revealed the exclusive role of ATP.* J Biol Chem, 2003. **278**(29): p. 26648-54.

333. Taniguchi, M., et al., *Stopped-flow fluorescence analysis of the conformational changes in the GroEL apical domain: relationships between movements in the apical domain and the quaternary structure of GroEL.* J Biol Chem, 2004. **279**(16): p. 16368-76.

334. Chaudhry, C., et al., *Role of the gamma-phosphate of ATP in triggering protein folding by GroEL-GroES: function, structure and energetics.* Embo Journal, 2003. **22**(19): p. 4877-4887.

335. Viitanen, P.V., et al., *Chaperonin-facilitated refolding of ribulosebisphosphate carboxylase and ATP hydrolysis by chaperonin 60 (groEL) are K+ dependent.* Biochemistry, 1990. **29**(24): p. 5665-71.

336. Kiser, P.D., G.H. Lorimer, and K. Palczewski, *Use of thallium to identify monovalent cation binding sites in GroEL.* Acta Crystallogr Sect F Struct Biol Cryst Commun, 2009. **65**(Pt 10): p. 967-71.

337. Horst, R., et al., *Direct NMR observation of a substrate protein bound to the chaperonin GroEL.* Proc Natl Acad Sci U S A, 2005. **102**(36): p. 12748-53.

338. Werbeck, N.D., et al., *Using (1)(5)N-ammonium to characterise and map potassium binding sites in proteins by NMR spectroscopy.* Chembiochem, 2014. **15**(4): p. 543-8.

339. Perozzo, R., G. Folkers, and L. Scapozza, *Thermodynamics of protein-ligand interactions: history, presence, and future aspects.* J Recept Signal Transduct Res, 2004. **24**(1-2): p. 1-52.

340. Olsson, T.S., et al., *The thermodynamics of protein-ligand interaction and solvation: insights for ligand design.* J Mol Biol, 2008. **384**(4): p. 1002-17.

341. Roseman, A.M., et al., *The chaperonin ATPase cycle: mechanism of allosteric switching and movements of substrate-binding domains in GroEL.* Cell, 1996. **87**(2): p. 241-51.

342. Waksman, G., et al., *Binding of a high affinity phosphotyrosyl peptide to the Src SH2 domain: crystal structures of the complexed and peptide-free forms.* Cell, 1993. **72**(5): p. 779-90.

343. Kad, N.M., et al., *Asymmetry, commitment and inhibition in the GroE ATPase cycle impose alternating functions on the two GroEL rings.* J Mol Biol, 1998. **278**(1): p. 267-78.

344. Gorovits, B.M. and P.M. Horowitz, *The chaperonin GroEL is destabilized by binding of ADP.* J Biol Chem, 1995. **270**(48): p. 28551-6.

345. Kudryavtseva, S.S., et al., *Novel cryo-EM structure of an ADP-bound GroEL-GroES complex.* Sci Rep, 2021. **11**(1): p. 18241.

346. Cliff, M.J., et al., *A kinetic analysis of the nucleotide-induced allosteric transitions of GroEL.* Journal of Molecular Biology, 1999. **293**(3): p. 667-684.

347. Grason, J.P., et al., *Setting the chaperonin timer: the effects of K+ and substrate protein on ATP hydrolysis.* Proc Natl Acad Sci U S A, 2008. **105**(45): p. 17334-8.

348. Clark, A.C., B.S. Karon, and C. Frieden, *Cooperative effects of potassium, magnesium, and magnesium-ADP on the release of Escherichia coli dihydrofolate reductase from the chaperonin GroEL.* Protein Sci, 1999. **8**(10): p. 2166-76.

349. Madan, D., Z. Lin, and H.S. Rye, *Triggering protein folding within the GroEL-GroES complex.* J Biol Chem, 2008. **283**(46): p. 32003-13.

350. Stengel, F., et al., *Dissecting heterogeneous molecular chaperone complexes using a mass spectrum deconvolution approach.* Chem Biol, 2012. **19**(5): p. 599-607.

351. Hansen, J.E. and A. Gafni, *Fluorescence detection of conformational changes in GroEL induced by thermal switching and nucleotide binding.* Journal of Biological Chemistry, 1994. **269**(9): p. 6286-6289.

352. Wang, J. and D.C. Boisvert, *Structural Basis for GroEL-assisted Protein Folding from the Crystal Structure of (GroEL-KMgATP)14 at 2.0Å Resolution.* Journal of Molecular Biology, 2003. **327**(4): p. 843-855.

353. Poso, D., A.R. Clarke, and S.G. Burston, *Identification of a major inter-ring coupling step in the GroEL reaction cycle.* J Biol Chem, 2004. **279**(37): p. 38111-7.

354. Saibil, H.R., et al., *ATP induces large quaternary rearrangements in a cage-like chaperonin structure.* Curr Biol, 1993. **3**(5): p. 265-73.

355. Chen, J., et al., *Dissecting a bimolecular process of MgATP(2)- binding to the chaperonin GroEL.* J Mol Biol, 2011. **410**(2): p. 343-56.

356. Buckle, A.M., R. Zahn, and A.R. Fersht, *A structural model for GroEL-polypeptide recognition.* Proc Natl Acad Sci U S A, 1997. **94**(8): p. 3571-5.

357. Fenton, W.A., et al., *Residues in chaperonin GroEL required for polypeptide binding and release.* Nature, 1994. **371**(6498): p. 614-9.

358. Farr, G.W., et al., *Multivalent binding of nonnative substrate proteins by the chaperonin GroEL.* Cell, 2000. **100**(5): p. 561-73.

359. Gorovits, B.M., J. Ybarra, and P.M. Horowitz, *ATP hydrolysis is critical for induction of conformational changes in GroEL that expose hydrophobic surfaces.* J Biol Chem, 1997. **272**(11): p. 6842-5.

360. Pereira, J.H., et al., *Crystal structures of a group II chaperonin reveal the open and closed states associated with the protein folding cycle.* J Biol Chem, 2010. **285**(36): p. 27958-66.